Transferable reduced TB models for elemental Si and N and binary Si-N systems

Jan Gehrmann
St Anne's College
University of Oxford

Supervisors: Ralf Drautz, Aleksey Kolmogorov, David Pettifor

A thesis submitted for the degree of
Doctor of Philosophy
Trinity Term 2013

Acknowledgements

I owe my deepest gratitude to my supervisors Prof Ralf Drautz, Dr Aleksey Kolmogorov, and Prof David Pettifor for their fantastic assistance and guidance throughout the course of this project. The work presented in this thesis would not have been possible without their continuous support.

Further, I am grateful to Martin Reese, Dr Matous Mrovec, and Prof Christian Elsässer at Fraunhofer-Institut für Werkstoffmechanik Freiburg for providing the projected bond integral data which are the basis of the models developed in this work. I am also grateful for their hospitality and many fruitful discussions during project meetings and my four-week stay in Freiburg in late 2011 when the foundation for the bond-order potential for silicon was laid.

I would like to thank Alexander Urban, Dr Pawel Rodziewicz, and Prof Bernd Meyer at Interdisciplinary Center for Molecular Materials and Computer-Chemistry-Center Friedrich-Alexander-Universität Erlangen-Nürnberg for the many discussions during the project meetings and their hospitality in Erlangen. Moreover, I would like to thank Dominik Jäger and Dr Jörg Patscheider at EMPA Dübendorf for their hospitality and insight into experimental work during project meetings in Dübendorf. In addition, I am grateful to the members of ICAMS Ruhr-Universität Bochum, especially to Dr Arthur Bialon and Dr Thomas Hammerschmidt, for their assistance with code development during my visits.

I am very grateful to the members of the Materials Modelling Laboratory (MML), University of Oxford, especially to John Drain, Dr Michael Ford, Dr Benoit Mangili, Dr Elena Roxana Margine, and Dr Bernhard Seiser. In particular, I would like to thank Paul Kamenski for his work on the reduced TB model for silicon, which was a good starting point for the development of the silicon model presented in this work.

Further, my thanks go to the Engineering and Physical Sciences Research Council (EPSRC) and the Department of Materials, University of Oxford for supporting me through a project grant and a Departmental award.

Finally, I would like to thank The Worshipful Company of Founders, St Anne's College, the Department of Materials, and the Multiscale Materials Modeling (MMM) 2012 conference committee for providing funds for me to present my results at MMM 2012 in Singapore.

Abstract

Silicon nitride is a bulk and a coating material exhibiting excellent mechanical properties. The understanding of the complex processes at the nanometre scale gained through experimental research will be enhanced by the existence of a computationally efficient and accurate model that is able to describe the mechanical properties of silicon nitride. Such a model has yet to be proposed.

In this thesis we present a transferable reduced tight-binding (TB) model for the silicon nitride system. More precisely, this model consists of a reduced TB model for elemental silicon, a reduced TB model for elemental nitrogen, and a reduced TB model for silicon nitride. These models are developed within the framework of coarse-graining the electronic structure from density functional theory (DFT) to tight binding (TB) to bond-order potentials (BOPs), and can therefore be used in the future as the stepping stone to develop BOPs for the application in large scale simulations.

The bond integrals employed in the reduced TB models are obtained directly from mixed-basis DFT projections of wave functions onto a minimal basis of atom-centred orbitals. This approach reduces the number of overall parameters to be fitted and provides models which are transferable through the different coarse-graining levels. We provide an example by using the same bond integrals in the reduced TB model for silicon and the preliminary bond-based BOP for silicon. DFT binding energies of ground state and metastable crystal structures are used as the benchmark to which the TB and BOP repulsive parameters are fitted.

In addition to model development, we present an improved methodology when going from TB to reduced TB. By weighting all four σ TB bond integrals equally, we provide a new parameterisation (Eqs. (2.73) and (2.74)) and show that the quality of the silicon reduced TB model can be increased by choosing one of the reduced TB parameters to be distance invariant.

The ingredients, the development methodology, and the quality of each of the four models are discussed in a separate chapter. The quality of the reduced TB models and BOP is demonstrated by comparing their predictions for the binding energies, heats of formation, elastic constants, and defect energies with DFT and experimental values.

Contents

1 Introduction **1**

2 Background **5**

2.1 Silicon Nitride (Si-N) 6

2.1.1 Applications of Si-N 6

2.1.2 Structure of Si-N 6

2.1.3 Synthesis and processing of Si-N 11

2.1.4 Microstructure and mechanical properties of Si-N 17

2.2 Interatomic Potentials for Si-N 22

2.2.1 Abell-Tersoff-Brenner interatomic potentials 22

2.2.2 Vashishta potential 27

2.2.3 Reactive force fields 31

2.2.4 Bond-based bond-order potentials 32

2.2.5 A note on growth simulations 37

2.3 Systematic Derivation of Interatomic Potentials 38

2.3.1 Density functional theory (DFT) 38

2.3.2 Tight binding (TB) approximation 41

2.3.3 Bond-order potentials (BOPs) 43

2.4 Methodology 48
2.4.1 From DFT to TB 48
2.4.2 From TB to reduced TB 57
2.4.3 From reduced TB to BOP 64
2.4.4 Computational details 65
2.5 Summary 67

3 Reduced TB Model for Silicon 69
3.1 Bond Integrals 69
3.2 Binding Energy Curves 80
3.2.1 DFT binding energy curves 82
3.2.2 Reduced TB binding energy curves 82
3.2.3 Equilibrium properties of diamond ground state 87
3.3 Summary 91

4 Reduced TB Model for Nitrogen 92
4.1 Bond Integrals 92
4.2 Binding Energy Curves 99
4.2.1 DFT binding energy curves 100
4.2.2 Reduced TB binding energy curves 101
4.2.3 Equilibrium properties of dimer ground state 101
4.3 Summary 104

5 Reduced TB Model for Silicon Nitride 105
5.1 Bond Integrals 106
5.2 Heat of Formation Curves 113
5.2.1 DFT heat of formation curves 115

5.2.2 Reduced TB heat of formation curves 116

5.2.3 Equilibrium properties of β phase ground state 124

5.3 Summary 128

6 Bond-order Potential for Silicon 130

6.1 Bond Integrals 130

6.2 Binding Energy Curves 132

6.2.1 DFT binding energy curves 132

6.2.2 BOP binding energy curves 134

6.2.3 Equilibrium properties of diamond ground state 135

6.3 Summary 141

7 Conclusions and Future Work 142

References 148

1 Introduction

Silicon nitride is one of the most widely used non-oxide ceramics and is employed in the bulk and as coatings in many applications, ranging from automotive to microelectronic industries [1–3]. Due to their high strength, hardness, and wear resistance, low density and friction coefficient, and excellent chemical and thermal stability, silicon nitride ceramics are applied in many areas at both low and high temperatures [4]. Examples include gas turbines, heat exchangers, car engine parts, fans, unlubricated roller and ball bearings, valves, seals, and crucibles for molten metal [5, 6].

In addition to the application of silicon nitride in the bulk, silicon nitride films play an important role in microelectronic technology [7] and microsystems technology [8]. Due to the material's chemical resistance, ease of deposition with various processes, and etching properties (especially the etching rate compared to silicon), silicon nitride is employed in a variety of semiconductor manufacturing processes [9]. Applications include sacrificial layers, masks, and passivation layers [10, 11]. In microelectronic technology for instance, mainly amorphous silicon nitride is applied due to its low electrical conductivity, high dielectric constant, high resistance against radiation, high temperature stability, and its high barrier against alkali-ion migration and impurity diffusion. Further, silicon nitride is applied in integrated circuits as dielectrics in capacitors and transistors. Silicon nitride coatings are also widely

employed for their mechanical properties and are used against wear and corrosion both by itself and in composite coatings in combination with other materials like silicon carbide, titanium carbide, titanium nitride, and aluminium oxide [12–14]. In order to investigate deposition processes of silicon nitride on the atomistic level and understand the complex interatomic and interface processes, the availability of accurate and yet computationally efficient models is crucial.

The electronic structure of silicon nitride has been intensively studied with the tight-binding (TB) method by Robertson *et al.* in order to help elucidate the nature of the defects in amorphous silicon nitride [15–19]. Interatomic potentials have been developed for the atomistic simulation of crystalline and amorphous silicon nitride using either the covalent bond-order-type Tersoff potential [20] or the two- and three-body Vashishta [21] potential that describes both ionic pairwise and covalent bond-bending interactions. However, no reduced TB model that would close the gap between the work by Robertson *et al.* and the interatomic potentials developed so far by describing the binding energy for silicon nitride has been developed until now. Such a high quality and transferable reduced TB model for silicon nitride is also crucial for the development of an accurate bond-based bond-order potential (BOP) for silicon nitride, since it provides the necessary input parameters.

Ideally, one would like to represent the atomic interactions of the silicon nitride system with a quantum mechanical approach, treating the electronic degrees of freedom explicitly. This has been done with *ab initio* methods to investigate the structural stability of silicon nitride crystal phases [22–26]. However, due to the restriction of computing power, only simulations using empirical interatomic potentials, which often lack transferability and accuracy, can reach the length and time scales necessary to study phenomena such as film growth, nanoindentation, radiation

damage, and dislocation dynamics. Nevertheless, in contrast to empirical potentials, bond-based bond-order potentials (BOPs) could provide an accurate description of a wide array of local atomic environments in covalent systems [27]. Generally, analytic BOPs can be derived either for metals [28] or semiconductors [29, 30] by coarse-graining the electronic structure from density functional theory (DFT) to TB to BOPs. Within this approach, the TB parameters can be extracted directly from DFT by projecting the wave functions onto a minimal basis of atom-centred orbitals [31, 32]. In the particular case of bond-based BOPs, reduced TB links the quantum mechanical with the atomistic level. We show that reduced TB is not just a theoretical coarse-graining step in the development of bond-based BOPs, but, in addition, provides a transferable model when applied to the silicon nitride system. This reduced TB model for the silicon nitride system can be used in the future to develop a transferable bond-based BOP. Furthermore, it is known that interatomic electronic charge redistribution is present in heterovalent compounds such as silicon nitride due to the large Pauling electronegativity difference between the atomic species [33]. This results in a hybrid of covalent and ionic bonding. We have included charge transfer within a self consistent density-functional tight-binding scheme [34].

In this thesis, we present a reduced TB model for silicon, a reduced TB model for nitrogen, a reduced TB model for silicon nitride, and a bond-based BOP for silicon. The bond integrals employed in the reduced TB and BOP models are obtained directly from DFT and the elemental silicon and nitrogen bond integrals and repulsive potentials are fully transferable from elemental to binary situations. In addition, the same bond integrals are used in the reduced TB model and BOP for silicon. This BOP for silicon demonstrates the transferability of the bond integrals

between the reduced TB and BOP levels, however, this BOP for silicon is only a preliminary model and needs further testing and refinement in the future. The quality of any bond-based BOP is defined by the accuracy of the underlying reduced TB model. Therefore, we focused on fine tuning the reduced TB models with respect to the ordering of the lowest energy structures.

This thesis is structured as follows. In Chapter 2 we begin with an interpretation of the background information. We begin with an introduction to the silicon nitride system in Section 2.1 and continue with a discussion of existing interatomic potentials for silicon nitride in Section 2.2. The theory and techniques employed in the derivation of interatomic potentials are described in Sections 2.3 and 2.4. Chapter 3 summarises the reduced TB model for silicon, Chapter 4 the reduced TB model for nitrogen, and Chapter 5 the reduced TB model for silicon nitride. Further, Chapter 6 gives details of the bond-based BOP for silicon. The quality of the reduced TB models and the BOP is demonstrated by comparing their predictions for the electronic structure, binding energies, heats of formation, elastic constants, and defect energies with DFT and experimental values. Finally, in Chapter 7, we conclude and suggest directions for possible further work.

2 Background

This Chapter is on silicon nitride and the relevant background information for the development of interatomic potentials. We start with an introduction to silicon nitride in Section 2.1 by focusing on the material's industrial applications in Subsection 2.1.1, the crystal structures in Subsection 2.1.2, the synthesis in Subsection 2.1.3, and the mechanical properties in Subsection 2.1.4. In Section 2.2 we discuss different interatomic potentials which have been used in both molecular dynamics (MD) and Monte Carlo (MC) simulations to investigate the silicon nitride system. Atomistic simulations of growth which have been done with these potentials are considered at the end of each Subsection. The theory and techniques necessary to develop a reduced tight-binding (TB) model and a bond-based bond-order potential (BOP) are described in Sections 2.3 and 2.4. In particular, the coarse-graining steps from density functional theory (DFT) to TB, from TB to reduced TB, and from reduced TB to BOP are described in Subsections 2.4.1, 2.4.2, and 2.4.3, respectively. Section 2.5 presents a summary of the background chapter's conclusions.

2.1 Silicon Nitride (Si-N)

2.1.1 Applications of Si-N

Silicon nitride can be applied in many areas and is therefore of particular interest to industry. Due to its excellent properties, silicon nitride is applied at both low and high temperatures, in the bulk and as films, and in different industries ranging from the automotive to the microelectronic industry [1–14]. The properties of silicon nitride and application examples were given in the introductory passages of Chapter 1.

2.1.2 Structure of Si-N

Silicon (Si) is in group IV and nitrogen (N) in group V of the periodic table. Silicon and nitrogen have four and five valence electrons, respectively, which in the atomic ground state have an s^2p^2 and s^2p^3 occupation. Due to hybridisation, both elements form a number of different bonding states. Examples of sp^3 hybridisation include silicon in the diamond structure (all four sp^3 orbitals with one unpaired electron per atom) and nitrogen in ammonia (NH_3) (one sp^3 orbital with a non-bonding pair of electrons and three with one unpaired electron per atom).

Figure 2.1 shows a calculated phase diagram for the Si-N binary system [35]. The phase diagram includes the gas phase (G), the silicon liquid solution phase (L), the stoichiometric compound Si_3N_4 phase (Si_3N_4), and the diamond silicon phase (Si).

Silicon forms the diamond structure at ambient conditions, where each silicon atom is tetrahedrally bonded to its four neighbours. Nitrogen forms diatomic molecules in the gas state at ambient conditions. It is assumed that all solid phases of nitrogen are also built from these diatomic units [36]. In both, gaseous and solid

phases, the nitrogen pairs are strongly triple bonded with weak van der Waals forces acting between the different molecules. Theoretical studies have suggested other forms of nitrogen in the solid phase, for instance twofold and threefold coordinated polymeric forms [37].

Even though different polytypes of silicon nitride have been proposed, Si_3N_4 is the only well-established stoichiometric compound in the Si–N binary system [35]. The 3:4 composition is anticipated, since this composition can basically be explained by the fact that silicon wants to bind to four neighbours due to having four unpaired valence electrons and nitrogen wants to form bonds with three neighbours due to its three unpaired valence electrons. As one can see from the phase diagram, at ambient pressure Si_3N_4 has no melting temperature, but dissociates into silicon (L) and nitrogen (G) at 1877 °C. With increasing temperature larger fractions of the liquid silicon transform into gaseous silicon.

There are two main polytypes of the Si_3N_4 phase, the β- and α-Si_3N_4 structures, which are both hexagonal and differ only by their stacking sequence [39]. The β structure is experimentally known to be thermodynamically more stable than the α structure at ambient conditions [40], yet the difference in their heat of formation is marginal being only 2 meV/atom [41]. Even though it was supposed that the α and β structures are low and high temperature forms respectively, only the transformation from the α to the β structure has been observed experimentally but never a conversion in the opposite direction [5, 40, 42, 43]. For instance, in sintering studies of a mixture of α/β starting powders it was observed that the β content increased with sintering time [44].

For both the α and β structure the basic building block is a Si-N tetrahedron with a silicon atom at its centre and four nitrogen atoms at each vertex (see Figure 2.2).

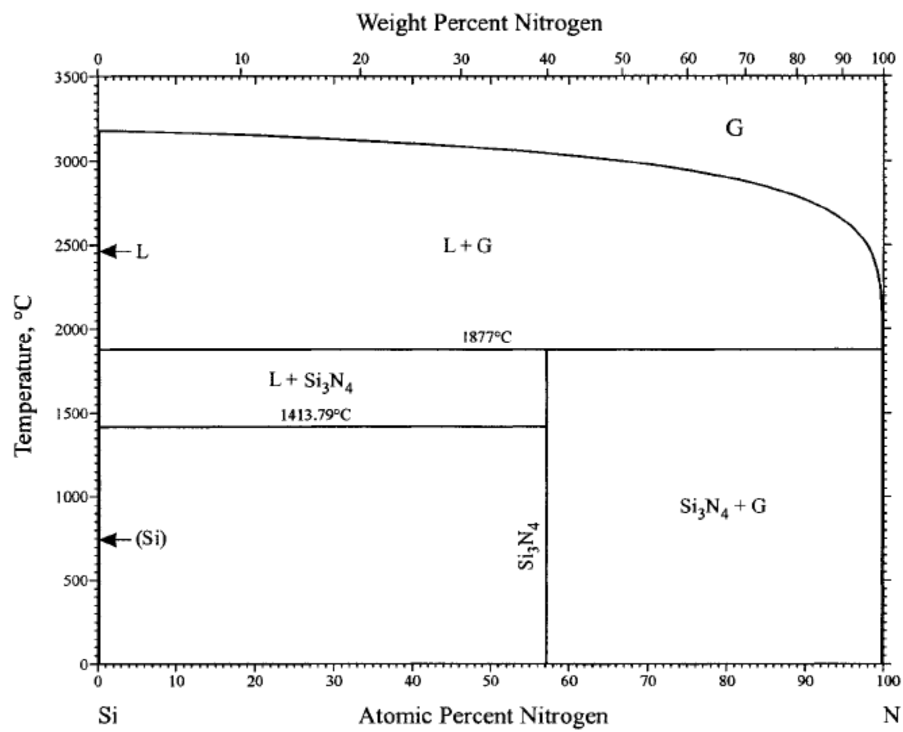

Figure 2.1: Calculated Si–N phase diagram at 1 atm from Ref. [35]. (Figure modified from Ref. [38].)

All these SiN_4 tetrahedra are linked by nitrogen atoms which are each common to three tetrahedra. As a result each silicon atom has four nitrogen atoms as nearest neighbours and each nitrogen atom has three silicon atoms as nearest neighbours.

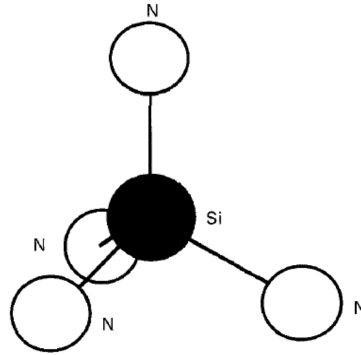

Figure 2.2: The tetrahedral unit in Si_3N_4 (modified from Ref. [45]).

The distinction between both polytypes is that they can be described as Si-N layers in an ... ABCDABCD ... order for the α structure and an ... ABAB ... order for the β structure (see Figure 2.3). The AB layers are the same for the α and β structure and the CD layers in the α structure are shifted along a c-glide plane compared to the AB layer. Due to this, the c-axis dimension of the unit cell of the α structure, consisting of $Si_{12}N_{16}$, is approximately twice that of the β structure, consisting of Si_6N_8. Furthermore, the α structure contains considerable lattice strain energy due to distorted bonds and bond angles compared to idealised Si-N layers, expressed by lattice distortion and the displacement of atoms from the idealised positions, whereas the β structure is almost strain free [46]. Moreover, the larger voids in each basal sheet created by the linking of six eight-membered Si-N rings do not align and therefore no continuous c-axis channels occur in the α structure, whereas they align in the β structure and hence provide continuous c-axis channels of diameters around 3 Å [39].

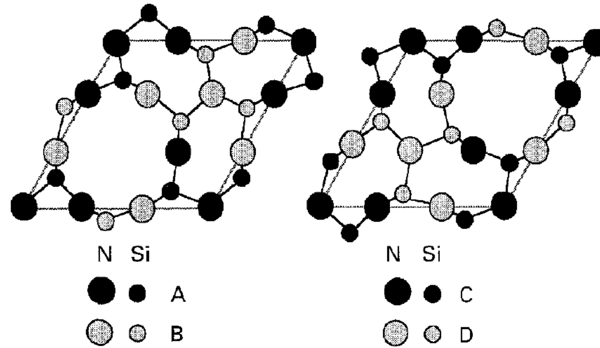

Figure 2.3: The idealised Si-N layers in the α and β crystal structures: ...ABAB... for the β structure and ...ABCDABCD... for the α structure [46]. The small and large circles represent silicon and nitrogen atoms respectively. The black circles represent atoms from the A and C layers and the grey circles represent atoms from the B and D layers.

In addition to the two polymorphs mentioned above, a spinel structure, called γ, has been discovered which can form at pressures above 15 GPa and temperatures exceeding 2000 K [47]. Further, a diffusionless transformation from the spinel to a metastable willemite-II (wII) structure has been suggested, which appears to be energetically more favourable than the spinel structure at zero pressure [48].

Silicon nitride amorphous films mostly have the fundamental SiN_4 and NSi_3 structural units of the crystalline phase but lack long-range ordering and have a tendency of their stoichiometry to differ from the 3:4 ratio (x = 1.33 in SiN_X). For instance, stoichiometries of x = 0 to 1.83 have been reported using reactive magnetron sputtering [49].

2.1.3 Synthesis and processing of Si-N

Bulk Si-N

The vast majority of non-oxide bulk ceramics are produced from high quality powder. The quality of the powder is directly related to the achievable densification of the manufactured parts with desirable properties approaching the theoretical limit of the material. Having a good grasp of the silicon nitride phase chemistry and processing parameters is crucial for achieving the necessary microstructures for the desired properties of the finished part.

Two purity grades of silicon powder are used at the start of most of the silicon nitride processing routes: metallurgical-grade and semiconductor-grade silicon powder. The metallurgical-grade silicon powder (> 98 % Si) is usually prepared through a carbothermal reduction of silicon dioxide (SiO_2) with a carbon electrode. This product still includes 2% contamination of carbon (C), boron (B), and phosphorus (P), which is unsuitable for electronic devices. Polycrystalline semiconductor-grade powder can then be produced in two further steps. First, gaseous hydrochloric acid (HCl) is added to fine ground metallurgical-grade silicon in a fractional distillation process to produce hydrogen (H_2) and liquid trichlorsilane ($SiHCl_3$). Second, with the addition of hydrogen, the trichlorsilane is decomposed into polycrystalline pure silicon (< 1 ppb contamination), silicon tetrachloride ($SiCl_4$), and hydrochloridic acid. The polycrystalline pure silicon is not only used in the silicon nitride production but also single crystalline silicon can be produced from it in the Czochralski process [50].

High-purity silicon nitride powder is needed for the production of silicon nitride components via hot-pressing and sintering processes. Measures for the quality of the silicon nitride powder are a small mean particle size (< 200 nm), a narrow

particle-size distribution, an equiaxed morphology, and the absence of agglomerates [5]. All these have a significant impact on the densification process [5]. The silicon nitride powder is usually produced using either direct nitridation of metallurgical-grade or semiconductor-grade silicon powder [51], carbothermal reduction of silicon dioxide with simultaneous nitridation [52], or high-temperature decomposition of silicon diimide [53].

Due to its relatively low self diffusion coefficients, sintering of silicon nitride is extremely difficult. Several processes have been developed leading to different properties of the finished silicon nitride parts. One process is the reaction-bonding of silicon nitride (reaction-bonded Si-N (RBSN)) [54] in which metallurgical-grade silicon powder together with binders and additives is first formed into a green body and then nitrided in an exothermic reaction between 1000 and 1300 °C. This process makes complex shapes possible but also leads to porous end products (25%–35% porosity) [5]. Two further processes lead to denser finished parts, namely to hot-pressed silicon nitride (HPSN) and to sintered silicon nitride (SSN). HPSN is the most common silicon nitride form, which is made by compressing Si_3N_4 powders (usually α-Si_3N_4) with MgO additives (and others like BeO, Mg_3N_2, and Al_2O_3) to promote densification at 20-30 MPa at 1850 °C for up to 2 hours. In this process mixtures of α- and β-Si_3N_4 are produced, where the α:β ratio depends on the processing parameters. The strength of HPSN depends considerably on the purity of the Si_3N_4 powder. The class of SSN became of interest when it was discovered that no applied mechanical pressure was needed to produce high-density silicon nitride ceramics when the loss of Si_3N_4 by evaporation can be restrained [55, 56]. Since the additives (e.g. MgO) form liquid phases, pressureless sintering of Si_3N_4 (SSN) is possible, even though an overpressure of N gas is usually used to prevent

the decomposition of Si_3N_4 during the sintering process. As a second step, using the powder bed technique, where the compacted Si_3N_4 powder containing sintering additives (e.g. MgO) is immersed in a bed of loosely packed Si_3N_4 powder (also with MgO additives), a 98% density can be obtained after 5 h at 1650 °C and at 1 bar nitrogen pressure [57].

Generally, α-Si_3N_4 can be synthesised at ambient pressure and temperatures below 1500 to 1550 °C while β-Si_3N_4 requires higher temperatures [42, 47]. As mentioned earlier, only the transformation from α- to β-Si_3N_4 has been observed experimentally, meaning that the α/β ratio can only decrease during sintering processes. After prolonged heating of α-Si_3N_4 at temperatures higher than 1450 °C this transformation starts and a complete conversion from α to β can be reached at temperatures between 1750 to 1900 °C and a pressure of 22.7 MPa with the addition of Mg_3N_2 and MgO [42].

Si-N coatings

Amorphous [58, 59] or polycrystalline [60] silicon nitride films can be deposited via various chemical vapour deposition (CVD) and physical vapour deposition (PVD) techniques [61]. The difference between the two methods is that in the CVD process chemicals in the gas state are fed into and react inside the chamber to form solid and desorbing gaseous products, whereas in the PVD process evaporated gaseous products are fed into or produced inside the chamber and condensate on a "cold" substrate. Due to its high dissociation temperature and to reduce stress levels in the grown films, in all processes, silicon nitride is usually not deposited directly onto the semiconductor surface but onto an approximately 5 to 50 nm thick pyrolytic SiO_2 layer [5]. Even though silicon nitride is usually deposited in a low pressure (10-10^3

Pa) CVD (LPCVD) process in industry, several other processes are widely employed and discussed in the literature. Examples are atmospheric pressure CVD (APCVD) [62] and PVD sputtering with Ar [63].

The most common LPCVD processes are the silane-process, usually carried out in a cold-wall reactor, and the dichlorsilane-process, mainly carried out in a hot-wall reactor, [64]. Several molecular excitation systems can be used in these LPCVD techniques to reduce the deposition temperature and the radiation damage, including plasma enhancement (PECVD), laser enhancement (LECVD), ultraviolet photon enhancement (PHCVD), and microwave and electron cyclotron resonance.

One advantage of CVD grown dense and high-purity amorphous and polycrystalline silicon nitride over the bulk production processes is the complete absence of intergranular glass, which leads to better high-temperature strength and oxidation resistance. Uncracked polycrystalline α-Si_3N_4 films with grain sizes of 0.1-1 μm could be produced at $\geq$ 1200 °C, ambient pressure, and low deposition rates (< 35 nm/h). With the LPCVD process at 10^3 Pa, much thicker (> 4 mm) uncracked deposits of polycrystalline α-Si_3N_4 could be obtained on graphite formers at much higher rates (< 0.4 mm/h). Under similar conditions and with the addition of $TiCl_4$ vapour, up to 1.1 mm thick β-Si_3N_4 plates could be grown which included three to four wt.% Ti-N in the β matrix [65]. Amorphous films can be produced by direct nitridation of silicon with NH_3 at temperatures of up to 950 °C, although due to the low diffusion coefficient of nitrogen in silicon nitride this process is self-limiting to a thickness of about 10 nm [5].

One of the most common PVD processes is reactive sputtering of silicon in Ar-N_2 mixtures [66]. This process allows the deposition of stoichiometric amorphous and polycrystalline Si_3N_4 layers. Similarly to the CVD process, the PVD process

has undergone some modifications over the last decades, one of them being the unbalanced magnetron sputtering (UMS). UMS uses argon and nitrogen gas at pressures of 1 to 5 x 10^{-1} Pa, a heated silicon substrate with temperatures between 500 and 800 °C, and a non-heated chamber which can reach temperatures of about 100 °C. In this process, argon ions sputter silicon atoms out of the silicon target. The N_2 molecules are split up in the vicinity of the substrate due to the heat of the plasma and the silicon and nitrogen atoms then precipitate on the substrate. The unbalanced magnetron is used to increase the plasma density. The UMS technique can also be used to deposit Ti-N layers on silicon or steel by using a titanium instead of a silicon target [67]. One advantage of sputtering over conventional CVD processes is that the increase of the bias voltage and hence the energy of the ions, which bombard the deposited layer during the growth process, results in very smooth surfaces and dense films [68]. Other advantages are low-temperature processing, extremely low hydrogen content, use of non-toxic gas, and a simple processing structure [69].

In both, CVD and PVD, the quality and microstructure of the product is controlled by the surface and volume energies of the substrate and deposited layer, and the substrate temperature and morphology. In addition, the energy and rate of the impacting particles, the interaction between the particles including total and partial pressure, flow rate, and mean free path, have an influence on the quality and microstructure of the deposited layer. Another important impact on the film properties is the reaction at the surface, which is influenced for instance by the purity of the surface and the chemicals in the gas phase, the gas phase and surface diffusion, and the nucleation and adhesion on the surface. The influence of pressure and homologous temperature on the microstructure is shown in Figure 2.4. A

stepwise transition from a porous columnar structure with a rough surface towards a polycrystalline dense structure with more spherical grains and a smooth surface can be seen with increasing temperature and decreasing pressure.

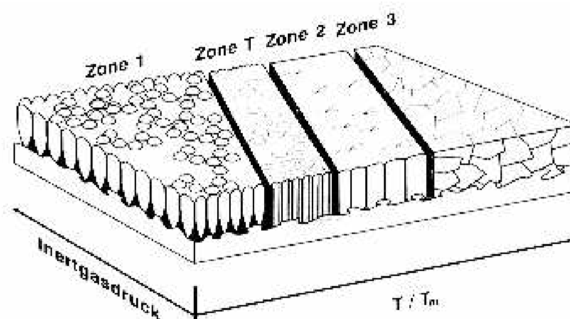

Figure 2.4: Inert gas pressure (Inertgasdruck) and homologous temperature (T/T_m) effects on the microstructure of deposited films [70].

Although the detailed growth mechanisms of silicon nitride do not seem to be sufficiently understood and the influence of different processing parameters on the deposited film is complex, experimental PVD studies of the growth of silicon nitride show certain trends. For instance, an increase in nitrogen partial pressure and a decrease in the target voltage has led to a decrease in the sputtering rate and nitrogen content in the deposited films [66]. At a high nitrogen pressure, target poisoning and a low sputtering rate were observed [68]. In general, the energy of the particles in the gas phase is higher at lower pressure due to fewer collisions and at higher temperature due to higher kinetic energies. An increase of temperature and a decrease of pressure in the processing chamber leads to more uniform and denser deposited films, to an increase in deposition rate, and to a higher surface movement of deposited atoms which leads to a smaller pore density and better conformity. Disadvantages of increasing the temperature in the chamber are a higher substrate strain and an increase in the risk of unwanted gas phase reactions. However, the

latter effect can be reduced by decreasing the chamber pressure. An increase of the bias voltage and hence an increase in the condensation energy of the ions leads to a higher adatom mobility, better adhesion, decrease in voids and porosity, higher density of the deposited film, and smoother surfaces [68, 69]. An increase of the substrate bias also has an influence on the composition. An increase of nitrogen content in the films with increasing bias due to higher reactivity between nitrogen and silicon was reported. Although, due to re-sputtering effects of nitrogen from the deposited film the nitrogen content decreased if the bias was increased further than -75 V [68, 69]. With no applied bias the N/Si ratio was close to the stoichiometric value of 1.33 and reached a value of 1.55 at -200 V [68, 69]. A disadvantage of raising the bias voltage is, however, the increase in strain of the substrate. For improving the layer quality, the substrate can be heated (200 to 500 °C), which leads to a lower deposition rate and a higher mobility of the deposited atoms, and this results in a higher density of the films, smaller pore density, better adhesion, and fewer inclusions of sputtering gas (e.g. argon).

2.1.4 Microstructure and mechanical properties of Si-N

Bulk Si-N

As mentioned in Subsection 2.1.3, the microstructure achieved with the aid of different processing steps has a major influence on the mechanical properties of the finished parts. Whereas the yield and tensile strength of ductile materials like metals can be increased the most through impeding the movement of dislocations by introducing as many obstacles as possible, and hence preventing plastic deformation, the properties of brittle materials like ceramics depend mostly on the materials ability to prevent crack nucleation and propagation. Grain size has a significant

effect on the resistance against crack nucleation and propagation. In general, smaller grains are preferable to increase the resistance against crack nucleation, but larger grains are preferable to increase the resistance against crack propagation (fracture toughness). This is because crack wake mechanisms, such as crack bridging, grain rotation, and grain pullout are less likely to occur with increasing grain sizes, whereas smaller diameter grains are easier to be bypassed and/or cut by the propagating crack [71]. However, the increase of grain size over a critical value can also lead to a reduction in fracture toughness [72].

The main factor in improving silicon nitride's mechanical properties lies in increasing its resistance against crack propagation, i.e. increasing its fracture toughness [72, 73]. Silicon nitride has a fracture toughness (K_{Ic}) of 3 to 10 MPa$\sqrt{m}$, which is quite high for ceramics but low compared to metals. In silicon nitride, the fracture toughness depends on the α content of the starting powder, the processing conditions and annealing treatments. The resulting microstructural features like size, aspect ratio, orientation and volume fraction of the β grains and different reinforcement mechanisms also affect the fracture toughness. Furthermore, the test conditions like test temperature, loading rate, testing atmosphere, and crack length have an influence [71]. A high fracture toughness can be achieved by evenly distributing the crack propagation energy of an advancing crack to either stop or deflect the crack or by channeling the crack direction away from the main crack front (perpendicular to the axis of applied stress) so that brittle fracture is postponed. Mechanisms to increase the fracture toughness relevant to silicon nitride include crack deflection, grain pull out, elastic bridging, and frictional grain bridging [74]. Crack deflection is favoured at larger grains and at temperatures above the glass transition temperature of the intergranular films. Grain pull out is favoured for smaller grains and for higher

test temperatures. Elastic bridging means that an elongated grain sustains some of the load being applied at the crack tip before ultimately being cut and is favoured for larger diameter grains. Frictional bridging means that contact points form between the upper and lower faces of the opened crack. This mechanism is favoured when the faces are roughened due to crack deflection, grain pull out or oxidation processes during the test [74]. Grain pull out, elastic bridging, and frictional grain bridging all shield the crack tip while it propagates through the material.

Depending on the processing method, silicon nitride can achieve strengths between 200 and 1100 MPa at temperatures of up to 1400 °C [5]. RBSN exhibits strengths of 200-300 MPa, the less porous HPSN, with Y_2O_3 additives, can reach strengths of 500–600 MPa, and SSN strengths of up to 1100 MPa. Due to the covalent nature of the bonding in ceramics, their Young's modulus and hardness values are high compared to those of metals. Silicon nitride has Young's modulus values for HPSN and SSN from 191 to 350 MPa [75]. HPSN and SSN exhibit values of Vickers microhardness from 8.6 to 18.9 GPa [75]. The high pressure polycrystalline cubic γ-Si_3N_4 at low oxygen concentration (< 0.5 wt%) showed an remarkable Vickers hardness of 43 GPa [76].

Si-N coatings

In addition to the importance of amorphous silicon nitride films in the semiconductor device field, silicon nitride plays a major role in the development of hard coatings, especially when it is applied in combination with other materials like silicon carbide [13] and titanium nitride [77]. In general, the same microstructural features and mechanical properties play a role in the two-dimensional coatings as in the bulk, although the interface properties between the coating and the substrate are impor-

tant, for instance lattice mismatch and adhesion. While there are well-documented mechanical property data of bulk materials, mechanical testing of coatings is more difficult and only limited data for films with varying thicknesses and process dependent properties can be found in the literature [78].

The Young's modulus of the film, especially compared to the substrate, is significant for the design process. For PECVD silicon nitride, values in the range between 97 and 220 GPa could be achieved on silicon wafers [79] and between 70 and 150 GPa on fused silica and borosilicate glass [80]. For LPCVD silicon nitride on silicon wafers Young's modulus values were measured between 130 and 290 GPa [81].

In the case of coatings, hardness is most commonly measured by nanoindentation [82]. Hardness values for PECVD grown silicon nitride on fused silica and borosilicate glass were reported between 8 and 15 GPa [80] and for magnetron sputtered silicon nitride on silicon and cemented carbide up to 31 GPa.

By depositing a Si_3N_4/SiC multilayer composite on silicon and cemented carbide via magnetron sputtering, Vickers hardness values of 26 GPa were measured [13]. The hardness of the Si_3N_4/SiC multilayers was always found to be higher than the average value of the monolayers. Further, the hardness was found to be subject to competing effects resulting from varying deposition temperatures. Increasing the deposition temperature led to an increase in hardness from structural relaxation, however at higher deposition temperatures the hardness dropped due to a decrease in the film stress. In addition, moderate and low adherence of the films to the metal substrates was observed.

TiN/Si_3N_4 nanocomposite coatings consist of crystalline titanium nitride nanograins embedded in an amorphous silicon nitride matrix [83–87]. The predominant deformation mechanisms are shear sliding at grain boundaries, grain

boundary rotation and collective displacement of non-deformed nanocrystals as well as cracking at the nanocrystalline boundaries under local tension in a quasi-plastic manner [88, 89]. In these nanocomposites the grain size is too small to be deformed by dislocation activity. Young's moduli in excess of 500 GPa and Vickers hardness values of 49 GPa have been measured [83]. Hardness values between 80 and 100 GPa were achieved by increasing the silicon content and hence forming amorphous $TiSi_2$ at the titanium nitride nanocrystal grain boundaries [90]. The same authors reported that the surface of these titanium nitride nanocrystals was covered with approximately one monolayer of stoichiometric Si_3N_4.

In addition to the nanograined TiN/Si_3N_4 nanocomposite coatings, TiN/Si_3N_4 can also be grown as multilayers [91]. Each layer can have a thickness of the order of several nanometres. Their hardness and wear resistance are high and depend critically on the thickness of the individual layers as well as on the nature of the interface [92]. For instance, it was found that oxygen impurities cause a significant reduction of the interface strength [93] and that a monolayer of silicon nitride between titanium nitride slabs leads to very high decohesion and shear strengths [94].

2.2 Interatomic Potentials for Si-N

In general, interatomic potentials should possess the following properties. First, their potential function should be flexible, meaning that the function can be fitted to a wide range of input data, which could include lattice constants, cohesive energies, elastic properties, vacancy formation energies, and surface energies. Second, the potential function should be accurate, meaning that it can reproduce the fitting database accurately. Third, the interatomic potential should be transferable, meaning that the potential can describe quantitatively, or at least qualitatively, structures not included in the fitting database. Fourth, the computation of energies and forces should be efficient.

To investigate the silicon nitride system, different interatomic potentials have been used in both molecular dynamics (MD) and Monte Carlo (MC) simulations over the last few decades. Studies include the investigation of cracks [95], interfaces [96, 97], shearing deformation [98], nanoindentation [99], fracture [100, 101], growth mechanisms [102, 103], and structural properties of amorphous silicon nitride [104]. The most commonly used interatomic potentials for studying silicon nitride are Tersoff- [20] and Vashishta-type [21] potentials. Another less often used potential is the reactive force field (ReaxFF) [105]. These potentials are described in Subsections 2.2.1 to 2.2.3. A short introduction to bond-based bond-order potentials (BOPs) is given in Subsection 2.2.4.

2.2.1 Abell-Tersoff-Brenner interatomic potentials

The common form of the Abell-Tersoff-Brenner many-body potentials includes pairwise repulsive nearest-neighbour interactions and an attractive term in a form which depends on the local environment through an effective bond order. This form was

initially suggested by Abell [106] for s-valent systems, where the bond order depends on the square root of the coordination. Tersoff developed this description further for the sp-valent element silicon (Si) [20, 107, 108] and later extended it to carbon (C) [109] and germanium (Ge) [110] and their alloys Si-C [108, 110] and Si-Ge [110, 111]. The Tersoff model has been used extensively to study a wide range of phenomena and systems [112]. The Tersoff model, which only models σ bonding explicitly, correctly simulates the dynamics of a number of silicon and carbon structures [20, 107, 109]. Nevertheless, the Tersoff model leads to unphysical results for bonding situations in conjugated systems including graphite.

To improve on the form of the Tersoff potential, in 1990 Brenner [113] developed a potential for hydrocarbons, which can model the bonding in a number of hydrocarbon molecules, diamond, and graphite and can describe the deposition of diamond films accurately. This model corrects the Tersoff potential by including effects from π-bonds and radicals. However, no potential that includes π-bonds and radicals properly has been developed for the silicon nitride system so far.

In 1998 de Brito Mota *et al.* [104, 114, 115] published an empirical potential of the Tersoff form for interactions between silicon and nitrogen. They fitted their parameters to a set of *ab initio* and experimental data which included experimental lattice parameters of the crystalline β-Si_3N_4 phase, *ab initio* values for the average binding energy of β-Si_3N_4, experimental equilibrium interatomic distance and binding energy of the N_2 molecule, and the *ab initio* result for the structure of the silicon-nitrogen bonds in the Si_3NH_9 molecule. This potential provides a description of amorphous silicon nitride in a wide range of nitrogen contents, from pure silicon to stoichiometric Si_3N_4, but includes only a repulsive nitrogen-nitrogen interaction and therefore unphysically prevents nitrogen-nitrogen bond formation. Despite the

non-attractive nitrogen-nitrogen interaction, this parameterisation has been applied to simulations of deposition [103, 116] and deposition related [117] processes. Besides the repulsive nitrogen-nitrogen interaction parameterised by de Brito Mota *et al.*, Albe *et al.* [118] parameterised nitrogen-nitrogen interactions in a Tersoff-like form which included nitrogen-nitrogen attraction, although this was for the boron nitride system.

Si-N growth simulation

To our knowledge, the Tersoff functional form has not been considered extensively for modelling the growth of Si-N in the literature. However, in 2009 Gou *et al.* [103] conducted MD simulations using the de Brito Mota interatomic potential [104] on the growth of silicon nitride by bombarding a layer of amorphous silicon, consisting of 2885 atoms, with N^+ ions having energies between 50 and 200 eV.

As a result of their simulations they reported that the uptake of nitrogen in the films depends on the incident ion energies. Until about the first 500 N^+ ions are deposited over an area of 473 $Å^2$, most incident ions remain on the surface and the deposition is not sensitive to the incident energy. After this first region, the number of deposited nitrogen atoms stays nearly constant with increasing number of incident N^+ ions for a given energy. In addition, more nitrogen atoms are deposited with increasing incident ion energies. This behaviour can be seen in Figure 2.5. Experimental studies by Park *et al.* [119] showed a similar raise in deposited N^+ ions with increasing incident ion energies. Their results are displayed in Figure 2.6. Similar experimental results have been published by Kim *et al.* [69] and Patra *et al.* [68] who have reported that the nitrogen content in their films increased with increasing particle energies. The saturation of nitrogen in the films

at a certain surface concentration can be attributed to competing effects of self-sputtering, scattering and penetration. All three contributions to the total number of incident atoms is shown in Figure 2.7. Similar results were observed in experimental studies by Park *et al.* [119].

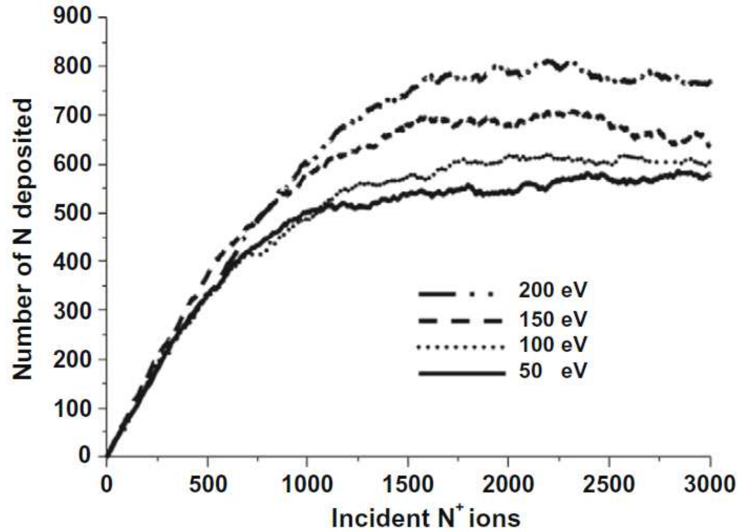

Figure 2.5: Number of N atoms accumulated on the surface at 300 K as a function of the number of incident N^+ ions for ion energies of 50, 100, 150 and 200 eV. [103]

During the MD simulations by Gou *et al.* [103] the N^+ ions that reached the silicon surface broke some of the silicon–silicon bonds and formed silicon–nitrogen bonds. By looking at the bond formation they showed that almost all silicon atoms were fully saturated by nitrogen and silicon atoms and only a few silicon dangling bonds were present. In contrast, the nitrogen atoms were less saturated leading to a number of nitrogen dangling bonds. In all their simulations the SiN_4 bond formation was dominant over the SiN_1, SiN_2, and SiN_3 bond formation for all silicon atoms. This dominance was even increased with higher deposition energies and agrees with experimental studies by Kusunoki *et al.* [120]. For the nitrogen atoms, not the NSi_3

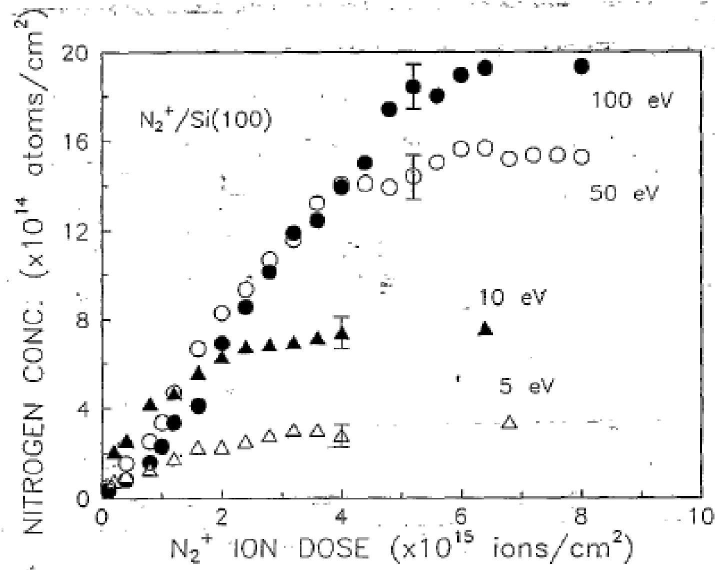

Figure 2.6: Nitrogen surface concentration measured as a function of N_2^+ dose at several impact energies. [119]

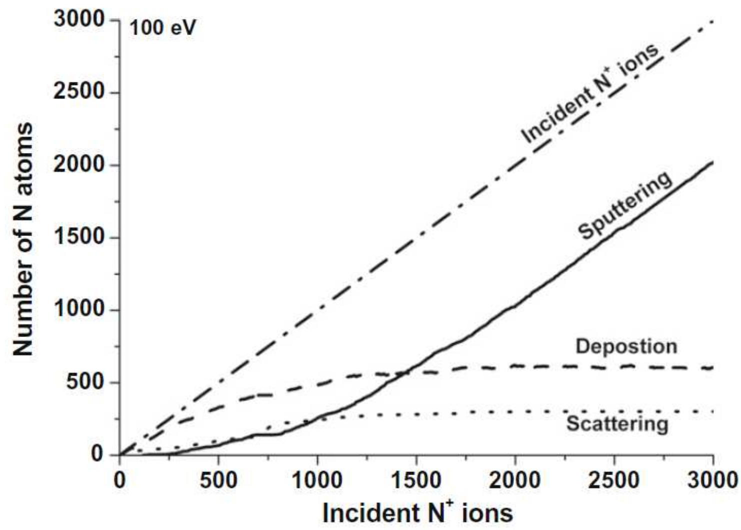

Figure 2.7: Cumulative number of incident N^+ ions, self-sputtering, deposition and scattering events during bombardment as a function of the number of incident N^+ ions for 100 eV at 300 K. The number of incident N+ ions is equal to the sum of self sputtering, scattering and deposition. [103]

bond formation, which is present in the stoichiometric Si_3N_4 structures, but the NSi_2 bond formation was the most frequent one. This bond formation also increased with raising incident energy. Hence, the simulations by Gou *et al.* predicted a nitrogen-rich nitride layer formation.

The unphysically high number of nitrogen dangling bonds, the nitrogen bonding environments which differ from experimentally observed structures, and the nitrogen-rich surface were all partially due to the prohibition of nitrogen-nitrogen bond formation by the model. Since N_2 formation at and N_2 desorption from the surface has been observed experimentally [119], Gou *et al.* introduced an attractive nitrogen-nitrogen term. However, this unphysically removed almost all nitrogen atoms from the surface by building N_2 molecules. Therefore, the interatomic potential introduced by de Brito Mota [104] leads to unphysical results of the description of the surface during growth simulations.

2.2.2 Vashishta potential

The Vashishta potential [21] consists of two-body and three-body terms, similar to the form proposed by Stillinger and Weber [121]. It was first introduced for silicon oxide [21] and was later extended to silicon nitride [95, 122]. No derivation for the potential form is given. However, effects from steric repulsion due to atomic sizes, screened ionic Coulomb interaction caused by charge transfer, and charge-dipole interaction caused by the electronic polarizability enter the two-body term, and bond bending and bond stretching due to the covalent nature of the bonds enter the three-body term [21, 122].

Comparisons between molecular dynamics simulation results using this potential and experimental results showed that bond lengths for both crystalline and

amorphous Si_3N_4 are in good agreement, the static structure factor is in agreement with neutron-scattering experiments, and elastic properties are within 10% from experimental data [96]. However, no comment about whether the model has been fitted to reproduce these properties could be found in Refs. [21, 95, 96, 100, 122–126] and references therein.

Although the Vashishta potential for silicon nitride has been used to study crack propagation and surfaces [95], pores and interfaces [96], amorphous silicon nitride [124], dynamic fracture [100], and shearing deformation [98], the potential's transferability to structures or environments not included in the fitting database is poor. For example, when modelling the interface between silicon and Si_3N_4 [127], the silicon atoms in silicon bulk, silicon nitride bulk, and the interface were all treated differently. This casts doubt on its ability to model realistically the growth of silicon nitride on a silicon substrate. To our knowledge, the Vashishta potential for silicon nitride was only applied once [102] to study the film growth of silicon nitride by molecular dynamics simulations. Unfortunately, only results of the mean cluster size but no results of local atomic environments, microstructural features, surface reconstructions or bulk properties resulting from deposition were reported.

Si-N growth simulation

Similar to the Tersoff potential, the Vashishta potential seems to be rarely applied in simulating Si-N growth. In 2001 Guo *et al.* [102] applied the Vashishta potential to study the film growth of Si-N by MD simulations. The results of their early growth kinetics investigation support the theory of film growth by Beysens [128]. The film growth showed three sequential steps: cluster formation followed by cluster coalescence and three-dimensional growth. Figure 2.8 shows the evolution of the

mean cluster size $\langle n \rangle$ with deposition time t for different substrate temperatures T_{sub} and particle kinetic energies E_k. It can be seen that the data follow a power law in two distinct steps characterised by two different exponents. The deposition time t_0 corresponds to the time at which the clusters begin to coalesce.

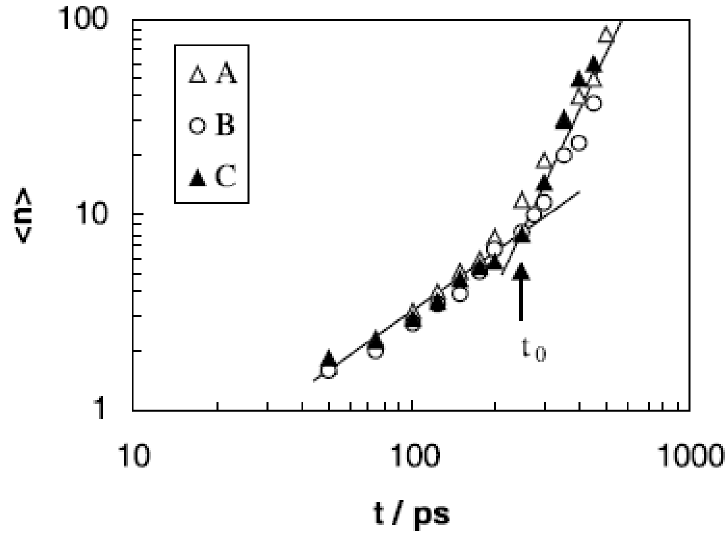

Figure 2.8: Evolution of the mean cluster size $\langle n \rangle$ with deposition time t: (A) T_{sub} = 300 K, E_k = 0.1 eV; (B) T_{sub} = 300 K, E_k = 10 eV; (C) T_{sub} = 1000 K, E_k = 0.1 eV [102].

Moreover, deposition parameters were found to have an influence on the film growth. For instance, raising the substrate temperature and the incoming atom's kinetic energy increased the mean cluster size $\langle n \rangle$ and hence, assuming that larger clusters result into denser films, also the density of the deposited films. Figure 2.9 shows the effect of the substrate temperature T_{sub} on the mean cluster size $\langle n \rangle$ with increasing atom coverage of the substrate Θ. The higher substrate temperature leads to an increase in cluster size. This can be explained by higher atom mobility on the surface and hence atoms can find energetically more favourable sites on existing

clusters. These results are in good agreement with experimental studies [68, 69, 129], in which denser films were achieved with higher substrate temperatures. The effect of the impact energy on the mean cluster size $\langle n \rangle$ with increasing atom coverage Θ is shown in Figure 2.10. Higher impact energies result into larger cluster sizes and hence denser films. This is also in good agreement with experimental studies [68, 69].

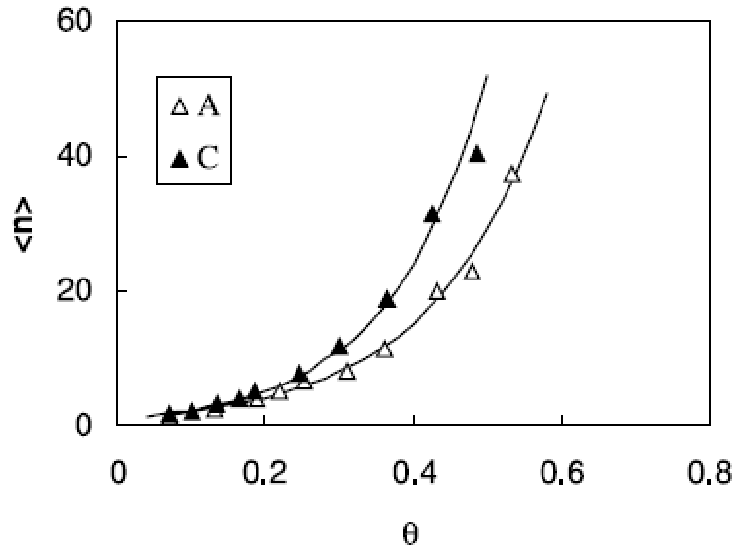

Figure 2.9: Effect of the substrate temperature T_{sub} on the mean cluster size $\langle n \rangle$ with increasing atom coverage Θ (in fractions of one monolayer (ML)): (A) T_{sub} = 300 K, E_k = 0.1 eV; (C) T_{sub} = 1000 K, E_k = 0.1 eV [102].

Unfortunately, Guo *et al.* only investigated the mean cluster size but did not show any results of local atomic environments, microstructural features, surface reconstructions or from deposition resulting bulk properties. Consequently, evidence of the robustness of the Vashishta potential for Si-N growth simulations cannot be found in the literature.

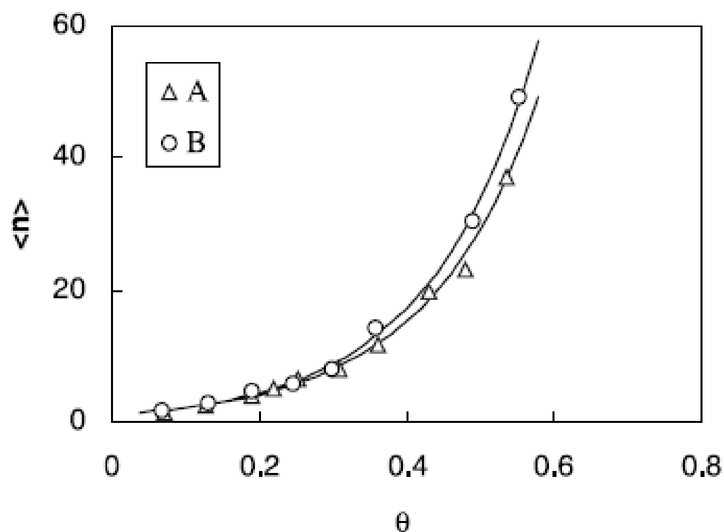

Figure 2.10: Effect of the impact energy on the mean cluster size ⟨n⟩ with increasing atom coverage Θ: (A) T_{sub} = 300 K, E_k = 0.1 eV; (B) T_{sub} = 300 K, E_k = 10 eV [102].

2.2.3 Reactive force fields

The reactive force field (ReaxFF) class of empirical interatomic potentials describes the forming and breaking of bonds by using σ and π bond orders that are distance dependent and was first developed for hydrocarbons by van Duin *et al.* [105]. It has been extended to many systems, including silicon and silicon oxide [130]. The original parameterisation for silicon nitride required nearly fifty fitting parameters and used only a limited training set [131]. Errors in the Si-O-N parametrisation from 2004 discussed in Ref. [132] include an excessive N-N dimerisation and under-coordinated silicon atoms in the β Si_3N_4 structure. This ReaxFF parametrisation predicted unphysically that the stable β Si_3N_4 phase was metastable due to the overestimation of the π character of the Si-N bonds. In the more recent 2006 version [132], the bond lengths at which π bonding becomes significant were manually

adjusted, and N-N π and double π bonding was prohibited, because of the N-N dimerisation in the solid state mentioned above. The new parameterisation is therefore not transferable to molecular systems involving double or triple bonded nitrogen (e.g. N_2). Moreover, torsional terms are not included in the ReaxFF for the Si-N system. Unfortunately, no simulation proving the successful application of the Si-N ReaxFFs parameterisation to modelling surface reconstructions or film deposition can be found in the literature.

2.2.4 Bond-based bond-order potentials

Pettifor *et al.* [133–136] have gone beyond the Tersoff empirical bond order form by deriving an analytic form directly from a tight binding (TB) Hamiltonian. These bond order expressions explicitly describe the σ and π bonding with associated angular interactions, are more environment dependent than the Tersoff potential by including fourth moment rather than only second moment contributions, and are suitable for large-scale atomistic simulations [27]. Bond-based bond-order potentials (BOPs) have been proven to describe several covalent systems successfully [29, 30] (Si and GaAs) and have been used to model film growth [27, 137–139] (Si, GaAs, and hydrocarbons).

Film growth simulations

For modelling film deposition processes, cluster, surface, and bulk properties have to be described by the interatomic potential accurately. Bond-based BOPs for hydrocarbons [137], Si [30], and GaAs [29] have successfully described film growth that is in good agreement with experiments [27, 137–139].

Gillespie *et al.* [30, 138] modelled silicon growth using a bond-based BOP. It

was reported that an increase in temperature results in an improvement in film crystallinity. Figure 2.11 shows three simulation snapshots at 600, 800, and 900 K and the increase in crystallinity with increasing temperature. This increase is in good agreement with experimental results [140].

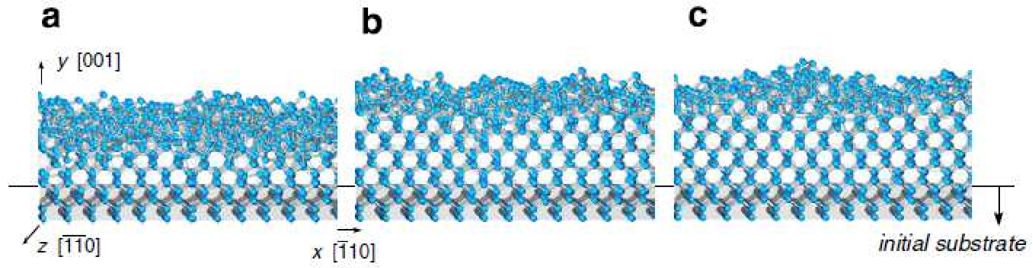

Figure 2.11: Simulated atomic structure of the Si films. (a) T = 600 K, (b) T = 800 K, and (c) T = 900 K. (Figure modified from [27].)

Murdick *et al.* [29, 139] performed BOP simulations of the growth of gallium arsenide (GaAs) films from As_2 and Ga vapour fluxes using a wide range of deposition conditions that cover substrate temperatures between 500 K and 1500 K, and As:Ga flux ratios between 0.9 and 3.4. They investigated the effects of substrate temperature and vapour flux ratio effects on the atomic structure of the GaAs film. Figure 2.12 shows four simulation snapshots at various substrate temperatures and flux ratios. An improvement in film crystallinity can be seen with increasing substrate temperature. The highest crystallinity was observed at a flux ratio of 3.14. This is in good agreement with experiments, since As_2 molecules form and evaporate from As-rich surfaces. It seems that BOPs are able to describe the experimentally observed balance between single As atom deposition and incorporation into the film and formation and desorption of As_2 molecules, which the empirical potential of the Tersoff functional form developed by de Brito Mota *et al.* [104] in the case of N_2 failed to describe (see Subsection 2.2.1). This ability of the BOP can be attributed to

the well predicted relative low energy of the As_2 molecule with respect to an isolated or condensed arsenic atom. Furthermore, it was observed that the As_2 evaporation increased with increasing growth temperature leading to gallium-rich surfaces at high simulation temperatures and near unity As:Ga flux ratios. At high flux ratios and high growth temperatures arsenic atoms first condensed on the substrate and some of them later desorbed leading to stoichiometric gallium arsenide films. A composition of $GaAs_X$ with $x > 1$ was only observed at low growth temperatures and high As:Ga flux ratios. All the observed effects are in good agreement with experimental results from the literature [141–144].

Mrovec *et al.* [137] reported MD simulations of the growth of an a-C:H film during deposition of acetylene (C_2H_2) molecules using a bond-based BOP for the hydrocarbon system. They reported an increase in sp^3 content in the films and an increase in penetration depth both with increasing acetylene kinetic energies. For simulations with energies per carbon atom of 25 eV and 100 eV the sp^3 concentration in the substrate increased during the deposition from 2.9% to 6.9% and 9.1%, respectively. In the simulations with the lower energy per carbon atom the increase of sp^3 content was localized only in the surface region and the remaining film differed only slightly from the initial substrate. In the simulations with higher energy per carbon atom, the sp^3 bonded atoms in the final structure were distributed uniformly throughout the whole film. This effect can be explained by the increase in maximum penetration depth for the acetylene molecules with increasing kinetic energies per carbon atom. Low energies led to small penetration depths and hence to transformations only in the surface region, whereas higher energies led to changes in the whole film. Other effects of the energy per carbon atom were reported. For instance, with increasing energy more long carbon chains were sticking out of the

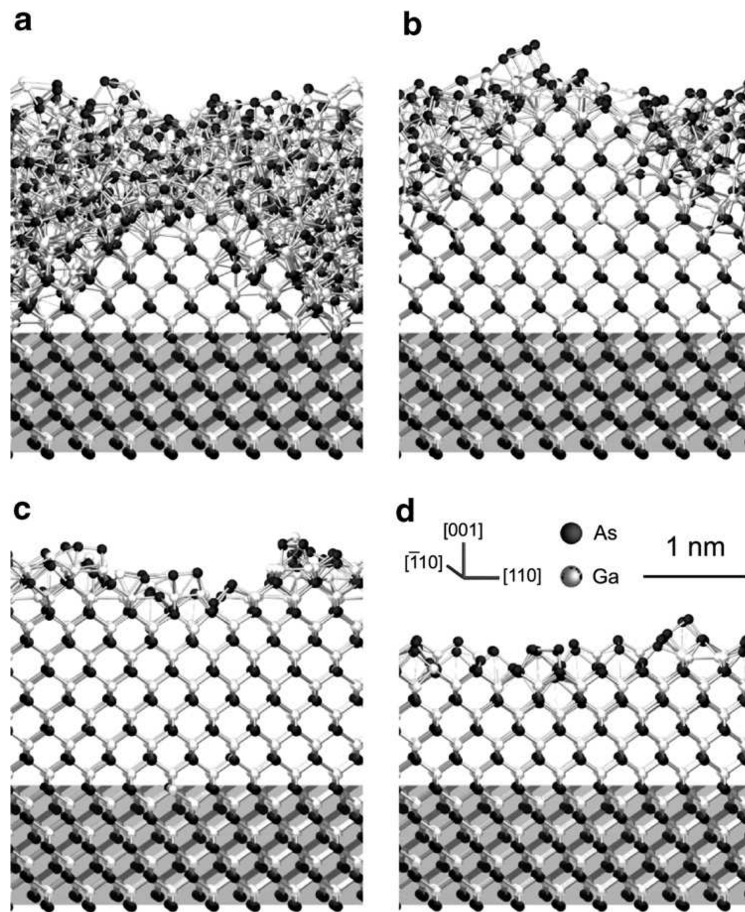

Figure 2.12: Simulated atomic structures of the GaAs films after 10 ns of deposition at different substrate temperatures T and As:Ga flux ratios R. (a) T = 500 K, R = 1.14; (b) T = 800 K, R = 1.19; (c) T = 1100 K, R = 1.67, and (d) T = 1500 K, R = 3.14. [27]

surface and the content of sp^1 bonded atoms in the surface region was increased. Also, the formation of local craters was favoured and the number of sputtered atoms was increased with increasing energy.

All the above mentioned results are in good agreement with experimental studies and show that BOPs are suitable for simulating film growth of covalent systems, since they are able to describe clusters, bulk structures, point defects, surface reconstructions, and melting temperatures better than other potentials. Hence, it can be assumed that a new bond-based BOP for silicon nitride can improve the description of silicon nitride growth simulations with currently employed potentials. For instance, a BOP for silicon nitride could provide corrections for the high number of nitrogen dangling bonds, the wrong nitrogen bonding environments, and the nitrogen-rich surface observed in the studies by de Brito Mota *et al.*. However, a challenge in developing this BOP could be that it is able to differentiate between the energetically very close α and β structures which have identical local atomic environments but different long range interactions. BOPs, like the ones used in the film growth simulations described above, can be derived by coarse-graining the electronic structure from DFT via the TB approximation. Therefore, the existence of a high quality TB model for silicon nitride is crucial for a successful BOP for silicon nitride. In this thesis we provide a reduced TB model for silicon nitride which provides valuable input for the future development of a BOP for silicon nitride. The theory necessary to develop a reduced TB model and a BOP is described in Sections 2.3 and 2.4.

2.2.5 A note on growth simulations

A common problem all MD simulations of film growth share is that using reasonable time steps for simulating deposition processes leads to very high deposition rates compared to experiments. Furthermore, no simulations in the literature have reached steady state growth rates due to limited computing speed. All this is due to the fact that deposition processes take place over a time scale which is much longer than that which can be reached with traditional molecular dynamics. This can lead to wrong surface reconstructions if the deposited atoms do not have enough time to diffuse to their preferred positions. Therefore, several suggestions for improving time- and length-scale issues have been made [145–147]. For dynamical systems, assigning a region of physical space to each processor is an efficient way to extend the accessible size scale of MD simulations to up to 10^{10} atoms. However, increasing the time scale is a more demanding task. Several MD accelerating methods can be found in [148]. Moreover, adaptive kinetic Monte Carlo (aKMC), where the relevant transitions are found on the fly during the simulation, can be applied in combination with classical dynamics [149]. With this approach the time interval between deposition events can be modelled with aKMC and the deposition event itself can be simulated with ordinary classical dynamics. This is an efficient way to increase the time scale.

2.3 Systematic Derivation of Interatomic Potentials

Interatomic potentials can be derived by coarse graining the electronic structure from density functional theory (DFT) via the tight binding (TB) approximation towards bond-order potentials (BOPs). The following three Subsections give a short introduction to the individual methods employed within this process. Section 2.4 then describes the different coarse graining steps which link these methods. Generally, density functional theory (DFT) is the most accurate method which is, however, not able to reach the time and length scales accessible by BOPs. The tight binding (TB) approximation lies with accuracy and efficiency between DFT and BOPs. The theoretical bridging of time and length scales allows us to fine tune less accurate but computationally more efficient methods on smaller length scales, by for example comparing formation energies of interstitials and vacancies with results from more accurate methods and experimental results, and then use the fine tuned but less accurate methods at larger length scales for calculating for example dislocations and deposition processes.

2.3.1 Density functional theory (DFT)

To simulate nanocoating materials as robustly as possible, the electronic structure must be described accurately. To calculate the electronic structure of materials, in principle, the time-independent many-electron Schrödinger equation needs to be solved, where the system consists of nuclei that can be considered to be fixed in space (Born-Oppenheimer Approximation) and electrons responding to the potential generated by the nuclei and electrons,

$$\hat{H}\Psi(\mathbf{r}_1, \mathbf{r}_2, ..., \mathbf{r}_N) = U_{tot}\Psi(\mathbf{r}_1, \mathbf{r}_2, ..., \mathbf{r}_N). \tag{2.1}$$

$\hat{H}$ is the many-body Hamiltonian, Ψ the electronic wave function (depending on the coordinates of all N electrons), and U_{tot} represents the total energy of the system. Since the many-electron Schrödinger equation cannot be solved analytically and a numerical solution is computationally very expensive for more than a few electrons, simplifications of the many-electron Schrödinger equation are needed for electronic structure calculations of larger systems. Density functional theory [150, 151] simplifies the many-electron Schrödinger equation to a set of effective one-electron Schrödinger equations,

$$\left(-\frac{1}{2}\nabla^2 + V_{eff}\right)\psi_n(\mathbf{r}) = E_n\psi_n(\mathbf{r}), \tag{2.2}$$

also known as the Kohn-Sham equations [151], where n labels the eigenvalues and eigenfunctions (or eigenstates) of the single-particle Hamiltonian. The first part of the single-particle Hamiltonian is the kinetic energy, whereas the second part gives the effective potential V_{eff}, in which a set of non-interacting electrons move, namely

$$V_{eff}(\mathbf{r}) = V_{ion}(\mathbf{r}) + V_H(\mathbf{r}) + V_{xc}(\mathbf{r}). \tag{2.3}$$

$V_{ion}(\mathbf{r})$ is the Coulomb potential due to the ionic cores, $V_H(\mathbf{r})$ is the Hartree potential resulting from the average electronic charge distribution, and $V_{xc}(\mathbf{r})$ is the exchange-correlation potential, which results from electron-electron correlations neglected in the Hartree approximation and whose exact form is unknown. Several approximations, including the local density approximation (LDA, [151]) and the generalised gradient approximation (GGA, [152]), can be used to estimate the exchange-correlation energy functional $U_{xc}[\rho(\mathbf{r})]$ which relates to the exchange-correlation

potential through the functional derivative as [153]

$$V_{xc}(\mathbf{r}) = \frac{\delta U_{xc}\left[\rho(\mathbf{r})\right]}{\delta\rho(\mathbf{r})}. \tag{2.4}$$

All contributions to the total energy can be expressed as unique functionals of the electron density $\rho(\mathbf{r})$, which is determined from the normalised one-electron wave functions,

$$\rho(\mathbf{r}) = \sum_n f_n \left|\psi_n(\mathbf{r})\right|^2, \tag{2.5}$$

with f_n being a factor defining the occupancy of each state. The electron density that minimises the total energy to the ground state energy of the system U_0 is called the ground state electron density $\rho_0(\mathbf{r})$. In order to find this particular electron density for fixed atomic positions, the set of Eqs. (2.2) must be solved self-consistently. This is because $V_H(\mathbf{r})$ and $V_{xc}(\mathbf{r})$ both, and hence $V_{eff}(\mathbf{r})$, depend on the charge density $\rho(\mathbf{r})$ which can only be obtained from the solutions $\psi_n(\mathbf{r})$. In practice, this self-consistency problem is solved as follows. First, an input electron density $\rho_{in}(\mathbf{r})$ is guessed from which the Hartree potential is obtained through the Poisson equation and the exchange-correlation potential is approximated with, for example, LDA or GGA. Second, the set of Eqs. (2.2) is solved using the effective potential obtained in the first step. Third, the solutions are a set of eigenstates and an output electron density $\rho_{out}(\mathbf{r})$ is calculated according to Eq. (2.5). The self-consistency loop is closed by guessing a new input electron density from the obtained output electron density, and self-consistency is reached when the difference between two output charge densities or total energies of two consecutive iterations is smaller than a given tolerance [154].

DFT is an approach that provides a significant simplification to quantum-mechanical calculations in that the calculation of ground state energies and forces requires the minimisation of a functional of the electron density only. Nevertheless, many materials phenomena arise from microstructural events that occur on length and time scales which DFT simulations cannot access. A first step of coarse graining towards the atomistic level can be done by obtaining TB parameters from mixed-basis DFT projections of wave functions onto a minimal basis of atom-centred orbitals (see Subsection 2.4.1).

2.3.2 Tight binding (TB) approximation

In orthogonal tight binding (TB), the eigenstates ψ_n of the Hamiltonian are expanded in an orthogonalised basis of atomic-like orbitals $\phi_{i\alpha}$,

$$\psi_n = \sum_{i\alpha} c_{n,i\alpha} \phi_{i\alpha}, \tag{2.6}$$

where α labels the orbital (e.g. s, p, or d) centred on atom i and $c_{n,i\alpha}$ are the expansion coefficients for the eigenstates n of the Hamiltonian. $\phi_{i\alpha}$ will be abbreviated with $i\alpha$ from here on. The DFT Hamiltonian is represented by a parametrised TB Hamiltonian matrix, where the matrix elements

$$H_{i\alpha j\beta} = \langle i\alpha | \hat{H} | j\beta \rangle \tag{2.7}$$

are written with respect to the valence orbitals $|i\alpha\rangle$ and $|j\beta\rangle$ and describe interactions between the atomic orbital basis functions. For the particular example of

$\alpha = s$ on atom i and $\beta = s$ on atom j, Eq. (2.7) gives

$$ss\sigma_{ij} = H_{isjs} = \langle is| \hat{H} |js\rangle . \tag{2.8}$$

Hence, similar to Eq. (2.2) for DFT we have the TB single-particle Schrödinger equation

$$\hat{H}\psi_n = E_n\psi_n. \tag{2.9}$$

In TB only the valence orbitals are assumed to contribute to the bonding on each site. For the case of sp-valent elements these are typically taken to be one s and three p orbitals per atom. For the case of transition metal elements a minimum of five d orbitals per atom are used. Usually, only first and at times second nearest neighbour interactions between these orbitals are included in the Hamiltonian matrix elements, hence the name tight binding.

The sp-valent TB Hamiltonian matrix elements within the two-centre approximation [155] can be expressed in terms of the on-site atomic energy levels, the two-centre bond integrals $ss\sigma$, $sp\sigma$, $ps\sigma$, $pp\sigma$, and $pp\pi$ (where the first and second indices refer to the first and second orbital respectively and the third index to the type of bond), and the direction cosines of a vector pointing along the bond length from atom i to atom j. Thus, for an orthogonal TB model the following inputs, which are in general functions of interatomic distance, are required: the on-site levels, the bond integrals, and the repulsive term.

In general TB calculations are faster than DFT calculations, because the Hamiltonian which needs to be diagonalised is smaller and sparse. This allows TB calculations to sample larger length and time scales. A further step towards the

atomistic level can be done by deriving BOPs from the TB model by a further coarse graining step.

2.3.3 Bond-order potentials (BOPs)

Bond-order potentials (BOPs) rely heavily on the concept of the moments of the local density of states (LDOS). The pth moment $\mu_{i\alpha}^{(p)}$ of the LDOS $n_{i\alpha}(E)$ projected onto atom i and orbital α is defined as [156],

$$\mu_{i\alpha}^{(p)} = \int E^p n_{i\alpha}(E)\, dE. \tag{2.10}$$

In general, moments are a quantitative measure of any distribution and are related to the distribution's mean, variance, and skewness, for example. Increasing the number of moments that are included leads to a better description of the distribution under consideration [33]. Following Cyrot-Lackmann [157], the moments of the LDOS can be written as the sum over all bonding paths of length p that start and finish on the same atom i and orbital α,

$$\mu_{i\alpha}^{(p)} = \sum_{j_1\beta_1,\dots,j_{p-1}\beta_{p-1}} H_{i\alpha j_1\beta_1} H_{j_1\beta_1 j_2\beta_2} \dots H_{j_{p-1}\beta_{p-1} i\alpha}, \tag{2.11}$$

where $H_{i\alpha j\beta}$ is the Hamiltonian matrix element between orbital α on atom i and orbital β on atom j. This approximation directly links the LDOS to the local atomic environment. The fact that moment expansions are slow to converge led Haydock *et al.* [158] to propose using the Lanczos recursion algorithm [159] to write the *on-site* (or *diagonal*) Green's function elements

$$G_{i\alpha i\alpha}(E) = \left\langle i\alpha \middle| \left(E - \hat{H}\right)^{-1} \middle| i\alpha \right\rangle \tag{2.12}$$

as a continued fraction

$$G_{i\alpha i\alpha}(E) = \cfrac{1}{E - a_0 - \cfrac{b_1^2}{E - a_1 - \cfrac{b_2^2}{E - a_2 - \cfrac{b_3^2}{\ddots}}}} \tag{2.13}$$

where the moments are grouped to give the recursion coefficients a_n, b_n. The first recursion coefficients in terms of the moments can be written as,

$$\begin{aligned}
a_0 &= \mu_1 \equiv 0, \\
b_1 &= \sqrt{\mu_2}, \\
a_1 &= \mu_3/\mu_2, \\
b_2 &= \sqrt{\mu_4/\mu_2 - \mu_3^2/\mu_2^2 - \mu_2}, \\
a_2 &= \left[\mu_5 - 2\mu_3\left(\mu_4/\mu_2 - \mu_3^2/\mu_2^2\right) - \mu_3^3/\mu_2^2\right] / \left[b_1^2 b_2^2\right],
\end{aligned} \tag{2.14}$$

where we have taken the centre of gravity μ_1 of the LDOS [160]

$$n_{i\alpha}(E) = -\frac{1}{\pi} \operatorname{Im}\left\{G_{i\alpha i\alpha}(E)\right\} \tag{2.15}$$

to be the energy zero. However, the bond order $\Theta_{i\alpha j\beta}$, from which the bond-based BOPs are then derived, depends on the *inter-site* (or *off-diagonal*) Green's function elements $G_{i\alpha j\beta}$,

$$G_{i\alpha j\beta}(E) = \left\langle i\alpha \left| \left(E - \hat{H}\right)^{-1} \right| j\beta \right\rangle, \tag{2.16}$$

as

$$\Theta_{i\alpha j\beta} = -\frac{2}{\pi} \operatorname{Im} \left\{ \int_{-\infty}^{E_F} G_{i\alpha j\beta} \left(E \right) dE \right\}. \tag{2.17}$$

Unfortunately, in contrast to the fast convergence of the *on-site* Green's function elements, the *inter-site* Green's function elements converge only slowly with respect to the number of exact recursion levels. A crucial step was done by Aoki and Pettifor [161, 162] who evaluated the *off-diagonal* Green's function matrix elements in terms of the derivatives of the *diagonal* Green's function matrix elements,

$$G_{i\alpha j\beta} = \frac{\partial}{\partial \lambda} G_{00}^{\lambda}, \tag{2.18}$$

where

$$G_{00}^{\lambda} = \left\langle u_0^{\lambda} \middle| \hat{G} \middle| u_0^{\lambda} \right\rangle = \frac{1}{2} \left(G_{i\alpha i\alpha} + G_{j\beta j\beta} \right) + \lambda G_{i\alpha j\beta}, \tag{2.19}$$

and

$$\left| u_0^{\lambda} \right\rangle = \frac{1}{\sqrt{2}} \left(\left| i\alpha \right\rangle + e^{i\phi} \left| j\beta \right\rangle \right), \tag{2.20}$$

and

$$\lambda = \cos \phi. \tag{2.21}$$

Thus, λ is a phase factor difference between the orbitals α and β on atoms i and j, respectively. $\left| u_0^{\lambda} \right\rangle$ is the initial basis from which the Lanczos algorithm can determine

an orthonormal recursion basis $\left|u_n^\lambda\right\rangle$ and recursion coefficients a_n^λ and b_n^λ such that

$$b_{n+1}^\lambda \left|u_{n+1}^\lambda\right\rangle = H\left|u_n^\lambda\right\rangle - a_n^\lambda \left|u_n^\lambda\right\rangle - b_n^\lambda \left|u_{n-1}^\lambda\right\rangle, \tag{2.22}$$

with $\left|u_{-1}^\lambda\right\rangle \equiv 0$.

Equation (2.18) is the key equation in bond-based BOP theory. By retaining up to four moments or hopping paths of length four the σ and π bond orders for half-full valence bands may be written as [134–136, 163]

$$\Theta_{\sigma ij}^{(\frac{1}{2})} = 1/\sqrt{1 + \frac{2\Phi_{2\sigma} + R_{4\sigma ij} + \widetilde{\Phi}_{2\sigma i}\widetilde{\Phi}_{2\sigma j}\left(2 + \widetilde{\Delta\Phi}_{4\sigma}\right) + \hat{\delta}_i^2}{\left(1 + \widetilde{\Delta\Phi}_{4\sigma}\right)^2}}, \tag{2.23}$$

and

$$\Theta_{\pi\pm ij}^{(\frac{1}{2})} = 1/\sqrt{1 + \left(\Phi_{2\pi} \mp \sqrt{\Phi_{4\pi}}\right)}. \tag{2.24}$$

$\hat{\delta}_i$ is the normalised on-site energy level splitting, with $\hat{\delta}_i = \delta_i/(\sum_{j,j\neq i}\beta_{\sigma ij})$. $\delta_i = (E_{pi} - E_{si})$ is assumed to be environment independent and $\beta_{\sigma ij}$ is the σ reduced TB bond integral between sites i and j. The Φ and R terms describe different hopping contributions as in Figure 2.13, the subscripts 2 and 4 give the number of paths, and σ and π the type of bonding. The total bond order Θ_{tot} can be calculated by adding the individual contributions,

$$\Theta_{tot} = \Theta_\sigma + \Theta_{\pi+} + \Theta_{\pi-}. \tag{2.25}$$

Whereas on the TB level the bond order matrix elements written with respect to

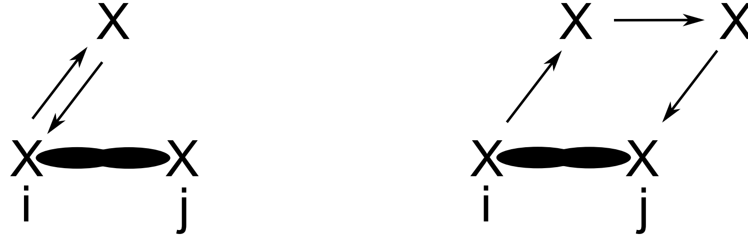

Figure 2.13: Hopping path contributions $\Phi_{i,2}$ and $R_{ij,4}$ that are taken into account for the evaluation of the analytic BOP.

the valence orbitals $|i\alpha\rangle$ and $|j\beta\rangle$

$$\Theta_{i\alpha j\beta} = \langle i\alpha| \hat{\Theta} |j\beta\rangle \tag{2.26}$$

are related to the off-diagonal elements of the density matrix as

$$\Theta_{i\alpha j\beta} = 2\rho_{i\alpha j\beta}, \tag{2.27}$$

on the bond-based BOP level the bond order contributions consist of analytic expressions as in Eqs. (2.23) and (2.24) that determine the ij bond strength depending on the local environment.

2.4 Methodology

In the previous Section we gave a short introduction to density functional theory (DFT), the tight binding (TB) approximation, and bond order potentials (BOPs). This Section is devoted to the different coarse-graining steps which link the previously discussed methods.

2.4.1 From DFT to TB

Orthogonal TB bond integrals

The distance dependent two-centre orthogonal TB bond integrals for silicon, nitrogen, and silicon nitride employed in this thesis were obtained from mixed-basis DFT projections of wave functions onto a minimal basis of atom-centred orbitals by Martin Reese with the projection method developed by Martin Reese, Matous Mrovec, Christian Elsässer, Alexander Urban, and Bernd Meyer [31]. This method can be used to extract non-orthogonal as well as orthogonal TB parameters, and can, in principle, be applied to single- and multi-component systems of any chemical composition [31, 32]. First applications of this projection method include the binary systems silicon carbide, titanium carbide, and titanium nitride [164, 165].

In the projection scheme, non-orthogonal atom-centred orbitals are written in terms of radial functions $f_{i\alpha}(r)$ and spherical harmonic functions $Y_\alpha(\mathbf{r})$,

$$\phi_{i\alpha}(\mathbf{r}) = f_{i\alpha}(r)\, Y_\alpha(\mathbf{r}), \tag{2.28}$$

where r is the radial distance, $\mathbf{r}$ is the position in space, and α comprises the usual indices l and m. The core of the projection scheme is the optimization of the radial functions, which are flexible in shape and range, such that the loss of electrons

is minimised when projecting the DFT wave functions $\psi_n(\mathbf{r})$ from self-consistent plane wave calculations onto the optimised atom-centred orbitals $\phi_{i\alpha}(\mathbf{r})$ for one or more chosen reference atomic configurations. The loss of electrons by going from DFT to TB during the projection is known as spillage. Clearly, the spillage is smaller for a structure when the radial functions are optimised for that particular structure and volume. However, results for carbon show [31] that the electronic band energy is nonsensitive to the re-optimization of the radial function, even the band energy of structures and volumes not included in the optimization process shows no dependence on small spillage differences.

With the aid of the optimised minimal basis of atom-centred orbitals with fixed radial functions and the self-consistent Hamiltonian of the plane-wave DFT calculation the non-orthogonal TB Hamiltonian and overlap matrix elements are then obtained for individual atomic interactions in a number of structures. For orthogonal TB, where the overlap matrix is the identity matrix, the bond integrals are then obtained via the Löwdin symmetric orthogonalization [166] from the non-orthogonal TB Hamiltonian and overlap matrix elements.

Binding Energy

For the development of the reduced TB models we use DFT binding energy curves of a structure database as a benchmark. The computational details of the DFT calculations are described in Subsection 2.4.4. Including charge transfer (CT), the TB binding energy takes the form given in Eq. (2.47) where $q_i \neq 0$ is the additional charge per atom compared to the isolated atom. It simplifies to the local charge neutrality (LCN) form in Eq. (2.29) for $q_i = 0$.

For the elemental silicon and elemental nitrogen systems it is often a reasonable

description to assume LCN. In this case, the binding energy can be expressed as [28],

$$U_B^{(LCN)} = U_{bond} + U_{prom} + U_{rep} + \Delta U_{atom}, \tag{2.29}$$

where the bond energy can be written in the on-site representation as,

$$U_{bond} = 2 \sum_{i\alpha} \int_{-\infty}^{E_F} (E - E_{i\alpha}) \, n_{i\alpha}(E) \, dE. \tag{2.30}$$

E_F is the Fermi energy, $E_{i\alpha}$ is the on-site energy level, and $n_{i\alpha}(E)$ is the local density of states (LDOS) projected onto atom i and orbital α for both up and down spins. Alternatively, the bond energy can be written in the *inter-site* representation as a sum over contributions from individual bonds between atomic sites i and j,

$$U_{bond} = \sum_{i,j:i<j} U_{bond,ij}, \tag{2.31}$$

with

$$U_{bond,ij} = 2 \sum_{\alpha,\beta} H_{i\alpha j\beta} \Theta_{j\beta i\alpha}. \tag{2.32}$$

The expression is multiplied by two to account for both bond energy contributions in the ij and ji direction and the assumed spin degeneracy of non-magnetic systems is inherent in the bond order elements as in Eq. (2.27).

U_{prom} is the energy contribution resulting from promoting electrons between different levels compared to the free atom occupation and is therefore associated

with the formation of hybrid orbitals [28],

$$U_{prom} = \sum_{i\alpha} E_{i\alpha}^{(0)} q_{i\alpha}. \tag{2.33}$$

$E_{i\alpha}^{(0)}$ is the reference level, which we take as the free atom on-site energy level, and $q_{i\alpha}$ is the difference between the number of electrons on a tightly bound and a free atom i and orbital α [28],

$$q_{i\alpha} = N_{i\alpha} - N_{i\alpha}^{(0)}, \tag{2.34}$$

with the number of electrons given by

$$N_{i\alpha} = 2 \int_{-\infty}^{E_F} n_{i\alpha}(E)\, dE. \tag{2.35}$$

Therefore, LCN on each atom i is met by

$$q_i = \sum_{\alpha} q_{i\alpha} = 0. \tag{2.36}$$

Both the repulsive pair potential and the two-centre bond integrals are represented by generalised GSP analytic functions [167, 168] $f_{GSP}(R)$ that are cut off smoothly from $R = R_{tail}$ by the exponential-cosine cutoff function $f_{cut}(R)$ that vanishes for $R = R_{cut}$. Thus,

$$f(R) = f_{GSP}(R) + f_{cut}(R), \tag{2.37}$$

where

$$f_{GSP}\left(R\right)=\left(\frac{R_0}{R}\right)^{n_a}\exp\left\{n_b\left[\left(\frac{R_0}{R_c}\right)^{n_c}-\left(\frac{R}{R_c}\right)^{n_c}\right]\right\}, \tag{2.38}$$

for $R < R_{tail}$, and

$$f_{cut}\left(R\right)=\frac{1}{2}f_0\exp\left\{\left(f_0'/f_0\right)\left(R-R_{tail}\right)\right\}\left[1-\cos\left(\pi\frac{R-R_{cut}}{R_{cut}-R_{tail}}\right)\right], \tag{2.39}$$

for $R_{tail} \leq R \leq R_{cut}$, with the matching boundary conditions

$$f_{cut}\left(R_{tail}\right)=f_{GSP}\left(R_{tail}\right)=f_0 \tag{2.40}$$

$$f_{cut}'\left(R_{tail}\right)=f_{GSP}'\left(R_{tail}\right)=f_0'. \tag{2.41}$$

The particular advantage of using the function in Eq. (2.39) lies in the fact that it can be applied to any function to be cut off without fitting. This function substitutes the original function over a range where the original function is not fitted and, in contrast to using a polynomial as in Xu's carbon model [169] and Kwon's silicon model [170], this function never changes sign. Equation (2.39) was suggested by the author of this thesis.

The repulsive energy is then approximated by

$$U_{rep}=\sum_i\left(\sum_{j:i<j}\phi_{ij}\left(R\right)\right)^{n_{d,i}}+\sum_{i,j:i<j}Y_{ij}\left(R\right) \tag{2.42}$$

with the repulsive pair potential

$$\phi(R) = \phi_0 f(R), \tag{2.43}$$

and a Yukawa-type core repulsion

$$Y(R) = a_c R^{-b_c} \exp(-c_c R). \tag{2.44}$$

The latter is needed at very short interatomic distances for the elemental silicon and the binary silicon nitride interactions to repel strongly enough to avoid fusion of silicon silicon and silicon nitrogen pairs. Note that nitrogen has no p core electrons while silicon does, and, therefore, has a softer core that allows the formation of dimeric N_2 as its ground state (see, e.g., §4.2 of Ref. [33]). This fact is not considered explicitly in the TB approximation. The Yukawa-type term is cut off smoothly in the same fashion as described above. $n_{d,i}$ in Eq. (2.42) is an embedding exponent. Similarly, for the bond integrals we have

$$\beta(R) = \beta_0 f(R), \tag{2.45}$$

with $n_a = n_b$ in Eq. (2.38).

ΔU_{atom} in Eq. (2.29) accounts for the upward shift of the non-magnetic DFT free atom reference energy compared to the magnetic free atom value due to the atom's spin configuration,

$$\Delta U_{atom} = \sum_i \Delta U_{atom,i}. \tag{2.46}$$

For most elemental systems LCN is a reasonable approximation. However, for the

binary silicon nitride system where the difference in electronegativity between silicon and nitrogen drives charge redistribution between the sites, the explicit inclusion of charge transfer (CT) is crucial. (The Pauling electronegativity values for silicon and nitrogen are 1.90 and 3.04 respectively.) This leads to the following expression for the binding energy

$$U_B^{(CT)} = U_{bond} + U_{prom} + U_{ion}^{intra} + U_{ion}^{inter} + U_{rep} + \Delta U_{atom}. \tag{2.47}$$

The bond, repulsive, and free atom terms take the same form as described above, but the promotion energy now takes the form (c.f. Eq. (85) Ref. [28]),

$$U_{prom} = \sum_{i\alpha} E_{i\alpha}^{(0)} \left(q_{i\alpha} - \Delta q_{i\alpha}\right). \tag{2.48}$$

$\Delta q_{i\alpha}$ is the charge taken from or put onto atom i and orbital α due to total charge transfer

$$q_i = \sum_{\alpha} \Delta q_{i\alpha} \tag{2.49}$$

between atoms, where $\Delta q_{i\alpha}$ is fixed by ensuring that the resulting change in atomic energy is minimised. In contrast, $q_{i\alpha}$ is the charge on atom i and orbital α following the self consistent optimization of the energy of the system. $q_{i\alpha}$ is equivalent to the definition in Eq. (2.34), although, the values of $N_{i\alpha}$ may differ from those when enforcing LCN due to non-zero values of $\Delta q_{i\alpha}$. Similar to the condition for Eq. (2.33) in Eq. (2.36), for each atom when allowing CT the following condition is met

$$\sum_{\alpha} \left(q_{i\alpha} - \Delta q_{i\alpha}\right) = 0. \tag{2.50}$$

This implies that the promotion energy when allowing CT is the result of promoting electrons between different levels compared to the free atom occupation after $\Delta q_{i\alpha}$ has been taken from or put onto atom i and orbital α.

U_{ion}^{intra} in Eq. (2.47) is the energy to form ions,

$$U_{ion}^{intra} = \sum_i \left(\overline{E}_i q_i + \frac{1}{2} J_i q_i^2 \right), \tag{2.51}$$

where

$$\overline{E}_i = \frac{\sum_\alpha E_{i\alpha}^{(0)} \Delta q_{i\alpha}}{q_i} \tag{2.52}$$

and J_i is the species dependent atomic on-site Coulomb integral. The first term of Eq. (2.51) is directly related to the electronegativity of atoms. This term lowers the energy of the system and drives charge transfer between atoms. The second term of Eq. (2.51) increases the energy of the system and thereby counteracts charge transfer between atoms. Note that the second term in Eq. (2.48) for the promotion energy and the first term in Eq. (2.51) for the ion formation energy cancel when the promotion and the ion formation energies are added together.

U_{ion}^{inter} is the electrostatic energy which is responsible for the anions and cations attracting each other due to their opposing charges in an ionic solid and is defined as,

$$U_{ion}^{inter} = \frac{1}{2} \sum_{i,j:i<j} J_{ij} q_i q_j. \tag{2.53}$$

Figure 2.14 shows the Coulomb integrals of the elemental and binary interactions and the standard Coulomb interaction as a function of interatomic distance R. The Coulomb integrals J_{ij} are determined by the species dependent atomic τ_i terms. For

heteronuclear interactions with $\tau_i \neq \tau_j$ [34],

$$J_{ij}(R) = \frac{k_c}{R} - \left[e^{-\frac{\tau_i R}{k_c}} \left(\frac{(\tau_j)^4 \tau_i}{2((\tau_i)^2-(\tau_j)^2)^2} - \frac{\left((\tau_j)^6 - 3(\tau_j)^4(\tau_i)^2\right)k_c}{((\tau_i)^2-(\tau_j)^2)^3 R} \right) + e^{-\frac{\tau_j R}{k_c}} \left(\frac{(\tau_i)^4 \tau_j}{2((\tau_j)^2-(\tau_i)^2)^2} - \frac{\left((\tau_i)^6 - 3(\tau_i)^4(\tau_j)^2\right)k_c}{((\tau_j)^2-(\tau_i)^2)^3 R} \right) \right] \tag{2.54}$$

while for homo nuclear interactions with $\tau_i = \tau_j$ [171],

$$J_{ij}(R) = \frac{k_c}{R} - \left[e^{-\frac{\tau_i R}{k_c}} \left(\frac{k_c}{R} + \frac{11}{16}\tau_i + \frac{3}{16}(\tau_i)^2 \frac{R}{k_c} + \frac{1}{48}(\tau_i)^3 \left(\frac{R}{k_c}\right)^2 \right) \right] \tag{2.55}$$

where $\tau_i = \frac{16}{5} J_i$ and k_c is the Coulomb constant.

To avoid the computationally expensive Ewald summation, the Coulomb integrals are screened and truncated using a polynomial of order 7 [132],

$$T(R) = a_0 + a_1 R + a_2 R^2 + a_3 R^3 + a_4 R^4 + a_5 R^5 + a_6 R^6 + a_7 R^7, \tag{2.56}$$

with

$$\begin{aligned}
a_0 &= \frac{-35R_{T1}^3R_{T2}^4 + 21R_{T1}^2R_{T2}^5 + 7R_{T1}R_{T2}^6 + R_{T2}^7}{(R_{T2}-R_{T1})^7}, \\
a_1 &= \frac{140R_{T1}^3R_{T2}^3}{(R_{T2}-R_{T1})^7}, \\
a_2 &= \frac{-210(R_{T1}^3R_{T2}^2 + R_{T1}^2R_{T2}^3)}{(R_{T2}-R_{T1})^7}, \\
a_3 &= \frac{140(R_{T1}^3R_{T2} + 3R_{T1}^2R_{T2}^2 + R_{T1}R_{T2}^3)}{(R_{T2}-R_{T1})^7}, \\
a_4 &= \frac{-35(R_{T1}^3 + 9R_{T1}^2R_{T2} + R_{T2}^3)}{(R_{T2}-R_{T1})^7}, \\
a_5 &= \frac{84(R_{T1}^2 + 3R_{T1}R_{T2} + R_{T2}^2)}{(R_{T2}-R_{T1})^7}, \\
a_6 &= \frac{-70(R_{T1} + R_{T2})}{(R_{T2}-R_{T1})^7}, \\
a_7 &= \frac{20}{(R_{T2}-R_{T1})^7},
\end{aligned}$$

with a range of the function defined from $R_{T1} = 0$ Å to $R_{T2} = 10$ Å (see Figure 2.14). We also tested a range of the function defined from 0 to 30 Å, given in grey in Fig. 2.14, which resulted in the same charge transfer between the atoms.

In addition to charge transfer, magnetic and van der Waals energies can be included in the binding energy expression (Eq. (2.29)) depending on their importance to the system [27, 28, 172].

2.4.2 From TB to reduced TB

By choosing the z-axis along the direction of the bond from atom i to atom j the ij bond energy in Eq. (2.32) separates into individual σ and π contributions, namely

$$U_{bond,ij} = U_{bond,ij}^{\sigma} + U_{bond,ij}^{\pi}, \tag{2.57}$$

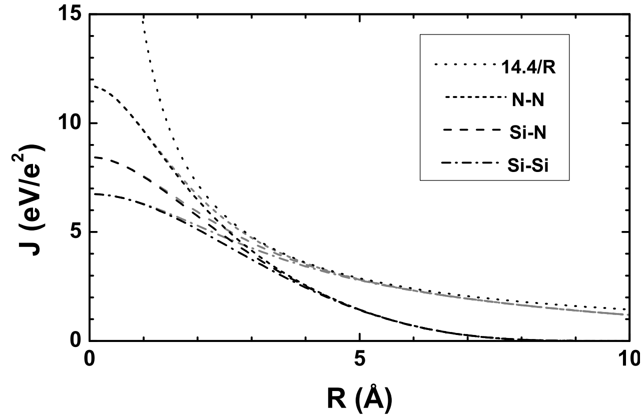

Figure 2.14: Screened Coulomb integrals [132] J as a function of interatomic distance R for the elemental silicon-silicon (Si-Si) and nitrogen-nitrogen (N-N) and binary silicon-nitrogen (Si-N) interactions (black: range of function from 0 to 10 Å, grey: range of function from 0 to 30 Å) compared to the unscreened Coulomb interaction.

with

$$U^{\sigma}_{bond,ij} = 2\left(ss\sigma_{ij}\Theta_{jsis} + sp\sigma_{ij}\Theta_{jzis} + ps\sigma_{ij}\Theta_{jsiz} + pp\sigma_{ij}\Theta_{jziz}\right), \tag{2.58}$$

and

$$U^{\pi}_{bond,ij} = 2pp\pi_{ij}\left(\Theta_{jxix} + \Theta_{jyiy}\right). \tag{2.59}$$

Thus, whereas the π bond energy can be written as a single contribution $2\beta_{\pi ij}\Theta^{tot}_{\pi ji}$, the σ bond energy comprises four different contributions as in Eq. (2.58) so that the powerful valence bond concept of a single σ bond order is lost.

For a binary *sp*-valent system the reduced TB approximation [173, 174] reduces the *four* independent TB σ bond integrals $ss\sigma_{ij}$, $sp\sigma_{ij}$, $ps\sigma_{ij}$, and $pp\sigma_{ij}$ to *three* independent parameters, namely $\beta_{\sigma ij}$, $p_{\sigma ij}$, and $p_{\sigma ji}$ by assuming that the four TB

σ bond integrals satisfy the constraint equation

$$sp\sigma_{ij} ps\sigma_{ij} = ss\sigma_{ij} pp\sigma_{ij}. \tag{2.60}$$

For the case of homovalent bonds the constraint equation implies that the $sp\sigma_{ij}$ bond integral is given by the physically intuitive geometric mean of $ss\sigma_{ij}$ and $pp\sigma_{ij}$, namely

$$sp\sigma_{ij} = \sqrt{|ss\sigma_{ij}|\, pp\sigma_{ij}}, \tag{2.61}$$

noting that $ss\sigma_{ij} < 0$, $pp\sigma_{ij} > 0$, $sp\sigma_{ij} > 0$, and $ps\sigma_{ij} < 0$.

Expressions for the two reduced TB parameters $p_{\sigma ij}$ and $p_{\sigma ji}$ may be obtained by making a transformation from the atomic orbitals to *bonding* hybrids that point into the ij bond

$$|i\sigma\rangle = \sqrt{1 - p_{\sigma ij}}\, |is\rangle + \sqrt{p_{\sigma ij}}\, |iz\rangle\,, \tag{2.62}$$

$$|j\sigma\rangle = \sqrt{1 - p_{\sigma ji}}\, |js\rangle - \sqrt{p_{\sigma ji}}\, |jz\rangle\,, \tag{2.63}$$

and *non-bonding* hybrids that point away from the ij bond

$$|i\sigma^*\rangle = \sqrt{p_{\sigma ij}}\, |is\rangle - \sqrt{1 - p_{\sigma ij}}\, |iz\rangle\,, \tag{2.64}$$

$$|j\sigma^*\rangle = \sqrt{p_{\sigma ji}}\, |js\rangle + \sqrt{1 - p_{\sigma ji}}\, |jz\rangle\,. \tag{2.65}$$

The hybridisation character on atom i clearly depends on its neighbouring atoms j (and vice versa) and we will show later that for a binary system $p_{\sigma ij} \neq p_{\sigma ji}$

(see Eq. (2.74)). We should note that the parameter p_σ, which gives the amount of p-character in the bonding hybrids, has been defined to vary from 0 to 1 [27] in contrast to the original parameter p_σ^{orig} that varied from 0 to ∞ [173, 174] as $p_\sigma^{orig} = p_\sigma / (1 - p_\sigma)$.

The values of $p_{\sigma ij}$ and $p_{\sigma ji}$ are now determined [173, 174] by requiring that the ij *inter-site* Hamiltonian with respect to the above i and j hybrids takes the diagonal form

$$H_{\sigma ij} = \begin{pmatrix} \beta_{\sigma ij} & 0 \\ 0 & 0 \end{pmatrix} \tag{2.66}$$

where

$$\beta_{\sigma ij} = \langle i\sigma | H | j\sigma \rangle . \tag{2.67}$$

The diagonal *non-bonding* matrix element $\langle i\sigma^* | H | j\sigma^* \rangle$ with the *non-bonding* hybrids given by Eqs. (2.64) and (2.65) can then be made to vanish by choosing $p_{\sigma ij}$ and $p_{\sigma ji}$ to satisfy

$$\sqrt{p_{\sigma ij} / (1 - p_{\sigma ij})} = pp\sigma_{ij} / sp\sigma_{ij} \tag{2.68}$$

and

$$\sqrt{p_{\sigma ji} / (1 - p_{\sigma ji})} = pp\sigma_{ji} / sp\sigma_{ji} = pp\sigma_{ij} / |ps\sigma_{ij}| , \tag{2.69}$$

since $pp\sigma_{ji} = pp\sigma_{ij}$ and $sp\sigma_{ji} = |ps\sigma_{ij}|$. Further, these values also lead to the off-diagonal matrix elements in Eq. (2.66) vanishing. Substituting $sp\sigma_{ij}$ and $|ps\sigma_{ij}|$ from Eqs. (2.68) and (2.69) respectively into the constraint Eq. (2.60) immediately

gives the relation that

$$pp\sigma_{ij} = \sqrt{p_{\sigma ij} p_{\sigma ji} / \left[\left(1 - p_{\sigma ij}\right) \left(1 - p_{\sigma ji}\right) \right]} \left| ss\sigma_{ij} \right| . \tag{2.70}$$

The reduced TB parameter $\beta_{\sigma ij}$ may now be found by substituting Eqs. (2.62) and (2.63) in Eq. (2.67) and using Eqs. (2.68) and (2.69) and is given by

$$\beta_{\sigma ij} = \left[1 / \sqrt{(1 - p_{\sigma ij})(1 - p_{\sigma ji})} \right] ss\sigma_{ij}. \tag{2.71}$$

Finally, using Eqs. (2.68) - (2.71), the original four independent TB bond integrals can be expressed in terms of the three reduced TB parameters as

$$\left. \begin{array}{c} ss\sigma_{ij} \\ sp\sigma_{ij} \\ ps\sigma_{ij} \\ pp\sigma_{ij} \end{array} \right\} = \left. \begin{array}{c} \sqrt{\left(1 - p_{\sigma ij}\right) \left(1 - p_{\sigma ji}\right)} \\ -\sqrt{\left(1 - p_{\sigma ij}\right) p_{\sigma ji}} \\ \sqrt{p_{\sigma ij} \left(1 - p_{\sigma ji}\right)} \\ -\sqrt{p_{\sigma ij} p_{\sigma ji}} \end{array} \right\} \beta_{\sigma ij}. \tag{2.72}$$

Interestingly, we see that squaring both sides and adding leads to the very simple expression for $\beta_{\sigma ij}$, namely

$$\beta_{\sigma ij} = -\sqrt{\left(ss\sigma_{ij}\right)^2 + \left(sp\sigma_{ij}\right)^2 + \left(ps\sigma_{ij}\right)^2 + \left(pp\sigma_{ij}\right)^2}, \tag{2.73}$$

which, unlike Eq. (2.71), weights all four TB bond integrals equally. In addition, this definition of $\beta_{\sigma ij}$ automatically guarantees that the second moment of the density of states is preserved in going from TB to reduced TB, even though the constraint Eq. (2.60) might not be accurately satisfied. Tests for silicon, nitrogen, and silicon nitride have shown that this parameterisation reproduces the total width of the

density of states. However, we will see later that the reproduction of the valence band width of the density of states depends on how well the bond integrals for each individual system can be approximated by reduced TB.

In this thesis, therefore, all *three* reduced TB parameters will be defined in terms of the *four* TB bond integrals as for $\beta_{\sigma ij}$ in Eq. (2.73) above. It follows from Eqs. (2.68) and (2.69) and the constraint Eq. (2.60) that

$$p_{\sigma ij} = \frac{1}{2}\left\{1/\left[1+(sp\sigma_{ij}/pp\sigma_{ij})^2\right] + 1/\left[1+(ss\sigma_{ij}/ps\sigma_{ij})^2\right]\right\}, \qquad (2.74)$$

and similarly for $p_{\sigma ji}$. Equations (2.73) and (2.74) were obtained in discussions with David Pettifor and Paul Kamenski after the author of this thesis suggested to weight all four σ TB bond integrals equally in the description of the reduced TB parameters.

For elemental interactions, where $sp\sigma_{ij} = sp\sigma_{ji}$ and $ps\sigma_{ij} = ps\sigma_{ji}$, $p_{\sigma ij}$ and $p_{\sigma ji}$ are identical. However, for binary interactions, where $sp\sigma_{ij} \neq sp\sigma_{ji}$ and $ps\sigma_{ij} \neq ps\sigma_{ji}$, $p_{\sigma ij}$ and $p_{\sigma ji}$ give different results. Therefore, considering a binary *sp*-valent system that comprises two chemical species, e.g. Si and N which will be indexed by μ and ν respectively, and taking account of Eq. (2.73), we can determine in total the following reduced TB parameters that contribute to the σ bonds in the system: $\beta_{\sigma ij}^{\mathrm{Si\,Si}}$, $\beta_{\sigma ij}^{\mathrm{Si\,N}}$, $\beta_{\sigma ij}^{\mathrm{N\,N}}$, $p_{\sigma ij}^{\mathrm{Si\,Si}}$, $p_{\sigma ij}^{\mathrm{Si\,N}}$, $p_{\sigma ij}^{\mathrm{N\,Si}}$, and $p_{\sigma ij}^{\mathrm{N\,N}}$.

Although $p_{\sigma ij}$ depends on both the nature of the μ and ν species of atoms i and j through Eq. (2.74), the dominance of the μ atom i over the ν atom j can be demonstrated [174] by making the geometric mean approximation that

$$\langle i\mu\alpha \,| H_\sigma |\, j\nu\beta\rangle \approx \sqrt{\langle i\mu\alpha \,| H_\sigma |\, j\mu\alpha\rangle \,\langle i\nu\beta \,| H_\sigma |\, j\nu\beta\rangle}. \qquad (2.75)$$

This results in

$$\left(\frac{sp\sigma_{ij}^{\mu\nu}}{pp\sigma_{ij}^{\mu\nu}}\right)^2 \approx \frac{\left|ss\sigma_{ij}^{\mu\mu}\right| pp\sigma_{ij}^{\nu\nu}}{pp\sigma_{ij}^{\mu\mu} pp\sigma_{ij}^{\nu\nu}} = \frac{\left|ss\sigma_{ij}^{\mu\mu}\right|}{pp\sigma_{ij}^{\mu\mu}}, \tag{2.76}$$

and

$$\left(\frac{ss\sigma_{ij}^{\mu\nu}}{ps\sigma_{ij}^{\mu\nu}}\right)^2 \approx \frac{\left|ss\sigma_{ij}^{\mu\mu}\right| \left|ss\sigma_{ij}^{\nu\nu}\right|}{pp\sigma_{ij}^{\mu\mu} \left|ss\sigma_{ij}^{\nu\nu}\right|} = \frac{\left|ss\sigma_{ij}^{\mu\mu}\right|}{pp\sigma_{ij}^{\mu\mu}}. \tag{2.77}$$

Therefore, using Eq. (2.61),

$$p_{\sigma ij}^{\mu\nu} \approx \frac{pp\sigma_{ij}^{\mu\mu}}{\left|ss\sigma_{ij}^{\mu\mu}\right| + pp\sigma_{ij}^{\mu\mu}} = p_{\sigma ij}^{\mu\mu}. \tag{2.78}$$

Similarly,

$$p_{\sigma ij}^{\nu\mu} \approx \frac{pp\sigma_{ij}^{\nu\nu}}{\left|ss\sigma_{ij}^{\nu\nu}\right| + pp\sigma_{ij}^{\nu\nu}} = p_{\sigma ij}^{\nu\nu}. \tag{2.79}$$

We will see later (compare Figures. 3.2, 4.2, and 5.2) that this is an approximation that is confirmed by our data. Put differently, for example, the hybridisation character on each silicon atom is very similar in the elemental ground state diamond structure and the binary ground state β structures.

A different simplification to Eq. (2.74) would be if all the TB bond integrals displayed the same distance dependence, so that the *ratio* of any two bond integrals became distance invariant, thereby leading to constant values of $p_{\sigma ij}$. We will see in Chapters 3, 4, and 5 that our data for silicon, nitrogen, and silicon nitride suggests that $p_{\sigma ij}$ is rather structure than distance dependent.

The distance dependence of the reduced TB parameters $\beta_{\sigma ij}$ and $\beta_{\pi ij}$ are given

by GSP functions with $n_a = n_b$ that we cut off as described in Subsection 2.4.1. The first nearest-neighbour distance dependence of the reduced TB parameters $p_{\sigma ij}$ will be shown to be well fitted by the exponential function

$$p_\sigma = 1/\left[1 + c \cdot \exp\left(-\gamma R\right)\right]. \tag{2.80}$$

This functional form is also able to describe the distance invariant behaviour of $p_{\sigma ij}$ as discussed above for a given structure by setting γ to zero.

2.4.3 From reduced TB to BOP

The binding energy expression for analytic BOPs is the same as for TB in Eq. (2.29). As mentioned before, due to the reduced TB approximation it is possible to write the bond energy in terms of a single σ contribution, namely,

$$U_{bond,ij} = 2\beta_{\sigma ij}\Theta_{\sigma ji} + 2\beta_{\pi ij}\left(\Theta_{\pi_+ ji} + \Theta_{\pi_- ji}\right). \tag{2.81}$$

The factor two is included since only half of the bond energy contributions are included in Eq. (2.31). The pairwise parameters $\beta_{\sigma ij}$ and $\beta_{\pi ij}$ can be taken directly from reduced TB. The σ and π bond order contributions that determine the effect of the local bond environment on the ij bond strength are being evaluated through a many atom series expansion as described in Subsection 2.3.3.

The promotion energy on site i can be written as [174]

$$U_{prom,i} = \delta_i \left(1 - 1/\sqrt{1 + \frac{16}{\Theta_{tot,i}\left(1 + p_{\sigma i}\right)\left(27 - 3\sqrt{3p_{\sigma i}}\right)^2 \hat{\delta}_i^2}}\right) \tag{2.82}$$

where δ_i and $\hat{\delta}_i$ are the on-site level splitting and the normalised on-site level

splitting, respectively, as previously described for Eq. (2.23), and

$$\Theta_{tot,i} = \sum_{j,j\neq i} \left(\Theta_{\sigma ji} + \Theta_{\pi_+ ji} + \Theta_{\pi_- ji}\right). \tag{2.83}$$

Furthermore, considering Eqs. (2.78) and (2.79) we can write

$$p_{\sigma i} \approx p_{\sigma ij}, \tag{2.84}$$

which means that the *inter-site* reduced TB parameter, when assumed to be environment independent, can be approximated by an *on-site* BOP parameter.

The repulsive energy we employed for the bond-based BOP model was the same as for the reduced TB models.

2.4.4 Computational details

The computational details that we will use in the next four Chapters to derive reduced TB and BOP parameters for elemental silicon and nitrogen and binary silicon nitride systems are as follows.

The DFT reference binding energies are calculated with the VASP code [175, 176] using the local density approximation (LDA) [177, 178] to the exchange-correlation energy functional and the projector augmented-wave method (PAW) [179, 180]. For each calculation, a sufficiently large plane wave cutoff energy and a dense Monkhorst-Pack [181, 182] type k-point mesh ensure numerical convergence for formation energy differences to within 5 meV/atom. We carry out the TB calculations using the Bond-Order Potential from Oxford (BOPfox [183]) package, which solves the tight-binding secular equation in k-space and calculates the local DOS using the tetrahedron k-space technique with Blöchl corrections [184].

The TB and BOP parameters are obtained as follows. For both, bond integral and repulsive functions, we choose the values for the parameters R_0, R_c, R_{tail}, and R_{cut} as follows. R_0 is set to the respective ground state equilibrium nearest neighbour distance (silicon diamond, nitrogen dimer, and silicon nitride β). R_c is set equidistantly between respective equilibrium first and second nearest neighbour distances. For nitrogen, R_c is set to half the value of the first and second nearest neighbour distances in the diamond structure. R_{tail} is set to the fcc equilibrium first nearest neighbour distance for the silicon and nitrogen models and to the B2 equilibrium first nearest neighbour distance for silicon nitride. R_{cut}, which defines the range of the model, is set to where the projected bond integral data is small. $\Delta U_{atom,i}$ in Eq. (2.46) is chosen to be the magnitude of the free atom magnetic energy calculated with DFT. The parameters related to the bond integrals, β_0, n_a, and n_c in Eqs. (2.38) and (2.45), are fitted to DFT projected orthogonal TB bond integrals of equilibrium structures. The parameters related to the repulsive function in Eqs. (2.38) and (2.43), Φ_0, n_a, n_b, and n_c, are pairwise fitting parameters, and $n_{d,i}$ in Eq. (2.42) is an atomic fitting parameter. These repulsive parameters are varied to reproduce the DFT reference binding energies. Φ_0, n_a for bond integrals, n_b, and n_c are let to vary freely but are constrained to be positive to give smoothly decaying GSP functions. β_0 is treated similarly, but constrained to be negative. n_a of the repulsive function and n_d are used to affect stabilization over different nearest neighbour distances and coordination numbers, respectively. The fitting parameters related to the repulsive function Φ_0, n_b, and n_c are varied by minimising the least squares error between DFT and TB as well as DFT and BOP binding energies employing a downhill simplex method. The Python fitting program employed was developed in the group with major contributions from Benoit Mangili and Paul

Kamenski. The Yukawa-type core repulsion (Eq. (2.44)) is adjusted such that the silicon and silicon nitride dimers predict smooth binding energy curves.

Throughout the development process we were confronted with a trade off between the potential functions flexibility, accuracy, and transferability. Generally we have found that the more parameters we can fix to physically meaningful values, the better the overall quality of the models. For example, fixing ΔU_{atom} to the respective free atom magnetic energies, rather than treating it as a degree of freedom, improved the quality of the individual models. Furthermore, influencing the effect of the model on coordination numbers through n_d or on nearest neighbour distances through n_a both improved the manageability of the development process.

2.5 Summary

The silicon nitride system is of great interest since it is widely applied as an electronic and structural material in industry. Experimental studies on the deposition of silicon nitride films via different CVD and PVD processes have been conducted for considerable time, however the growth mechanisms of silicon nitride do not seem to be sufficiently understood.

For modelling film deposition the description of clusters, bulk structures, point defects, surface reconstructions, and melting temperatures is important. All currently employed potentials for silicon nitride seem to lack realistic descriptions of the growth processes. Therefore, an accurate and transferable model suitable for simulating growth of silicon nitride does not exist in the literature. For instance, the application of a Tersoff potential to silicon nitride for modelling film growth did not give a proper description of the surface. A high number of nitrogen dangling bonds was observed, the nitrogen bonding environments differed from the experimentally

observed structures, and the surface was enriched with nitrogen atoms. Further, no results of using the Vashishta potential to describe local atomic environments, microstructural features, surface reconstructions, or bulk properties resulting from deposition can be found in the literature. Moreover, the Reactive Force Field (ReaxFF) parameterisation for silicon nitride is not transferable to molecular systems involving double or triple bonded nitrogen and torsional terms because these are not included. Therefore, it is understandable that no successful application of the silicon nitride ReaxFF parameterisation to modelling surface reconstructions or film deposition can be found in the literature.

First attempts of using bond-based bond-order potentials (BOPs) to model film growth of covalent systems have been successful and descriptions of clusters, bulk structures, point defects, surface reconstructions, and melting temperatures are in better agreement with experiments than results from other currently employed potentials. In particular, the effects of growth temperature on the crystallinity of silicon and gallium arsenide films and the effect of vapour flux ratio on the crystallinity and defect population of gallium arsenide films could be correctly described.

In this Chapter we presented the methodology for deriving transferable reduced TB models directly from DFT. In Chapters 3 to 5 we will apply this methodology to elemental silicon, nitrogen, and to the binary silicon nitride. In Chapter 6 we will develop a bond-based BOP for silicon.

3 Reduced TB Model for Silicon

In the previous Chapter we described the general methodology for the development of reduced TB models. In this Chapter we will present the details of the reduced TB model for silicon. First, we show the two-centre TB bond integrals obtained from DFT via the projection scheme and the reduced TB parameters calculated from this data. In addition, we tabulate the parameters for the reduced TB bond integrals and provide details of the electronic structure of the silicon diamond structure. Further, we tabulate the parameters for the repulsive energy contribution and provide the resulting binding energy curves. In addition, we give details of tests of the reduced TB model including equilibrium binding energy, volume, bulk modulus, elastic constants, and point defect energies.

3.1 Bond Integrals

The two-centre orthogonal TB bond integrals obtained from DFT via the projection scheme described in Subsection 2.4.1 for different structures of silicon are shown in Figure 3.1. In this figure and in the following, the data for equilibrium structures is displayed with enlarged symbols. As one can see from the figure, the data is distance and structure dependent. In addition, screening of the bond integrals in the second nearest neighbours data can be observed. This screening is especially visible for the

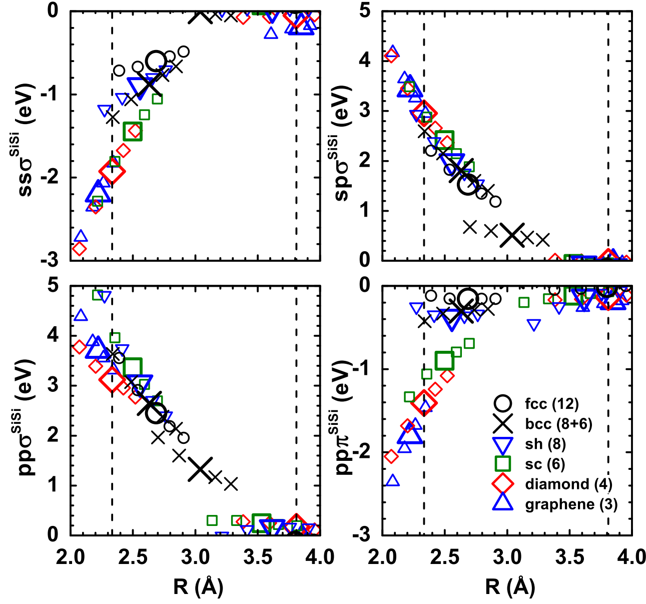

Figure 3.1: Two-centre orthogonal TB Si-Si bond integrals obtained from DFT via projection scheme for different structures as a function of interatomic distance R. Equilibrium data are displayed with enlarged symbols. Dashed vertical lines are the first and second nearest neighbour distances in the ground state equilibrium diamond structure, $R_1^{\diamond}$ and $R_2^{\diamond}$.

bcc structure, and can be attributed to the fact that the bonding between a pair of second nearest neighbour atoms is weakened by the first nearest neighbour atoms surrounding the bond [185].

Figure 3.2 shows the reduced TB Si-Si parameters β_σ, β_π, and p_σ that are calculated from the data in Figure 3.1 through Eqs. (2.73) and (2.74). Similar to the data in Figure 3.1, the data for the reduced TB parameters β_σ, β_π, and p_σ is distance and structure dependent. The data for β_π falls off to zero at shorter values for R than the data for β_σ. This can be attributed to the relatively short range of π bonds compared to σ bonds.

The functions $\beta_\sigma(R)$, $\beta_\pi(R)$, and $p_\sigma(R)$ in Figure 3.2 are fitted to equilibrium

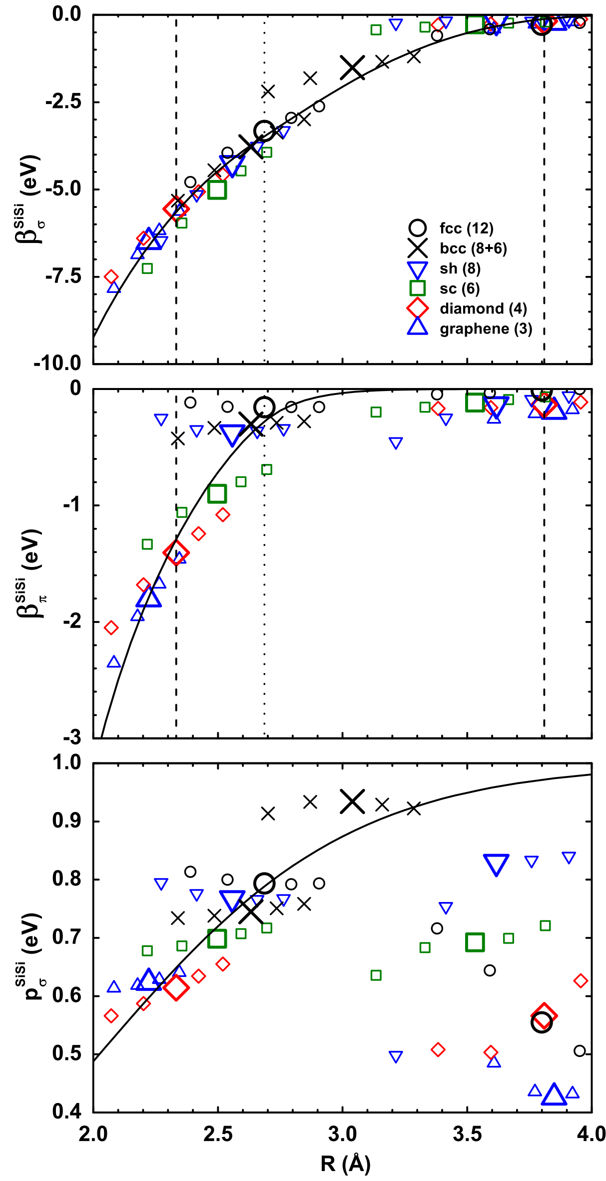

Figure 3.2: Reduced TB Si-Si parameters calculated from projected bond integrals in Figure 3.1 for different structures as a function of interatomic distance R. Equilibrium data are displayed with enlarged symbols. Dashed vertical lines are the first and second nearest neighbour distances in the ground state equilibrium diamond structure, $R_1^\diamond$ and $R_2^\diamond$. The vertical dotted line marks R_{tail}.

data points and cut off smoothly as described in Subsection 2.4.4. The cutoff is typically between first and second nearest neighbours of the ground state structure. In cases of steep slopes such as $\beta_\pi(R_{tail})$ in Figure 3.2 a polynomial cutoff function of degree three may lead to sign changes, and hence to a non-smooth decay of the reduced TB parameters. However, since the oscillations in the cutoff region are very sensitive to the environment and we aim for transferable parameters, a smooth distance dependence of the reduced TB parameters is essential. The cutoff function we chose is given in Eq. (2.39). This function substitutes the original function over a range where the original function is not fitted, and, in contrast to using a polynomial as in Xu's carbon model [169] and Kwon's silicon model [170], never changes sign.

Generally, we aim to approximate each data set with a single function. In Figure 3.2 the data for β_σ is relatively structure independent unlike the individual $ss\sigma$ and $pp\sigma$ curves in Figure 3.1 and the data is well reproduced by a single function. In addition, the function $\beta_\sigma(R)$ reproduces the distant-dependent gradients of all structures well. One exception is the screened data of the second nearest neighbours of the bcc structure, which is equivalent to the screening effect inherent in the projected data in Figure 3.1. Even though the data for β_π is more structure dependent, the gradients of the individual structures are still fairly well reproduced by a single function. The most pronounced structure dependence can be seen in the p_σ data where the non-equilibrium data and the gradients of the different structures are less well reproduced by a single function. Hence, a fit to the p_σ equilibrium data, as shown in Figure 3.2, might not be the best solution as we will find in Section 3.2. The gradients at the equilibrium first nearest neighbour distance in each structure of silicon are shown in Figure 3.3.

The parameters of the functions representing the reduced TB parameters for the

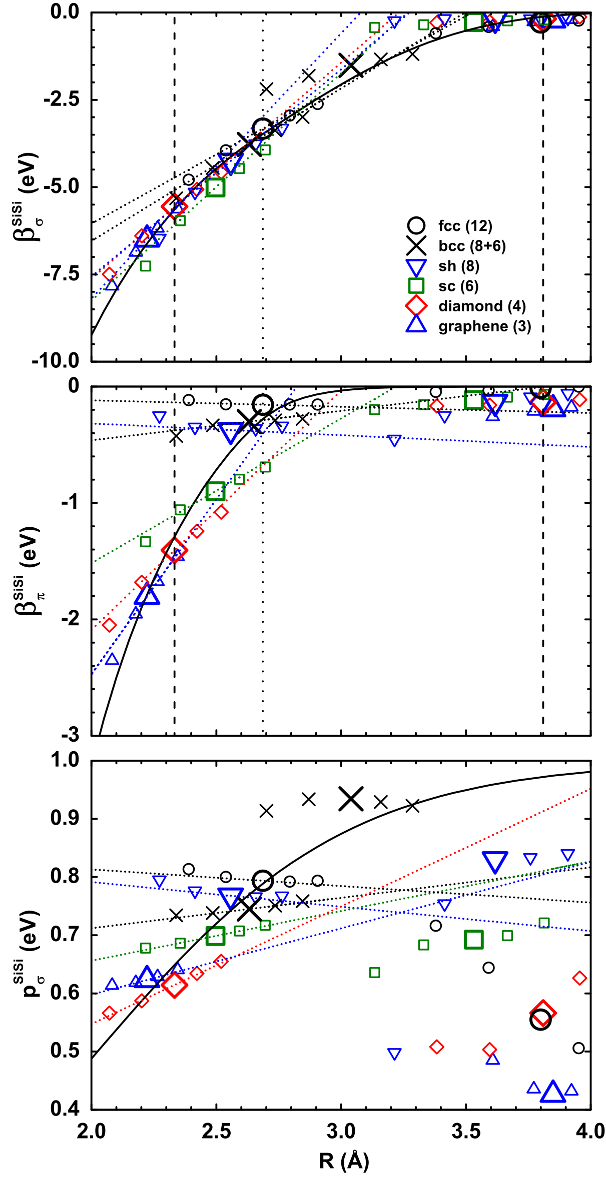

Figure 3.3: Reduced TB Si-Si parameters from Figure 3.2 including the gradients at the equilibrium first nearest neighbour distance in each structure of silicon.

Table 3.1: Reduced TB parameters for silicon-silicon (Si-Si), nitrogen-nitrogen (N-N), and silicon-nitrogen (Si-N) interactions.

	Si-Si	N-N	Si-N (N-Si)
$\beta_{0,\sigma}$ (eV)	-5.643	-21.640	-10.183
$\beta_{0,\pi}$ (eV)	-1.290	-5.015	-2.347
R_0 (Å)	2.333	1.103	1.671
R_c (Å)	3.071	2.335	2.212
$n_{a,\sigma}$	1.840	1.551	0.792
$n_{a,\pi}$	4.915	2.339	1.712
$n_{c,\sigma}$	1.080	2.937	5.005
$n_{c,\pi}$	11.552	5.382	9.009
R_{tail} (Å)	2.687	2.170	2.205
R_{cut} (Å)	4.200	2.750	3.500
c	0.333	0.976	0.588 (1.315)
γ (1/Å)	0.000	0.000	0.000 (0.000)

Table 3.2: On-site levels for silicon (Si) and nitrogen (N) (Ref. [186]).

	Si	N
E_p (eV)	-7.59	-13.84
E_s (eV)	-14.79	-26.22

silicon TB model are given in Table 3.1. In addition to the bond integrals, on-site levels are required for the reduced TB model. In this study we employ the on-site levels from Harrison [186] which are given in Table 3.2. The Harrison on-site levels were chosen for all reduced TB models in this thesis to guarantee the transferability of the silicon model between different environments, for example between silicon nitride and silicon carbide [164].

Figure 3.4 shows the density of states for the silicon ground state diamond structure calculated with DFT, projected TB, and reduced TB. For ease of comparison, all density of states are shifted along the energy scale such that the Fermi energy is at zero eV. The features of the DFT DOS are qualitatively reproduced by projected

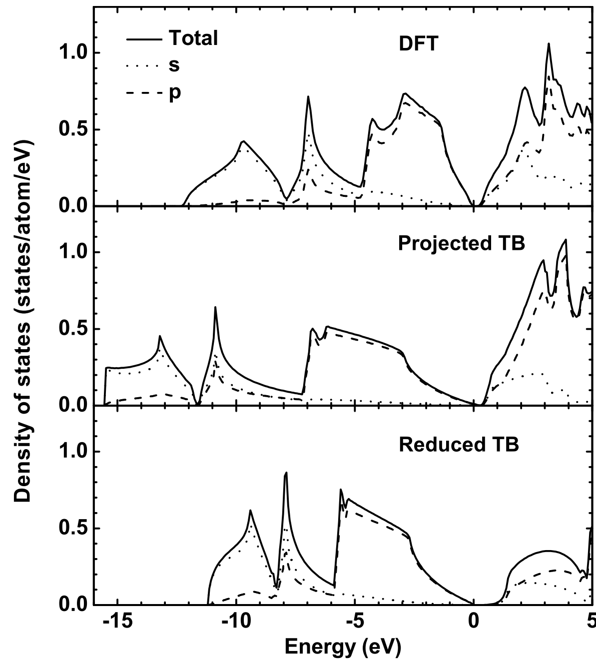

Figure 3.4: s and p contributions to the average total density of states of the silicon diamond structure for DFT, projected TB, and reduced TB. For the calculation of the projected TB DOS the same on-site levels were used as for the calculation of the reduced TB DOS.

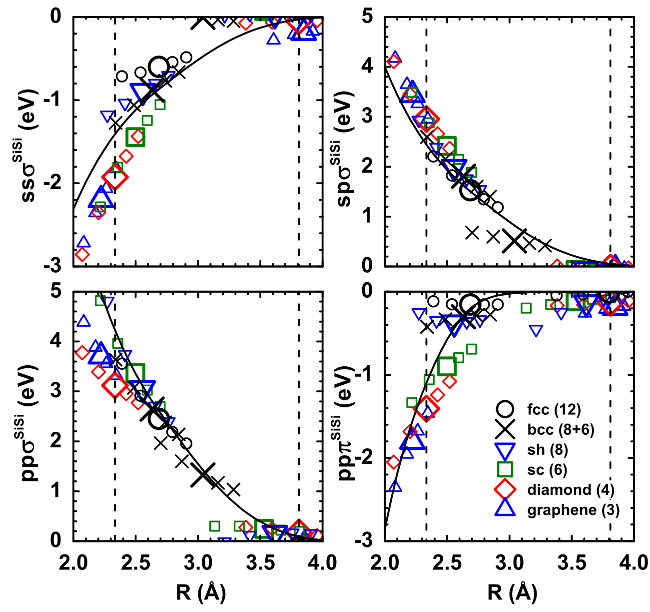

Figure 3.5: Two-centre orthogonal TB Si-Si bond integrals from Figure 3.1 including the functions that show how well the bond integrals are approximated by reduced TB.

TB and reduced TB. Further, the individual s and p contributions of the projected TB and reduced TB models reproduce the distinct sp-hybridisation. The valence band width, when going from DFT to projected TB, is only poorly reproduced because for the projected TB DOS Harrison's [186] on-site levels were used instead of the output values from the projection scheme described in Subsection 2.4.1. This was merely done to increase the comparability between the projected TB DOS and the reduced TB DOS. The fact that the features of the DOS are only qualitatively reproduced by going from projected TB to reduced TB can be attributed to the underlying theory. At this stage our new parameterisation guarantees through Eq. (2.73) that the total band width is conserved when going from projected TB to reduced TB, however, how well the valence band width is reproduced depends on how well reduced TB approximates the individual bond integrals for each system. Figure 3.5 displays the two-centre orthogonal TB Si-Si bond integrals from Figure 3.1 including the functions that show how well the bond integrals are approximated by reduced TB. One can see that at the nearest neighbour distance in the ground state equilibrium diamond structure reduced TB underestimates the magnitude of the $ss\sigma$, $sp\sigma$, and $pp\pi$ bond integrals, while it overestimates the magnitude of the $pp\sigma$ bond integral. A better match could be achieved by introducing degrees of freedom into Eqs. (2.72).

Figure 3.6 displays the silicon σ and π bond orders for a first nearest neighbour bond with respect to interatomic distance in the graphene, diamond, simple cubic (sc), and face centred cubic (fcc) structures, which have coordination numbers of 3, 4, 6, and 12, respectively. We see that the graphene structure has a saturated σ bond together with a saturated and an unsaturated π bond corresponding to whether it lies out of or in the plane. The cubic diamond structure has a saturated σ bond

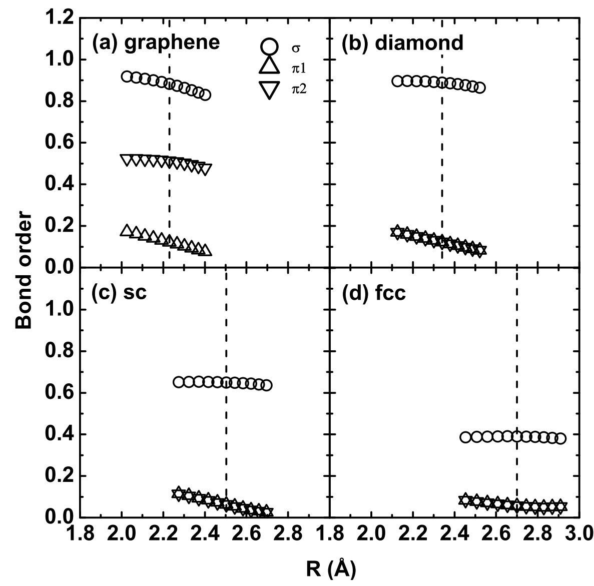

Figure 3.6: σ and π bond orders for a first nearest neighbour bond in the silicon (a) graphene, (b) diamond, (c) simple cubic (sc), and (d) face centred cubic (fcc) structures as a function of interatomic distance R.

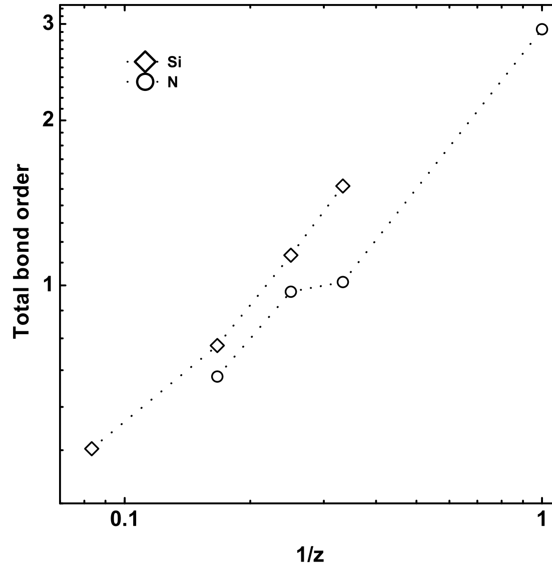

Figure 3.7: Total bond order for a first nearest neighbour bond in the silicon (Si) and nitrogen (N) structures in Figures 3.6 and 4.6, respectively, versus $1/z$, where z is the coordination number.

and two degenerate unsaturated π bonds. Further, the σ bond of the simple cubic structure is less saturated than the σ bond of the diamond structure, and the σ bond of the face centred cubic structure is the least saturated σ bond. Similar to the two π bonds in the diamond structure, the two π bonds in the simple cubic and the face centred cubic structures are perfectly degenerate. Furthermore, the total bond order at equilibrium nearest neighbour distances varies approximately inversely with the coordination number. This can be seen in Figure 3.7 and is in agreement with the chemistry of the investigated structure types [163].

Table 3.3: Repulsive parameters for silicon-silicon (Si-Si), nitrogen-nitrogen (N-N), and silicon-nitrogen (Si-N) interactions.

	Si-Si	N-N	Si-N
Φ_0 (eV)	5.358	18.442	7.242
R_0 (Å)	2.333	1.103	1.671
R_c (Å)	3.071	2.335	2.212
n_a	5.000	3.328	0.010
n_b	2.210	4.017	2.456
n_c	4.170	5.709	2.890
R_{tail} (Å)	2.687	2.170	1.856
R_{cut} (Å)	4.200	2.750	4.200

Table 3.4: Embedding exponent n_d and shift in the non-magnetic DFT free atom reference energy Δu_{atom} for silicon (Si), and nitrogen (N).

	Si	N
n_d	0.800	1.000
Δu_{atom} (eV)	0.611	2.888

3.2 Binding Energy Curves

Having the information for calculating the TB electronic structure, the bond and promotion energies can be computed. However, to calculate total binding energies, a repulsive function (Eq. (2.42)) needs to be determined. Our particular procedure is described in Subsection 2.4.4. Figure 3.8 displays the resulting reduced TB (LCN) binding energy curves for different silicon structures in the right-hand panel. As a comparison, the DFT binding energy curves are shown in the left-hand panel of Figure 3.8. The resultant parameters of the repulsive function for the silicon reduced TB model are given in Table 3.3. The repulsive embedding exponent n_d and the Yukawa parameters are given in Tables 3.4 and 3.5, respectively. The shift in the non-magnetic compared to the magnetic reference energy of the free atom ΔU_{atom} is given in Table 3.4.

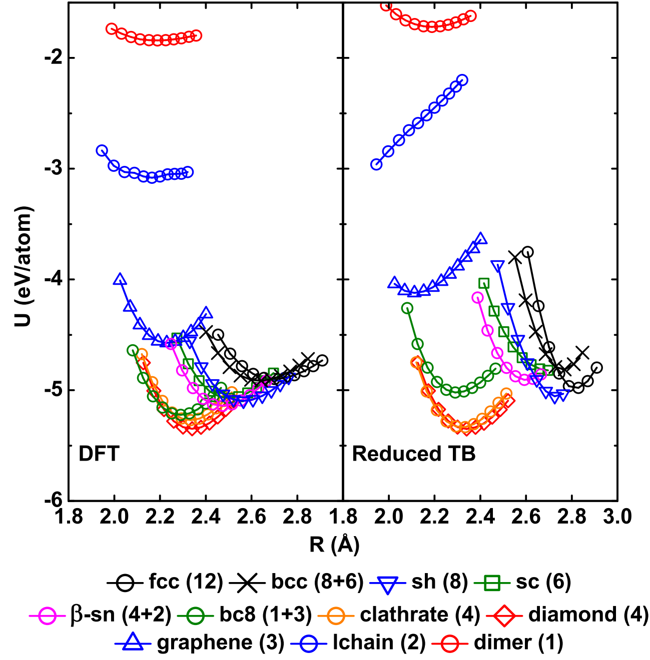

Figure 3.8: DFT and reduced TB (LCN) binding energy curves for different silicon structures as a function of nearest neighbour interatomic distance R. The number of nearest neighbours is given in parenthesis for each structure.

Table 3.5: Yukawa parameters for silicon-silicon (Si-Si) and silicon-nitrogen (Si-N) interactions.

	Si-Si	Si-N
a_c (eV)	185.000	10.444
b_c	4.500	5.794
c_c (1/Å)	0.000	-0.047
$R_{tail,c}$ (Å)	1.560	1.200
$R_{cut,c}$ (Å)	1.916	1.550

3.2.1 DFT binding energy curves

The binding energy curves displayed in Figure 3.8 are calculated with open and close packed structures spanning a wide range of co-ordination. All silicon structures used as a binding energy benchmark together with their equilibrium binding energies are given in Table 3.6. These benchmark structures were used for each trial reduced TB model to compare their equilibrium reduced TB binding energies with their DFT reference binding energies.

The DFT binding energy curves in Figure 3.8 show the diamond structure having the lowest binding energy, as expected. The lowest metastable structure is the clathrate structure. This structure has four nearest neighbours like diamond, but the bond lengths and angles are slightly distorted compared to diamond. The clathrate structure for which the data is given has 34 atoms in its unit cell. In addition, we tested a clathrate structure with 46 atoms per unit cell, which is found to have a slightly higher binding energy than clathrate 34 (DFT: 0.0073 eV/atom, reduced TB: 0.021 eV/atom). The third lowest structure is the bc8 structure. This is a body centred cubic structure with eight atoms in the basis, in which each atom has four nearest neighbours which are divided into one first and three second nearest neighbours. β-Sn is the fourth lowest structure in Figure 3.8. This structure can be viewed as sixfold coordinated, because of a distinct gap between the two second nearest neighbours and the four third nearest neighbours. From the DFT binding energy data the ordering diamond $\rightarrow$ clathrate $\rightarrow$ bc8 $\rightarrow$ β-Sn is observed.

3.2.2 Reduced TB binding energy curves

As shown in Figure 3.3 the function for $p_{\sigma ij}$ does not reproduce the gradients of the reduced TB data very well. This means that choosing a distance dependent

function for p_σ might not be the best choice. Instead we will see that setting $p_{\sigma ij}$ to the equilibrium ground state value provides good fits to the binding energy curves. Therefore, $p_{\sigma ij}$ will be chosen to be a constant by setting the parameter γ in Eq. (2.80) to zero (see Table 3.1). This approach also helps us to destabilize the clathrate structure compared to the diamond structure without changing the bond integrals from having a smooth decaying character.

As one can see from Figure 3.8, the diamond structure is predicted to be the ground state structure by the reduced TB model. Further, the ordering diamond $\rightarrow$ clathrate $\rightarrow$ bc8 $\rightarrow$ β-Sn predicted by the DFT binding energy data is reproduced by the reduced TB model. It has to be noted that DFT predicts this ordering in the presence of all the other structures considered, however, the reduced TB model only predicts the ordering of these structures without considering the close packed structures fcc und sh which are considerably more stable than β-Sn when calculated with the reduced TB model. In addition, the low coordinated structures dimer, linear chain (lchain), and graphene are all fairly well reproduced. Due to the hard core Yukawa potential, the binding energy of the linear chain shows a global minimum well above the diamond structure at shorter interatomic distances. The close packed structures sh, bcc, and fcc are slightly too stable compared to the DFT data. This is not generally an issue with the reduced TB methodology, but rather due to the difficulty of fitting the binding energy curves with transferable TB parameters over such a wide range of co-ordination. The silicon structures used as a binding energy benchmark are given in Table 3.6.

Table 3.7 gives the results of the two approaches with reduced TB with 1) p_σ as a function of interatomic distance R as in Figure 3.2, and 2) reduced TB with $p_\sigma =$ const.. The results from DFT calculations are also included for comparison.

Table 3.6: Silicon structures used as a binding energy benchmark. Equilibrium binding energies (eV/atom) are given in parentheses (reduced TB, DFT). The structures are ordered with respect to DFT binding energies.

dimer (-1.719, -1.841)	lchain (-3.033, -3.069)	achain45 (-3.546, -3.313)
achain (-3.083, -3.315)	zchain90 (-2.780, -3.368)	zchain (-3.347, -3.625)
A14 (-3.755, -4.248)	A17 (-3.734, -4.456)	graphene (-4.122, -4.575)
A9 (-4.122, -4.593)	st12 (-4.123, -4.603)	A8 (-4.338, -4.698)
mp4 (-4.418, -4.778)	st12-W (-4.053, -4.786)	hp7 (-4.327, -4.793)
hp12 (-4.133, -4.795)	hr13 (-4.330, -4.803)	A15 (-4.504, -4.834)
Ab (-4.620, -4.850)	A13 (-4.706, -4.854)	tp30 (-4.603, -4.859)
A11 (-4.794, -4.869)	A12 (-3.371, -4.873)	Ac (-4.316, -4.884)
A10 (-4.601, -4.892)	A7 (-4.426, -4.894)	fcc (-4.989, -4.899)
A6 (-4.960, -4.900)	of8 (-4.747, -4.901)	Gaoc4 (-4.790, -4.908)
C19 (-4.992, -4.909)	hp4 (-4.982, -4.909)	bcc (-4.799, -4.914)
mp16 (-4.442, -4.922)	hcp (-5.036, -4.928)	Gamc4 (-4.778, -4.936)
hr22 (-4.795, -4.937)	Uoc4 (-4.600, -4.942)	Ad (-4.557, -4.944)
A20 (-4.587, -4.945)	Aa (-4.902, -4.951)	ci12 (-3.972, -4.959)
Ai (-4.694, -5.000)	bct5 (-4.773, -5.065)	sc (-4.824, -5.071)
mc4 (-4.841, -5.075)	sh (-5.049, -5.095)	β-Sn (-4.905, -5.140)
bc8 (-5.019, -5.222)	Clathrate46 (-5.310, -5.262)	Clathrate34 (-5.333, -5.269)
hex. dia. (-5.332, -5.338)	diamond (-5.348, -5.348)	–

If we chose approach 1), we can either achieve the correct relative ordering of the different silicon structures or good properties for the ground state diamond structure. This particular model with approach 1) shows comparable equilibrium properties to the approach 2), however, the clathrate34, hcp, and fcc structures are more stable than the diamond structure. In particular the diamond $\rightarrow$ clathrate34 ordering is difficult to achieve with approach 2), as the equilibrium nearest neighbour distances of the diamond and clathrate34 structures are very similar. Furthermore, the ordering bc8 $\rightarrow$ β-Sn is reproduced by the approach 2), however, the ordering is wrong when using approach 1).

The difficulty of achieving the correct relative ordering in addition to satisfactory properties for the ground state diamond structure can be seen by comparing the results from this study with the results by Kamenski [164], who employed approach 1). It can be seen that the ordering diamond $\rightarrow$ clathrate34 was reproduced, however, with a cost of a relatively poor description of the ground state diamond properties. Compare Table 5.2 of Ref. [164] with the last line of Table 3.7. Furthermore, the ordering bc8 $\rightarrow$ β-Sn predicted by DFT was not reproduced in the model by Kamenski.

Table 3.7: Equilibrium properties of different structures for silicon calculated with reduced TB with p_σ as a function of interatomic distance R as in Figure 3.2, reduced TB with p_σ = const., and DFT. Difference to the diamond equilibrium binding energy (ΔU), equilibrium binding energy (U), equilibrium volume (V), and bulk modulus (B) are obtained from Birch-Murnaghan equation of state fits to binding energies. Units are ΔU and U (eV/atom), V (Å^3), and B (GPa).

Structure	ΔU	U	V	B
fcc	-0.191, 0.359, 0.449	-5.538, -4.989, -4.899	16.235, 15.879, 13.928	491.016, 465.410, 88.976
hcp	-0.195, 0.312, 0.420	-5.542, -5.036, -4.928	16.188, 15.851, 13.822	498.448, 486.871, 94.317
β-Sn	0.238, 0.443, 0.208	-5.109, -4.905, -5.140	17.295, 17.268, 14.839	152.112, 173.423, 113.781
bc8	0.365, 0.329, 0.125	-4.982, -5.019 ,-5.222	18.183, 18.147, 17.902	99.767, 104.9491, 100.562
clathrate 34	-0.020, 0.017, 0.078	-5.367, -5.333, -5.269	22.139, 22.411, 22.791	93.301, 89.462, 81.050
diamond	0.000, 0.000, 0.000	-5.347, -5.348, -5.348	19.725, 19.760, 19.742	93.104, 94.263, 93.658
diamond [164]	0.000	-5.407	18.826	175.417

3.2.3 Equilibrium properties of diamond ground state

Table 3.8 gives equilibrium properties of silicon diamond for reduced TB (LCN) and DFT. The column named reduced TB shows the results of the reduced TB (LCN) model from this study, and the column named DFT shows the results of the DFT calculations performed in this study using LDA. The reduced TB equilibrium binding energy, equilibrium volume, and bulk modulus are in good agreement with the DFT results. In addition, the elastic constants are fairly well reproduced. Experimental data and a TB model by Lenosky *et al.* [187] are also included for comparison. We have chosen the model by Lenosky *et al.* from all the different TB fits as the most comprehensive fit to silicon diamond properties. The major difference between the Lenosky *et al.* and our approach is that Lenosky *et al.* fitted to the equilibrium properties of silicon diamond, including elastic constants, phonon frequencies, Grüneisen parameters, and point defect energies, whereas we only optimised fitting the binding energy curves. The effect of the different approaches can be seen by comparing the binding energies of the reduced TB and DFT columns with the binding energies of the experimental and Lenosky *et al.* columns.

In addition to equilibrium properties, we test the silicon reduced TB model for point defects. Table 3.9 gives point defect formation energies in silicon. The energies are calculated using a silicon box of 128 atoms from which the defected structures are generated. This means the vacancy structure contains 127 atoms and the split-(110), hexagonal, and tetrahedral structures contain 129 atoms. The unrelaxed results are obtained from the starting configuration with the atoms being fixed with respect to the internal degrees of freedom. The relaxed results are obtained from lifting this constraint and by starting from the unrelaxed positions. The reduced TB model gives relatively high energies for the unrelaxed structures due to short

Table 3.8: Equilibrium properties of silicon diamond for reduced TB (LCN) and DFT. Equilibrium binding energy (U), equilibrium volume (V), and bulk modulus (B) are obtained from Birch-Murnaghan equation of state fits to binding energies. Units are U (eV/atom), V (Å^3), and B and C (GPa). C_{44}^0 is the static C_{44} elastic constant.

	Reduced TB	DFT	Expt.	TB[a]
U	-5.348	-5.348	-4.63[b]	-4.620[a]
V	19.760	19.742	20.026[c]	19.999[a]
B	94	94	100[c]	100[a]
C'	63	48.5	51[d,e]	50.4[a,e]
$C44$	111	76	80[d]	75[a]
$C44^0$	144	106	f	f
$C11$	178	161	166[d]	167[a,e]
$C12$	52[e]	65[e]	64[d]	67[a,e]

[a]Reference [187].
[b]Reference [112].
[c]Reference [188].
[d]References [189, 190].
[e]Calculated from other elastic constants.
[f]Not available.

interatomic distances generated by the initial configuration of the interstitial atom where the Yukawa-type core repulsion is effective. Overall, the reduced TB model overestimates the relaxed point defect formation energies relative to DFT. Further, the reduced TB model predicts an unstable hexagonal defect which relaxes into a tetrahedral defect configuration. However, despite the unstable hexagonal defect predicted by reduced TB, the energetically ordering of the defects tetrahedral $\rightarrow$ split-(110) $\rightarrow$ vacancy as predicted by our DFT calculations is reproduced by our reduced TB model.

Table 3.9: Point defect formation energies in silicon diamond (eV). The numbers in parentheses in the top line are the number of atoms per perfect unit cell, whereas the pair of numbers in parentheses in the DFT column from Ref. [191] are LDA and GGA values respectively.

	Reduced TB (128)		DFT (128)		DFT [191] (64)	TB [187] (144)	
	Unrelaxed	Relaxed	Unrelaxed	Relaxed	Relaxed	Unrelaxed	Relaxed
Vacancy	7.526	5.492	3.795	3.577	(a, a)	3.915	3.708
Split-(110)	7.743	5.327	4.949	3.340	(3.31, 3.84)	a	3.215
Hexagonal	11.839	4.862	5.961	3.378	(3.31, 3.80)	4.733	3.814
Tetrahedral	6.951	4.862	3.772	3.339	(3.43, 4.07)	4.067	3.600

[a]Not available.

3.3 Summary

In this Chapter we presented a reduced TB model for silicon. This model reproduces the DFT DOS and projected DOS of the silicon diamond structure qualitatively well. The difference between the DOS calculated with DFT and projected TB can be attributed to the fact that on-site level values different from the output of the projection scheme were used. In addition, the difference between the DOS calculated with projected TB and reduced TB can be attributed to how well reduced TB approximates the two-centre orthogonal TB bond integrals. Without considering the close packed structures fcc and sh, the reduced TB model reproduces the ordering diamond $\rightarrow$ clathrate $\rightarrow$ bc8 $\rightarrow$ β-Sn predicted by the DFT binding energies. Furthermore, we show that we can achieve a reasonable trade off between relative ordering of structures and properties for the ground state diamond structure by setting p_σ as a constant rather than as a function of interatomic distance R. The reduced TB model for silicon overestimates the relaxed point defect formation energies relative to DFT and predicts an unstable hexagonal defect which relaxes into a tetrahedral defect configuration. However, the energetically defect ordering tetrahedral $\rightarrow$ split-(110) $\rightarrow$ vacancy as predicted by our DFT calculations is reproduced by our reduced TB model.

4 Reduced TB Model for Nitrogen

In Chapter 3 we gave details of the reduced TB model for silicon. In this Chapter we introduce the reduced TB model for nitrogen. Similar to the previous Chapter, we first show the two-centre TB bond integrals obtained from DFT. We then provide details of the reduced TB parameters and show the electronic structure of the nitrogen cubic gauche (cg) structure. Finally we show binding energy curves and give results of nitrogen reduced TB model tests. The results provided include equilibrium binding energy, equilibrium nearest neighbour distance, and frequency of the dimer.

4.1 Bond Integrals

Figure 4.1 shows the projected two-centre orthogonal TB bond integrals obtained from DFT for different structures of nitrogen. Again, the data for equilibrium structures is displayed with enlarged symbols. Compared to the silicon data in Figure 3.1, the data for nitrogen appears to be less structure dependent.

The nitrogen reduced TB parameters are displayed in Figure 4.2. Similar to the two-centre orthogonal TB bond integrals, the reduced TB parameters for nitrogen are less structure dependent than those displayed for silicon in Figure 3.2. As expected, the β_π data is short ranged compared to the β_σ data. The functions $\beta_\sigma(R)$, $\beta_\pi(R)$, and $p_\sigma(R)$ are fitted in a similar fashion to that described for silicon.

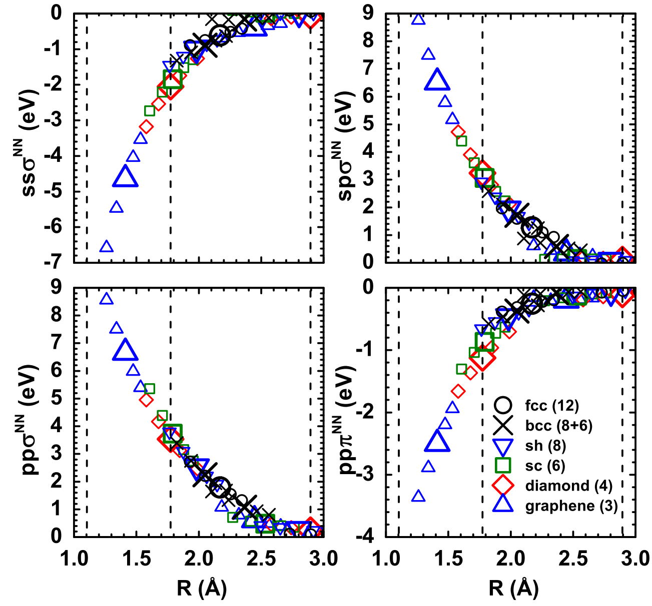

Figure 4.1: Two-centre orthogonal TB N-N bond integrals obtained from DFT via projection scheme for different structures as a function of interatomic distance R. Equilibrium data are displayed with enlarged symbols. Dashed vertical lines are, from left to right, the first nearest neighbour distance in the ground state equilibrium dimer, R_1^{dimer}, and the first and second nearest neighbour distances in the equilibrium diamond structure, $R_1^{\diamond}$ and $R_2^{\diamond}$.

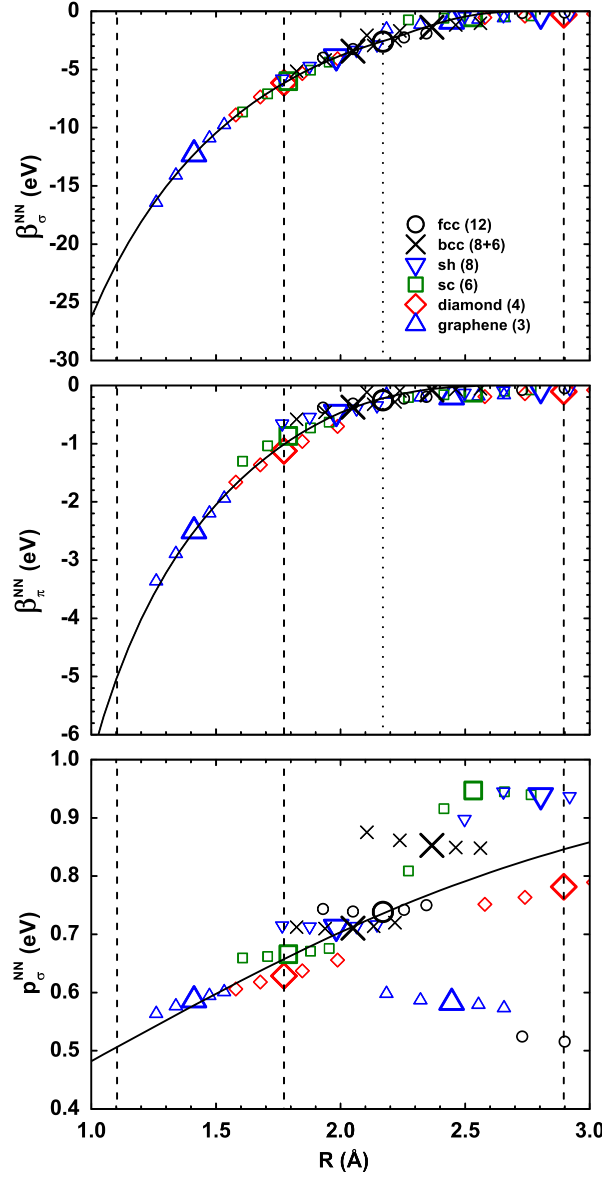

Figure 4.2: Reduced TB N-N parameters calculated from projected bond integrals in Figure 4.1 for different structures as a function of interatomic distance R. Equilibrium data are displayed with enlarged symbols. Dashed vertical lines are, from left to right, the first nearest neighbour distance in the ground state equilibrium dimer, R_1^{dimer}, and the first and second nearest neighbour distances in the equilibrium diamond structure, $R_1^{\diamond}$ and $R_2^{\diamond}$. The vertical dotted line marks R_{tail}.

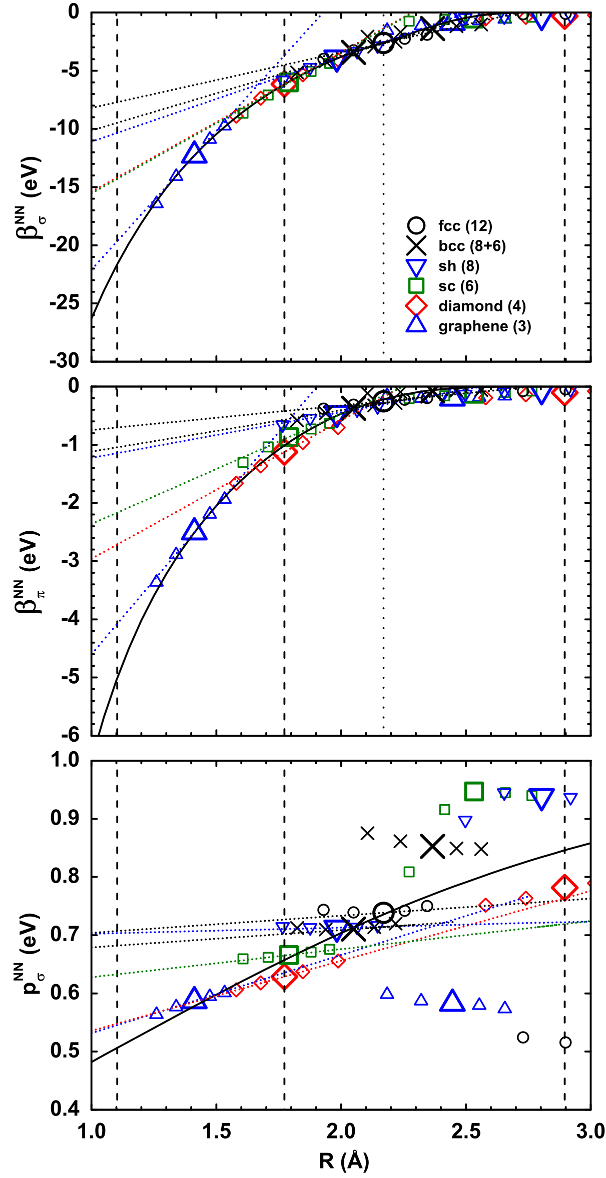

Figure 4.3: Reduced TB N-N parameters from Figure 4.2 including the gradients at the equilibrium first nearest neighbour distance in each structure of nitrogen.

Since the β_σ and β_π data for nitrogen in Figure 4.2 is less structure dependent than that of silicon, it can be better approximated by a single distance dependent function. Overall, the functions $\beta_\sigma(R)$ and $\beta_\pi(R)$ reproduce the data and distant-dependent gradients well. Compared to the β_σ and β_π data, the nitrogen p_σ data is more structure dependent and the gradients of the individual structures are only poorly reproduced (see Figure 4.3). Again, for the same reasons given for the silicon model, we set $p_\sigma(R)$ as a constant. For nitrogen, we extrapolate the $p_\sigma(R)$ function to the dimer equilibrium distance and chose that value. This approach seems to be the best choice to achieve the correct relative ordering of metastable structures.

The parameters of the functions representing the reduced TB parameters for the nitrogen reduced TB model are given in Table 3.1 and the on-site levels are given in Table 3.2.

The density of states for the nitrogen cubic gauche (cg) structure calculated with DFT, projected TB, and reduced TB is shown in Figure 4.4. Similar to the density of states for the silicon ground state diamond structure each DOS is shifted along the energy scale such that the Fermi energy is at zero eV and the features of the DFT density of states are qualitatively reproduced by projected TB and reduced TB. Again, projected TB and reduced TB reproduce the sp-hybridisation of the DFT density of states well. See the discussion for the density of states for the silicon ground state diamond structure in Chapter 3 on the reproduction of the valence band width when going from projected TB to reduced TB. Figure 4.5 displays the two-centre orthogonal TB N-N bond integrals from Figure 4.1 including the functions that show how well the bond integrals are approximated by reduced TB. One can see that at the nearest neighbour distance in the equilibrium diamond structure reduced TB underestimates the magnitude of the $sp\sigma$, $pp\sigma$, and $pp\pi$ bond integrals,

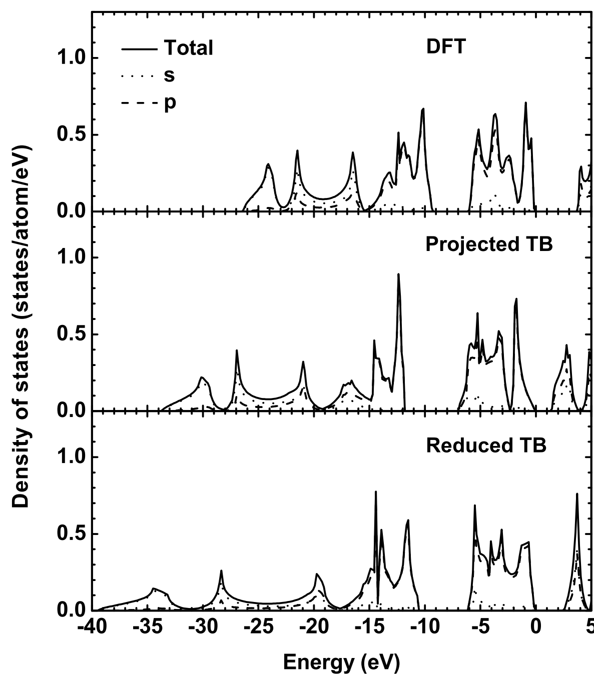

Figure 4.4: s and p contributions to the average total density of states of the nitrogen cubic gauche (cg) structure for DFT, projected TB, and reduced TB. For the calculation of the projected TB DOS the same on-site levels were used as for the calculation of the reduced TB DOS.

while overestimates the magnitude of the $ss\sigma$ bond integral.

The distance dependence of the nearest neighbour σ and π bond orders of nitrogen are displayed in Figure 4.6 for the dimer, cubic gauche (cg), diamond, and simple cubic (sc) structures with coordination numbers of 1, 3, 4, and 6, respectively. The nitrogen dimer has a saturated σ bond and two saturated π bonds. The cubic gauche structure has a saturated σ and two unsaturated π bonds. This is equivalent to three single bonds and a lone pair per atom. The diamond structure has one half saturated σ and two unsaturated π bonds. The character of the nearest neighbour bond in the simple cubic structure is similar to the character of the nearest neighbour bond in

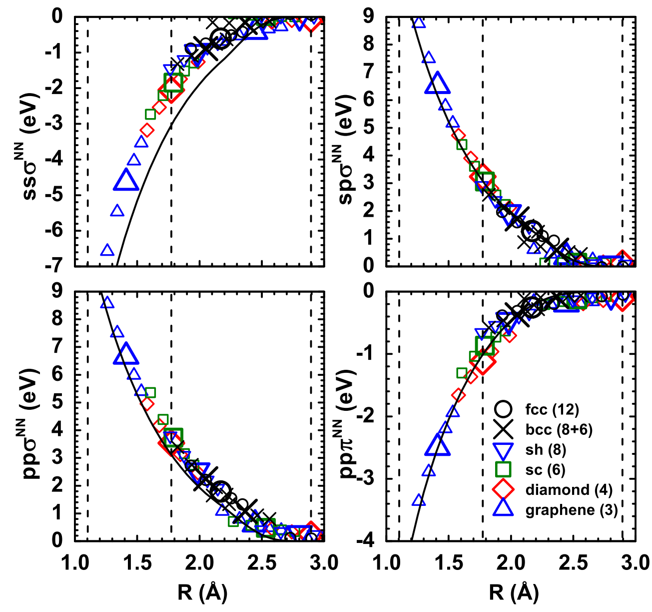

Figure 4.5: Two-centre orthogonal TB N-N bond integrals from Figure 4.1 including the functions that show how well the bond integrals are approximated by reduced TB.

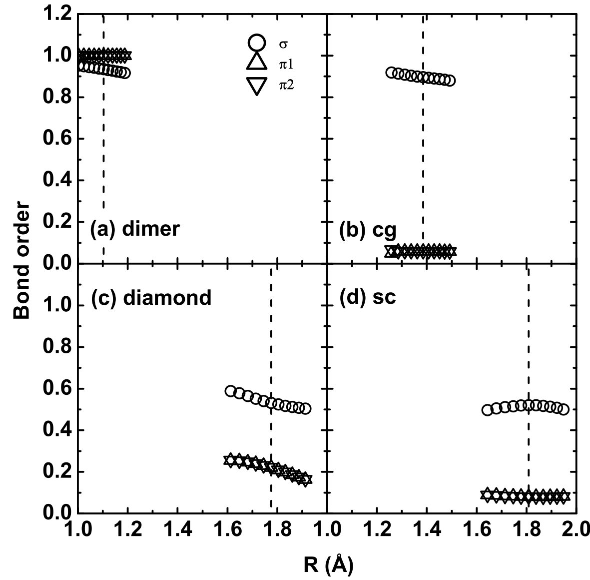

Figure 4.6: σ and π bond orders for a first nearest neighbour bond in the nitrogen (a) dimer, (b) cubic gauche (cg), (c) diamond, and (d) simple cubic (sc) structures as a function of interatomic distance R.

the diamond structure, although both σ and π bonds in the simple cubic structure are less saturated. Similar to the bond order values of different silicon structures in Figure 3.6, the total bond order at equilibrium nearest neighbour distances varies approximately inversely with the coordination number. This shows Figure 3.7.

4.2 Binding Energy Curves

To be able to calculate binding energies for the nitrogen reduced TB model, a repulsive function is obtained as discussed previously for silicon. Figure 4.7 shows the reduced TB (LCN) binding energy curves for different nitrogen structures in the right-hand panel. As a comparison, the DFT binding energy curves are given in the left-hand panel. The parameters of the repulsive function for the nitrogen model

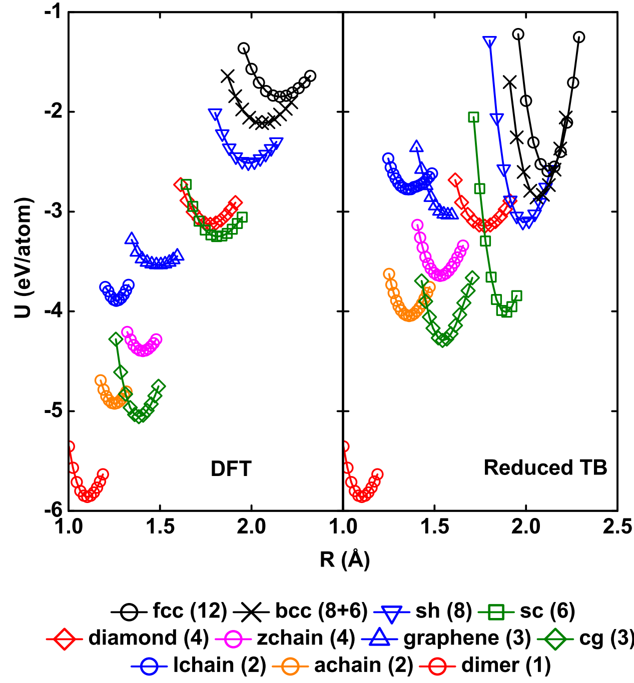

Figure 4.7: DFT and reduced TB (LCN) binding energy curves for different nitrogen structures as a function of nearest neighbour interatomic distance R. The number of nearest neighbours is given in parenthesis for each structure.

are given in Table 3.3. The embedding exponent, and the shift in the nonmagnetic DFT free atom reference energy are given in Table 3.4. For the nitrogen reduced TB (LCN) model no Yukawa-type core repulsion is used.

4.2.1 DFT binding energy curves

As expected, the DFT binding energy curves for nitrogen show that the dimer has the lowest binding energy. The lowest metastable structure is the threefold coordinated cubic gauche (cg) structure. This structure is a body centred cubic structure with four atoms per primitive cell. The second lowest metastable structure

is the armchair chain (achain) structure with bond angles chosen to be 135 degrees. The third lowest metastable structure is the zig-zag chain (zchain) structure with bond angles of 90 degrees. Even though this structure is a chain-like structure, it is fourfold coordinated due to the arrangement of the atoms resulting from the 90 degree bond angles. The fourth most stable metastable structure is the linear chain (lchain) structure. In this structure every atom has two nearest neighbours and it is equivalent to the zchain structure, but with bond angles of 180 degrees. Overall, the DFT binding energy curves in Figure 4.7 agree very well with Figures 1 and 3 of Mailhiot *et al.* [37].

4.2.2 Reduced TB binding energy curves

As one can see from Figure 4.7, the dimer is predicted to be the ground state structure by the reduced TB model. Further, the ordering dimer $\rightarrow$ cg $\rightarrow$ achain $\rightarrow$ zchain predicted by the DFT binding energy data is reproduced by the reduced TB model. In addition, the crossing of the diamond and the sc structures is reproduced. Further, the ordering of the close packed structures sh $\rightarrow$ bcc $\rightarrow$ fcc is also reproduced by the reduced TB model. The nitrogen structures used as a binding energy benchmark together with their binding energies are given in Table 4.1.

4.2.3 Equilibrium properties of dimer ground state

Table 4.2 gives equilibrium properties of the nitrogen dimer for reduced TB (LCN) and DFT calculated in this study. Experimental and DFT results from other studies are also included for comparison. Overall, the equilibrium properties of the dimer ground state predicted by the reduced TB model agree very well with the DFT

Table 4.1: Nitrogen structures used as a binding energy benchmark. Equilibrium binding energies (eV/atom) are given in parentheses (reduced TB, DFT). The structures are ordered with respect to DFT binding energies.

hp7 (-2.001, -1.794)	st12W (-1.766, -1.802)	μ (-2.007, -1.806)
hp12 (-1.821, -1.809)	fcc (-2.613, -1.848)	A13 (-2.411, -1.868)
A15 (-2.305, -1.872)	A6 (-2.638, -1.880)	A12 (-2.246, -1.898)
A3' (-2.680, -1.902)	C19 (-2.695, -1.915)	hcp (-2.725, -1.934)
Ab (-2.471, -1.947)	γMoPt$_2$ (-2.628, -2.004)	of8 (-2.804, -2.029)
Aa (-2.933, -2.038)	mc34 (-2.668, -2.091)	bcc (-2.869, -2.114)
hr22 (-2.680, -2.148)	A10 (-2.621, -2.169)	Gaoc4 (-2.841, -2.295)
oc4 (-3.128, -2.335)	ci12 (-4.295, -2.340)	A20 (-3.151, -2.362)
Gamc4 (-3.045, -2.449)	Ad (-3.231, -2.484)	A11 (-2.885, -2.490)
sh (-3.112, -2.510)	Af (-3.330, -2.578)	Ac (-3.184, -2.669)
mp4 (-3.051, -2.704)	β-Sn (-3.445, -2.757)	mc4 (-3.479, -2.778)
Ai (-3.587, -2.951)	A14 (-3.801, -2.977)	bct5 (-3.572, -3.083)
diamond (-3.151, -3.126)	bc8 (-3.497, -3.231)	sc (-4.021, -3.252)
st12 (-3.631, -3.309)	A8 (-4.117, -3.405)	graphene (-3.037, -3.538)
A9 (-3.037, -3.559)	A7 (-4.515, -3.817)	lchain (-2.686, -3.893)
zchain90 (-3.634, -4.397)	A17 (-4.498, -4.621)	Pba2 (-4.264, -4.850)
cg (-4.403, -5.055)	achain (-4.328, -5.062)	zchain (-4.308, -5.240)
dimer (-5.860, -5.860)	–	–

Table 4.2: Equilibrium properties of the nitrogen dimer for reduced TB (LCN), DFT, and experiment. Equilibrium binding energy (U), equilibrium nearest neighbour distance (NND), and frequency ν are obtained from Birch-Murnaghan equation of state fits to binding energies. Units are U (eV/atom), NND (Å), ν (cm^{-1}). The pair of numbers in parentheses in the DFT column from Ref. [192] are LDA and GGA values respectively.

	Reduced TB	DFT	Expt.	DFT [192]
U	-5.872	-5.860	-4.903[a]	(-5.666, -5.279)
NND	1.099	1.103	1.10[a], 1.112[b], 1.098[c]	(1.107, 1.113)
ν	2610	2615	2359[c], 2360[d], 2361[e]	(2465, 2351)

[a]Reference [193].
[b]Reference [194].
[c]Reference [195].
[d]Reference [196].
[e]Reference [192].

calculations and results from other studies.

4.3 Summary

A reduced TB model for nitrogen was developed in this Chapter. This model reproduces the DFT DOS and projected DOS of the nitrogen cubic gauche structure qualitatively. When not considering all structures in the structure database, the reduced TB model for nitrogen reproduces the ordering dimer → cg → achain → zchain and the ordering of the close packed structures sh → bcc → fcc predicted by DFT calculations. Furthermore, the equilibrium binding energy, nearest neighbour distance, and frequency of the nitrogen dimer calculated with the reduced TB model agree well with results from DFT calculations and experimental studies.

5 Reduced TB Model for Silicon Nitride

In Chapters 3 and 4 we introduced the elemental reduced TB models for silicon and nitrogen within the constraint of local charge neutrality (LCN). We will use these elemental bond integrals and repulsive functions in the binary silicon nitride model without further adjustments. However, for the parameterisation of the binary silicon nitride system, charge transfer (CT) is introduced as described in Subsection 2.4.1, so that, unless stated otherwise, all the silicon nitride figures correspond to the model allowing CT. The binary silicon nitride interactions are then obtained in a similar way as the elemental interactions. We also compare the reduced TB CT model for silicon nitride with a reduced TB model enforcing LCN. The latter model will be referred to as reduced TB LCN and the interactions are obtained in a similar fashion as the elemental interactions.

In the following Sections we show the two-centre orthogonal TB bond integrals obtained from DFT via the projection scheme described in Subsection 2.4.1 and the reduced TB parameters obtained from this data. We display the parameters for the reduced TB bond integrals and display the density of states of silicon nitride in the β crystal structure. We further tabulate the repulsive energy parameters for the reduced TB CT model and show heat of formation curves for different structures of silicon nitride for both reduced TB CT and reduced TB LCN and discuss the advantages and disadvantages of both models compared to DFT. In addition, we

give results of tests of the reduced TB CT model in form of equilibrium properties of the β phase ground state and defect formation energies.

5.1 Bond Integrals

The two-centre orthogonal TB Si-N bond integrals obtained from DFT for different structures are shown in Figure 5.1. The data for equilibrium structures is displayed with enlarged symbols. Compared to the data for silicon and nitrogen, the data is moderately structure dependent. Screening of second nearest neighbours can be observed in all the data.

Figure 5.2 displays the reduced TB parameters calculated from the data in Figure 5.1. The first nearest neighbour values for p_σ^{NSi} are smaller than those for p_σ^{SiN}. This difference is obvious when considering the definition of p_σ^{SiN} and p_σ^{NSi} according to Eq. (2.74) and the different behaviour of $ss\sigma^{SiN}$, $pp\sigma^{SiN}$, $sp\sigma^{SiN}$, and $ps\sigma^{SiN}$ in Figure 5.1. The functions $\beta_\sigma(R)$, $\beta_\pi(R)$, and $p_\sigma(R)$ are fitted to equilibrium data points, with the same considerations as for the elemental models. The functions $\beta_\sigma(R)$ and $\beta_\pi(R)$ reproduce the data as well as the gradients of the individual structures fairly well, however, this is not the case for the function $p_\sigma(R)$ (see Figure 5.3). Therefore, for the same reason as given for the elemental models, $p_\sigma^{SiN}(R)$ and $p_\sigma^{NSi}(R)$ are chosen to be constants. The parameters of the functions representing the reduced TB parameters for the silicon nitride TB model are given in Table 3.1. The species dependent atomic on-site Coulomb integrals for silicon and nitrogen required for the inclusion of charge transfer are given in Table 5.1.

Figure 5.4 shows the average total DOS for the silicon nitride β structure calculated with DFT, projected TB, and reduced TB. Again, the density of states are shifted along the energy scale such that the Fermi energy is at zero eV. The

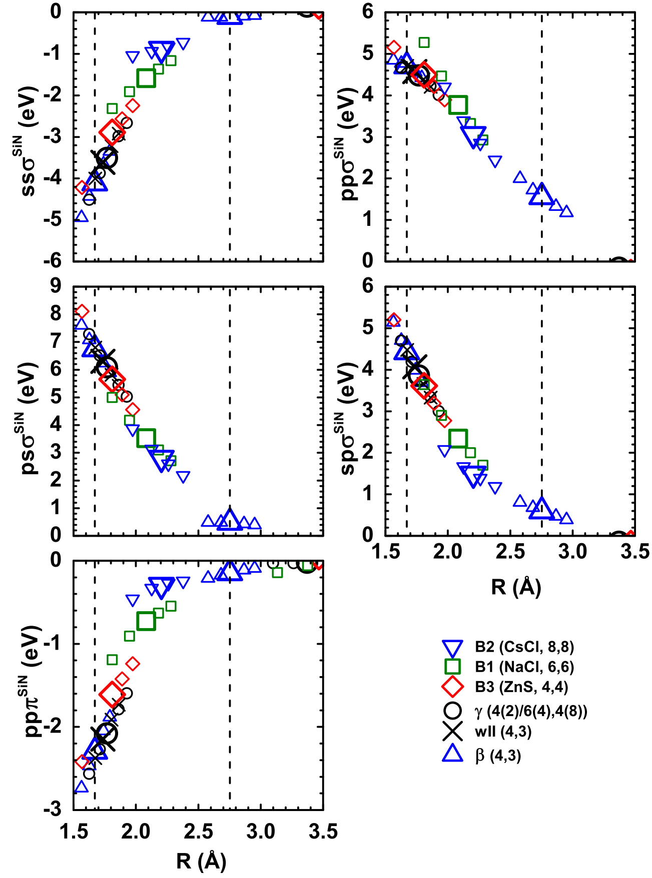

Figure 5.1: Two-centre orthogonal TB Si-N bond integrals obtained from DFT via projection scheme for different structures as a function of interatomic distance R. Equilibrium data are displayed with enlarged symbols. Dashed vertical lines are the first and second nearest neighbour distances in the ground state equilibrium β structure, R_1^β and R_2^β. Note that the $ps\sigma$ data is multiplied by -1 to improve the comparability to the $sp\sigma$ data.

Table 5.1: Species dependent atomic on-site Coulomb integrals for silicon (Si) and nitrogen (N) from Ref. [171].

	Si	N
J (eV/e^2)	7.095	11.919

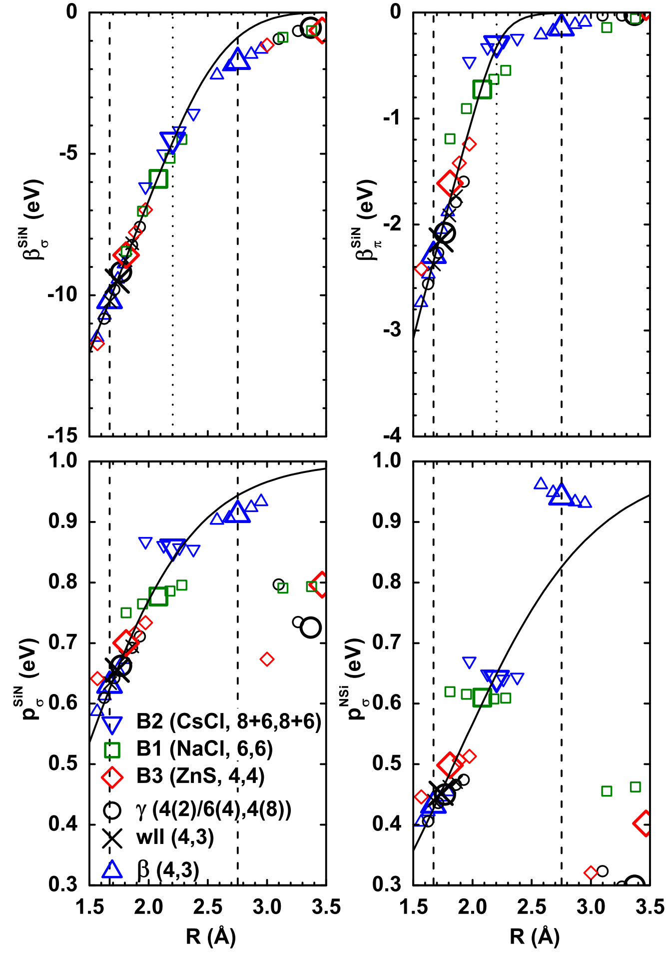

Figure 5.2: Reduced TB Si-N parameters calculated from projected bond integrals in Figure 5.1 for different structures as a function of interatomic distance R. Equilibrium data are displayed with enlarged symbols. Dashed vertical lines are the first and second nearest neighbour distances in the ground state equilibrium β structure, R_1^β and R_2^β. The vertical dotted line marks R_{tail}.

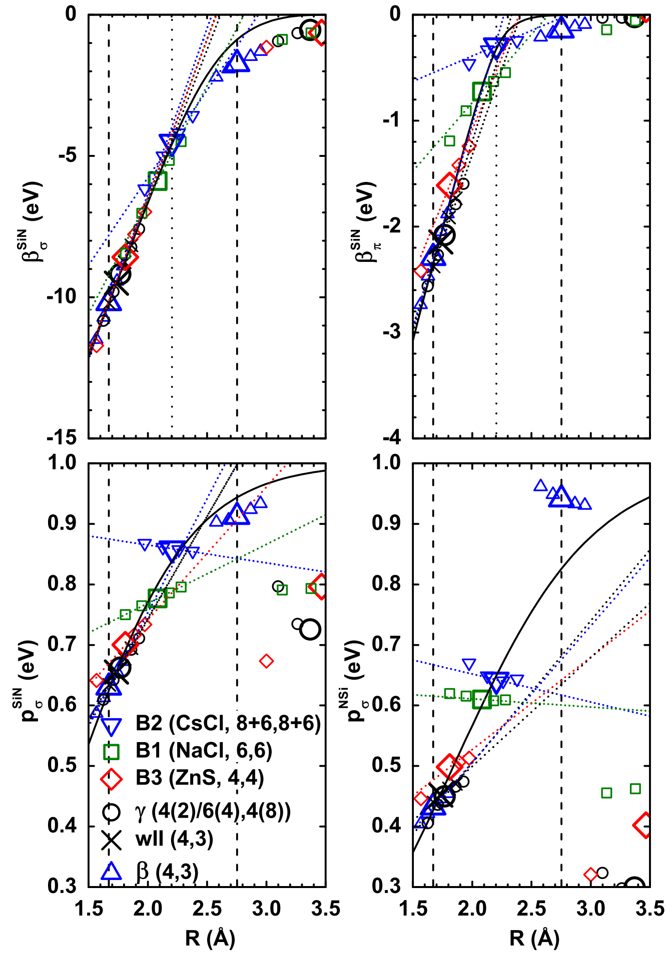

Figure 5.3: Reduced TB Si-N parameters from Figure 5.2 including the gradients at the equilibrium first nearest neighbour distance in each structure of silicon nitride.

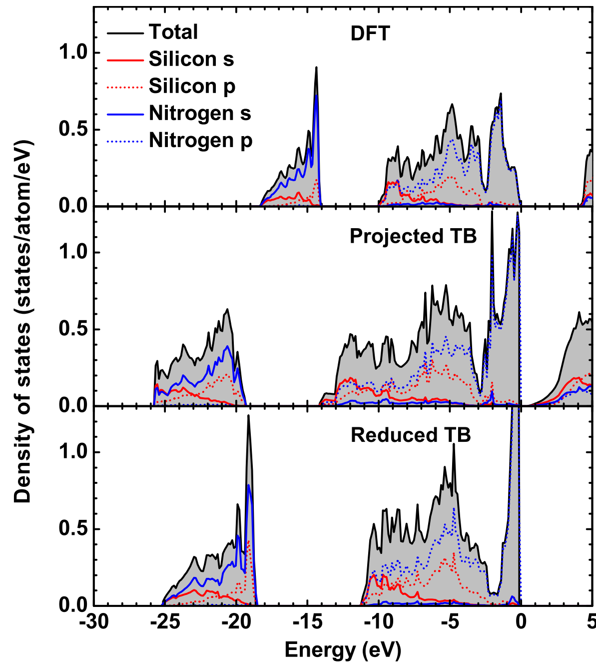

Figure 5.4: Local s and p contributions of silicon and nitrogen to the average total density of states of the silicon nitride β structure for DFT, projected TB, and reduced TB. For the calculation of the projected TB DOS the same on-site levels were used as for the calculation of the reduced TB DOS.

local s and p contributions of silicon and nitrogen to the average total DOS are also displayed. The features of the DFT DOS are qualitatively well reproduced by projected TB and reduced TB. At the nearest neighbour distance in the ground state equilibrium β structure reduced TB slightly underestimates the magnitude of the $sp\sigma$ and $ps\sigma$ bond integrals, and slightly overestimates the magnitude of the $ss\sigma$ and $pp\sigma$ bond integrals (see Figure 5.5). Overall however, compared to the reduced TB models for silicon and nitrogen, reduced TB approximates all of the two-centre orthogonal TB Si-N bond integrals at the nearest neighbour distance in the ground state equilibrium β structure fairly well. This has a positive effect on conserving the valence band width of the DOS when going from projected TB to reduced TB.

Figure 5.6 displays the σ and π bond orders for a first nearest neighbour bond in the silicon nitride β structure as a function of interatomic distance R. In the β structure each silicon atom is surrounded by 4 neighbouring nitrogen atoms and each nitrogen atom is surrounded by 3 neighbouring silicon atoms. Therefore, each silicon atom provides one valence electron to each of the four silicon-nitrogen bonds around silicon and each nitrogen atom contributes 5 valence electrons to the three silicon-nitrogen bonds around nitrogen.

The specific values for the difference in the charge in the β equilibrium structure compared to the respective free atoms are in our study -1.314 electrons per atom for silicon, and +0.990 and +0.973 electrons per atom for the two nitrogen sites N1 and N2, respectively. These values agree very well with the values from the study by Zhao *et al.* [197, 198] who investigated the electronic structure and charge transfer at the silicon-silicon nitride interface using LDA and calculated an average of -1.24 electrons per silicon atom and +0.93 electrons per nitrogen atom in the α and β structures.

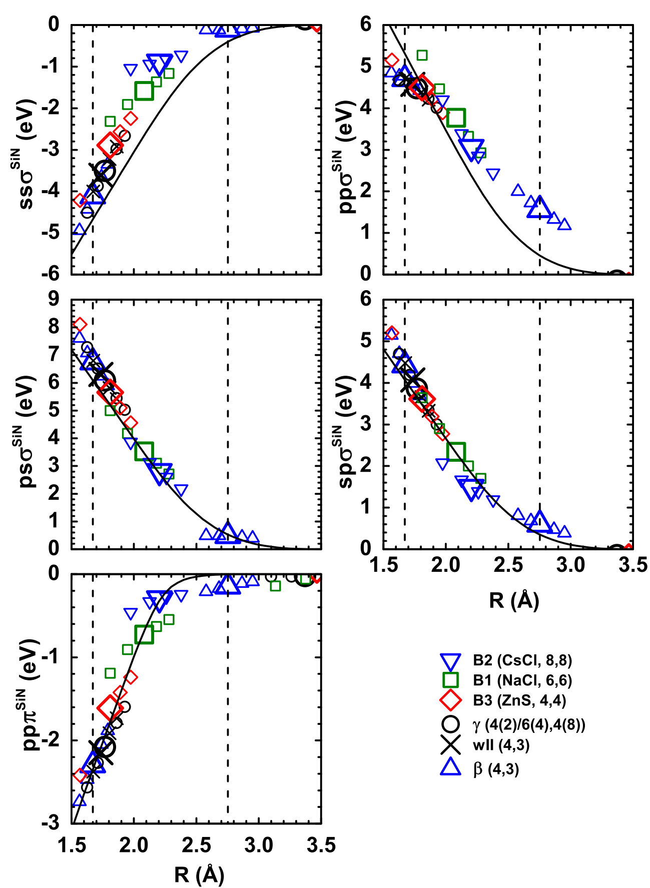

Figure 5.5: Two-centre orthogonal TB Si-N bond integrals from Figure 5.1 including the functions that show how well the bond integrals are approximated by reduced TB.

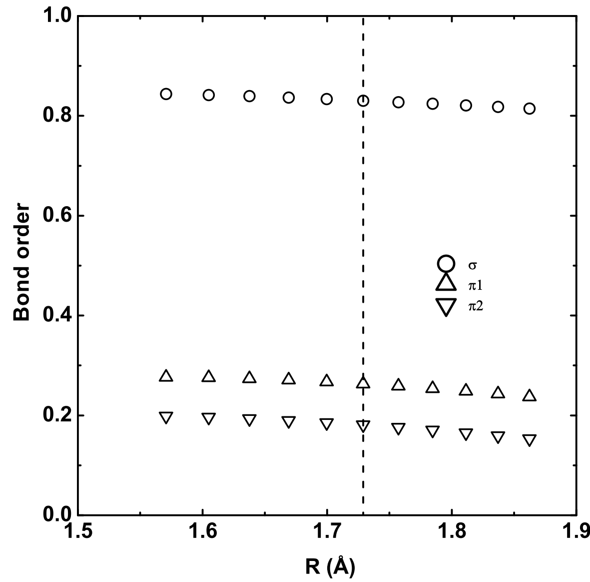

Figure 5.6: σ and π bond orders for a first nearest neighbour bond in the silicon nitride β structure as a function of interatomic distance R.

5.2 Heat of Formation Curves

Figure 5.7 shows the reduced TB CT heat of formation curves for different silicon nitride structures in the right-hand panel. As a comparison, the DFT heat of formation curves are displayed in the left-hand panel and the reduced TB LCN heat of formation curves are displayed in the middle panel. The parameters of the repulsive function for the silicon nitride reduced TB CT model are given in Table 3.3. The elemental embedding exponents, the elemental shifts in the non-magnetic DFT free atom reference energy, and the binary Yukawa parameters are given in Tables 3.4 and 3.5.

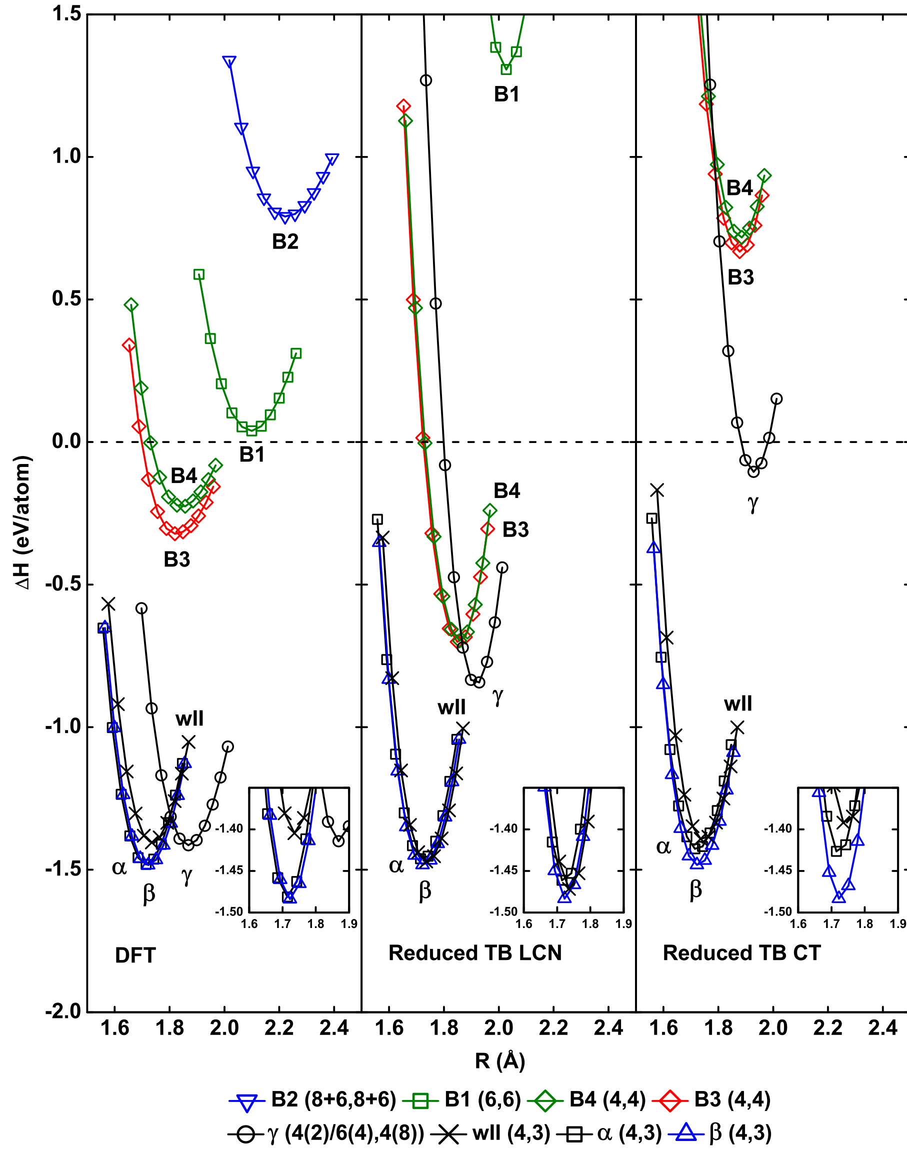

Figure 5.7: DFT, reduced TB LCN, and reduced TB CT heat of formation curves for different silicon nitride structures as a function of nearest neighbour interatomic distance R. The number of nearest neighbours is given in parenthesis for each structure.

5.2.1 DFT heat of formation curves

The DFT heat of formation curves in Figure 5.7 show the Si_3N_4 β phase as the ground state structure. The second lowest structure is α with a 2.5 meV/atom higher equilibrium heat of formation value. This value is consistent with the marginal difference in experimental heat of formation values between these two polytypes [41], and is responsible for the ability to experimentally achieve these two hexagonal crystal structures, which differ only by their stacking sequence, with different processing routes [39]. For both structures the basic building block is a silicon-nitrogen tetrahedron with a silicon atom at its centre and four nitrogen atoms at each vertex. All these SiN4 tetrahedra are linked by nitrogen atoms which are each common to three tetrahedra. As a result each silicon atom has four nitrogen atoms as nearest neighbours and each nitrogen atom has three silicon atoms as nearest neighbours. Therefore, the notation β (4,3) was chosen, where 4 is the number of nearest neighbours of each silicon atom and 3 is the number of nearest neighbours of each nitrogen atom. The third lowest structure predicted by DFT is the cubic γ structure [47] and the fourth lowest structure is the willemite-II (wII) structure [48]. Both structures have the same chemical composition as the β and α structures. In the γ structure however, two of the six silicon atoms have four nearest neighbours, and the other four silicon atoms have six nearest neighbours. All eight nitrogen atoms have four nearest neighbours. Therefore, we chose the notation γ (4(2)/6(4),4(8)). The SiN phases B1, B2, B3, and B4 are the structures NaCl, CsCl, ZnS, and Wurtzite, respectively. From the DFT heat of formation curves the ordering $\beta \rightarrow \alpha \rightarrow \gamma \rightarrow$ wII $\rightarrow$ B3 $\rightarrow$ B4 $\rightarrow$ B1 $\rightarrow$ B2 can be observed.

5.2.2 Reduced TB heat of formation curves

As one can see from the right-hand panel of Figure 5.7, the β structure is predicted to be the ground state structure by the reduced TB model when allowing charge transfer (CT). The β structure is also the ground state structure when considering all structures from the structure database (see Tables 5.2 and 5.3). In addition, the ordering over similar nearest neighbour distances and composition of $\beta \rightarrow \alpha \rightarrow$ wII predicted by the DFT heat of formation data is reproduced by the reduced TB CT model. The ordering of these three structures with respect to each other can be attributed to the fact that they have the same coordination shells. The γ structure, however, has sites with 6 and 8 coordination which the reduced TB CT model fails to describe well. The reduced TB CT model for silicon nitride predicts a heat of formation value for the γ structure which is 1.305 eV/atom higher than the DFT reference value (see Table 5.2). Further, the ordering of the high heat of formation structures, namely B3 $\rightarrow$ B4 $\rightarrow$ B1 $\rightarrow$ B2, with respect to each other is being reproduced. The reduced TB model predicts heat of formation values for B1 and B2 that are out of the scale of the right-hand panel of Figure 5.7. See Tables 5.2 and 5.3 for a comparison of the heat of formation values of the silicon nitride structures used as a benchmark.

The middle panel of Figure 5.7 shows that the reduced TB model when enforcing local charge neutrality (LCN) predicts the β structure to be the ground state structure as well. Further, the ordering over similar nearest neighbour distances, same composition, and same coordination shells of $\beta \rightarrow \alpha \rightarrow$ wII predicted by the DFT heat of formation data is also reproduced by the reduced TB LCN model. Comparing the middle and right-hand panel of Figure 5.7 it can be seen that the reduced TB LCN model reproduces the heat of formation value difference between

Table 5.2: Silicon nitride structures used as a heat of formation benchmark. Equilibrium heat of formation values (eV/atom) are given in parentheses (reduced TB CT, reduced TB LCN, DFT). The structures are ordered with respect to DFT heat of formation values.

D5-19-A3B2 (4.913, 3.751, 1.077)	$B8_2$-A4B2 (4.072, 3.375, 1.064)
C-e-A4B8 (4.030, 3.053, 1.058)	D0-17-A2B6 (4.275, 3.227, 0.992)
μ-AAAAB (2.504, 1.118, 0.982)	L60-A3B (3.214, 3.384, 0.951)
B20 (4.996, 3.945, 0.951)	C37-A8B4 (4.086, 3.653, 0.931)
D5-11-A12B8 (2.807, 2.014, 0.877)	D5-c-A8B12 (4.331, 3.518, 0.861)
C42-A2B4 (1.493, 1.333, 0.845)	B-e-AB (3.219, 1.936, 0.800)
B2 (5.350, 3.960, 0.791)	C23-A4B8 (3.460, 2.205, 0.789)
C22-A3B6 (3.641, 2.303, 0.780)	C24-A2B4 (2.122, 1.493, 0.750)
C22o-A3B6 (3.281, 1.993, 0.627)	C-a-A12B6 (3.647, 3.126, 0.600)
B31 (4.245, 2.884, 0.598)	B8-1 (4.317, 2.863, 0.483)
D0-2-A4B12 (1.495, 0.546, 0.472)	C1-AB2 (2.783, 1.537, 0.450)
L'2-A1B2 (2.609, 1.476, 0.390)	B18 (2.129, 1.033, 0.342)
C43-A4B8 (2.212, 1.130, 0.292)	C46-A8B16 (1.902, 0.878, 0.278)
C34-A1B2 (1.889, 0.766, 0.261)	C3-A4B2 (1.911, 0.462, 0.241)
C25-A4B8 (2.021, 0.969, 0.207)	D5-e-A2B3 (2.115, 1.063, 0.185)
C8-A3B6 (-0.164, 0.895, 0.174)	C33-A3B2 (3.004, 1.436, 0.156)
C10-A4B8 (-0.086, 0.274, 0.147)	C9-A2B4 (-0.074, 0.359, 0.143)
B-i-AB (3.156, 1.453, 0.121)	B24-AB (2.994, 1.424, 0.068)
B-k-AB (0.080, -0.921, 0.040)	B1 (3.056, 1.313, 0.040)
B_h-AB (3.334, 1.699, 0.035)	C5-A2B4 (1.576, 0.826, 0.022)
C21-A8B16 (1.526, 0.861, 0.019)	B10-AB (1.663, 0.114, 0.018)
B26 (1.306, 0.202, 0.003)	B37-A4B4 (2.532, 2.290, -0.028)
D5-8-A8B12 (1.710, 0.882, -0.073)	oP8-AK (0.904, -0.401, -0.119)
tP8-AK (0.904, -0.400, -0.120)	C4-A2B4 (1.465, 0.555, -0.126)
C35-A2B4 (1.614, 0.723, -0.141)	B4 (0.721, -0.696, -0.226)
B29 (2.288, 1.091, -0.228)	B12-AB (0.224, -0.798, -0.249)
B3 (0.672, -0.702, -0.323)	B16-A4B4 (1.496, 0.532, -0.338)
B34-A8B8 (1.280, -0.137, -0.495)	B17-A2B2 (0.680, -0.764, -0.675)
C18-A2B4 (0.821, -0.367, -0.709)	D5-1-A4B6 (0.822, -0.043, -0.902)
wII (-1.397, -1.476, -1.403)	γ (-0.108, -0.852, -1.413)
α (-1.430, -1.466, -1.480)	β (-1.487, -1.487, -1.483)

Table 5.3: Further silicon nitride structures used as a heat of formation benchmark. Equilibrium heat of formation values (eV/atom) are given in parentheses (reduced TB CT, reduced TB LCN, DFT). The structures are ordered with respect to DFT heat of formation values.

D2-b-A1B12 (4.473, 4.217, 3.592)	D2-e-A3B33 (4.330, 3.994, 3.359)
D2-1-A1B6 (3.539, 3.334, 3.274)	μ-BBBBA (3.986, 4.426, 3.030)
D2-d-A1B5 (4.952, 4.672, 2.985)	D1-A4B12 (1.616, 1.745, 2.971)
D2-f-A1B12 (3.237, 5.677, 2.857)	D1-3-A1B4 (4.769, 4.784, 2.795)
dimer (0.645, 1.017, 2.694)	B21 (0.508, 1.171, 2.662)
D1-a-A1B4 (4.978, 3.954, 2.525)	L1-3-AB3 (5.690, 4.644, 2.467)
C14-Laves-AB2 (6.047, 5.141, 2.351)	C36-Laves-A8B16 (6.017, 5.146, 2.337)
C15-Laves-A2B4 (5.991, 5.149, 2.325)	D0'-c-A2B6 (5.376, 4.154, 2.180)
D0-19-A2B6 (5.378, 4.125, 2.177)	L1-2-AB3 (5.469, 4.298, 2.151)
D0-a-A2B6 (5.387, 4.085, 2.140)	C6-A1B2 (6.527, 5.397, 2.131)
D0-c-A2B6 (5.308, 4.122, 2.116)	C32-A1B2 (4.958, 5.244, 2.094)
L60-AB3 (5.148, 4.023, 2.085)	L6-0-AB3 (5.148, 4.023, 2.085)
L2-2-A6B21 (4.374, 3.102, 1.949)	A15-B6A2 (5.174, 4.097, 1.917)
B11-A2B2 (5.668, 5.431, 1.895)	D8-5-A6B7 (5.605, 4.659, 1.841)
$MoPt_2$-γ-AB2 (5.934, 4.823, 1.789)	D8-h-A10B4 (4.053, 4.454, 1.782)
D8-i-A5B2 (3.939, 3.668, 1.751)	C16-A2B4 (5.276, 4.475, 1.731)
C15-Laves-A4B2 (3.122, 4.500, 1.705)	D1-c-A2B8 (3.318, 2.381, 1.684)
C-h-A2B4 (4.244, 3.023, 1.678)	C36-Laves-A2B (3.522, 5.822, 1.669)
L1-1-AB (5.582, 5.242, 1.664)	L1-1 (5.569, 5.241, 1.662)
D0-18-A2B6 (4.376, 3.190, 1.655)	C14-Laves-A2B (3.110, 4.139, 1.633)
D0-15-A2B6 (2.944, 1.857, 1.554)	B-b-AB2 (5.370, 4.104, 1.539)
D0-5-A2B6 (3.180, 2.425, 1.517)	C54-A2B4 (4.946, 3.927, 1.507)
B33 (5.583, 4.369, 1.498)	D0-4-A6B18 (3.129, 2.135, 1.485)
C40-A3B6 (5.020, 3.966, 1.483)	B27 (5.583, 4.394, 1.462)
B-g-AB (5.478, 4.260, 1.457)	B-a (6.089, 5.334, 1.439)
B13 (3.128, 3.076, 1.414)	L1-0-AB (5.825, 5.218, 1.391)
D0-11-A4B12 (3.616, 2.487, 1.352)	B8-2-AB2 (4.872, 3.672, 1.259)
D0-14-A2B6 (2.706, 2.214, 1.228)	B35 (5.590, 5.162, 1.192)
C-a-AB2 (3.729, 2.877, 1.183)	$MoPt_2$-γ-A2B (4.243, 4.098, 1.167)
C38-A4B2 (3.484, 3.898, 1.160)	C7-A2B4 (3.225, 2.350, 1.099)
B-b-A6B3 (3.801, 3.741, 1.091)	D5-a-A6B4 (4.814, 3.959, 1.087)
A15-A6B2 (3.711, 2.748, 1.079)	D0-9-A1B3 (2.739, 2.257, 1.079)

the β and α structures better than the reduced TB CT model. However, the heat of formation value difference between the β and wII structure is better described by the reduced TB CT model. The DFT heat of formation value difference between the β structure and the remaining five structures, namely γ, B3, B4, B1, and B2 is better reproduced by the reduced TB LCN model than by the reduced TB CT model, although all differences between the DFT heat of formation values and the heat of formation values calculated with both reduced TB models is rather large for these five structures.

The heat of formation values of the silicon nitride structures given in Tables 5.2 and 5.3 for DFT, reduced TB LCN, and reduced TB CT are displayed in Figure 5.8 versus nitrogen concentration. Similarly to the phase diagram in Figure 2.1 at 0 °C, all three methods reproduce the fact that Si_3N_4 is the only well-established stoichiometric compound found experimentally in the silicon nitride binary system [35]. Even though our reduced TB CT model predicts values of charge transfer between the silicon and nitrogen atoms comparable to DFT results [197, 198], our reduced TB CT model does not outperform our reduced TB LCN model when it comes to energetically ordering and thermodynamic stability of different structures.

It might be surprising that the heat of formation values for the α, wII, γ, B3, B4, B1, and B2 structures are higher when allowing charge transfer than when enforcing local charge neutrality, which leads to fewer structures in the right-hand panel than in the middle panel of Figure 5.8. To explain this fact we need to consider two effects: first, the lowering of the energy when allowing charge transfer compared to enforcing local charge neutrality, and, second, the increase of the energy when refitting the parameters of the repulsive energy contribution to the binding energy of the ground state β structure. The first effect is always negative and

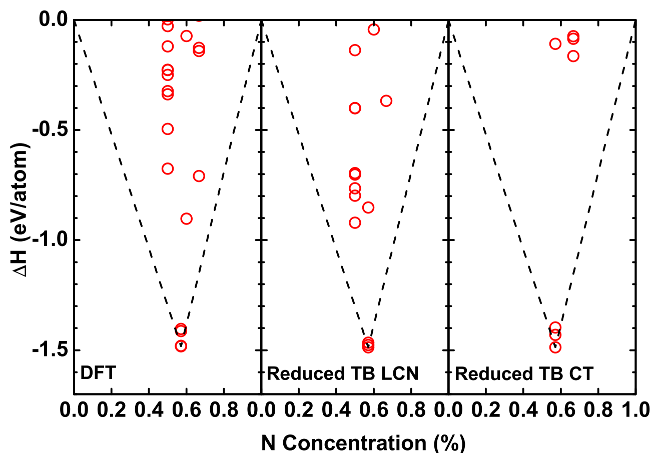

Figure 5.8: Heat of formation for different silicon nitride structures for DFT, reduced TB LCN, and reduced TB CT, versus nitrogen concentration.

concerns the sum of all energy contributions to the binding energy apart from the repulsive energy, since the repulsive energy is not determined by solving the secular equation but rather by fitting its parameters to DFT binding energies. The second effect is always positive to counteract this lowering effect for the ground state equilibrium β structure. We can now investigate which of the two terms is more dominant in the non ground state structures for the particular case of the reduced TB models for silicon nitride presented here. Table 5.4 gives the values of both effects for the ground state equilibrium β structure and seven non ground state equilibrium structures from Figure 5.7. As we can see, whereas for the ground state equilibrium β structure $|\Delta U_{rep}| = |\Delta\left(U_{bind} - U_{rep}\right)|$, for all seven non ground state equilibrium structures the increase in binding energy due to refitting the repulsive energy $|\Delta U_{rep}|$ is larger than the decrease in binding energy due to allowing charge transfer $|\Delta\left(U_{bind} - U_{rep}\right)|$. In a previous model we observed that $|\Delta U_{rep}|$ was smaller than $|\Delta\left(U_{bind} - U_{rep}\right)|$ for these seven non ground state structures. Furthermore, in that particular reduced TB CT model the description of six (α, γ, B1, B2, B3, B4)

Table 5.4: Lowering of the energy when allowing charge transfer compared to enforcing local charge neutrality ($\Delta\left(U_{bind} - U_{rep}\right)$) and increase of the energy when refitting the repulsive energy to the binding energy of the ground state β structure (ΔU_{rep}) for different structures of silicon nitride. Units are eV/atom.

	$\Delta\left(U_{bind} - U_{rep}\right)$	ΔU_{rep}
B2	-1.826	3.984
B1	-1.690	3.619
B4	-1.224	2.766
B3	-1.244	2.730
γ	-2.277	3.176
wII	-2.278	2.358
α	-2.273	2.302
β	-2.286	2.286

of the seven structures mentioned above was better compared to DFT, however, the most stable structure was wII and not β.

Figure 5.9 shows the binding energy contributions according to Eq. (2.47) for different silicon nitride structures for the reduced TB CT model. By considering the individual contributions to the binding energy for the structures β, α, and wII, the driving factors for the relative stability can be examined. For example, the ordering $\beta \rightarrow \alpha$ can be mainly attributed to the bond energy. At β equilibrium nearest neighbour distance, the bond energy contributes to the stabilization of the β structure compared to the α structure with 0.420 eV/atom. Further, a marginal stabilization of the β structure compared to the α structure can be observed in the U_{ion}^{intra} and U_{ion}^{inter} energy contributions, which both have a stabilization effect of only 0.004 eV/atom. This value in energy difference is not significant since its magnitude is similar to the accuracy of the model for which the energy differences are converged to within 0.005 eV/atom. The fact that the reduced TB model is able to destabilize the wII structure compared to the β and α structures can be mainly attributed to

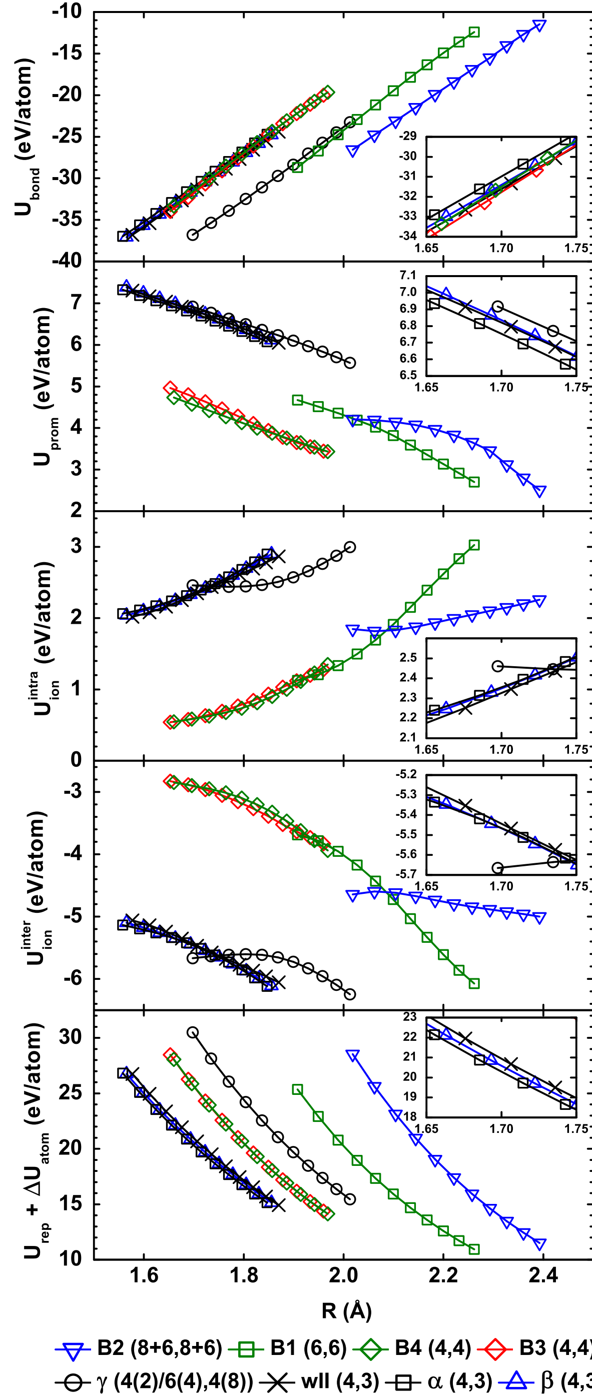

Figure 5.9: Binding energy contributions for different silicon nitride structures for reduced TB CT as a function of interatomic distance R.

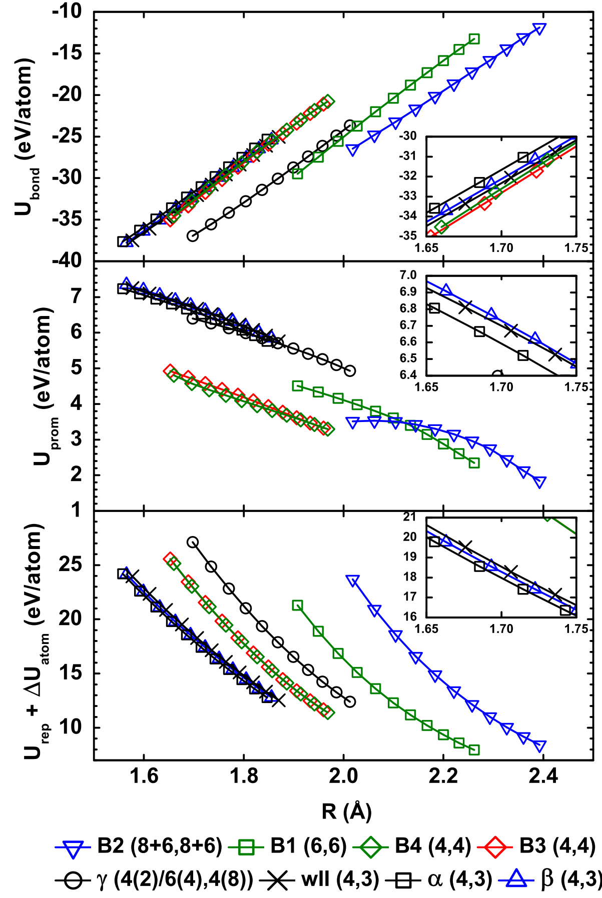

Figure 5.10: Binding energy contributions for different silicon nitride structures for reduced TB LCN as a function of interatomic distance R.

the repulsive energy, with 0.318 eV/atom being the difference in repulsive energy between the wII and the β structure. In addition, U_{ion}^{inter} has a tiny effect with 0.022 eV/atom, too. Even though our reduced TB CT model reproduces the fact that charge transfer is present in silicon nitride, the contributions U_{ion}^{intra} and U_{ion}^{inter} to the binding energy seem to have only a minor effect on the relative ordering $\beta \rightarrow \alpha \rightarrow$ wII.

For comparison, the binding energy contributions for the same structures for

reduced TB LCN are displayed in Figure 5.10. By comparing the repulsive energy contributions in Figures 5.9 and 5.10, one can notice the earlier described increase in the repulsive energy due to refitting the repulsive parameters after allowing charge transfer. Furthermore, it can be seen that the bond and promotion energies for the β, α, wII, and γ structures calculated with the reduced TB LCN model are smaller than those calculated with the reduced TB CT model. Therefore, since U_{ion}^{intra} is positive, U_{ion}^{inter} is the driving force behind the negative values of $\Delta\left(U_{bind} - U_{rep}\right)$ in Table 5.4.

5.2.3 Equilibrium properties of β phase ground state

Table 5.5 gives equilibrium properties of the silicon nitride β structure for reduced TB CT and DFT using LDA. The reduced TB equilibrium heat of formation, equilibrium volume, and bulk modulus are in good agreement with the DFT results. In addition, the elastic constants are fairly well reproduced. Experimental data, DFT results from other studies, and results from force field calculations are also included for comparison. Compared to the results obtained with DFT, the equilibrium heat of formation, equilibrium volume, and bulk modulus are slightly overestimated by our reduced TB CT model. Furthermore, except for the elastic constant C33, all elastic constants are underestimated by our reduced TB CT model compared to our results from DFT calculations.

To our knowledge, studies of simple point defects in pure crystalline silicon nitride have not been discussed in the literature, which may be due to the fact that defects like elemental bond formation are not found experimentally in stoichiometric silicon nitride [199]. More frequently found defects include oxygen [46] and hydrogen [199] contaminations. Therefore, we test our silicon nitride reduced TB CT model for

point defects only to compare with DFT results and not to reproduce experimental values.

Table 5.5: Equilibrium properties of the silicon nitride β structure for reduced TB CT and DFT. Equilibrium heat of formation (ΔH), equilibrium volume (V), and bulk modulus (B) are obtained from Birch-Murnaghan equation of state fits to binding energies. Units are ΔH (eV/atom), V (Å^3), B and C (GPa). The FF column displays values of the force field at 0 Kelvin and B is calculated from other elastic constants.

	Reduced TB CT	DFT	Expt.	DFT	FF[200]
ΔH	-1.487	-1.483	-1.261[a]	b	b
V	10.331	10.290	(10.423, 10.410, 10.423, 10.400)[c]	(10.647, 10.303)[d], 10.302[e], 10.619[f]	9.978, 10.429, 10.454
B	303	254	273[g]	270[e], 234[f]	285
$C11$	410	423	343[h]	409[e], 413[f]	448
$C12$	191[i]	200[i]	136[h]	271[e], 198[f]	215
$C13$	91[i]	117[i]	120[h]	201[e], 116[f]	165
$C33$	591	553	600[h]	604[e], 544[f]	580
$C44$	93	99	124[h]	108[e], 99[f]	115

[a]Reference [41]
[b]Not available
[c]Reference [46]
[d]Reference [201] (GGA, LDA)
[e]Reference [202] (LDA)
[f]Reference [26] (GGA)
[g]Reference [203]
[h]Reference [204]
[i]Calculated from results of C11-C12 and C11+C33-2C13 deformations.

Table 5.6: Relaxed point defect formation energies in silicon nitride β (eV) with 112 atoms per perfect unit cell.

	Reduced TB CT (112)	DFT (112)
Si vacancy	9.612	10.843
N1 vacancy	6.205	5.692
N2 vacancy	5.991	6.126
Si(N1) antisite	13.892	11.972
Si(N2) antisite	12.000	10.823

Table 5.6 gives relaxed point defect formation energies in the silicon nitride β structure with 112 atoms per perfect unit cell. Therefore, the vacancy structures have 111 atoms per unit cell and the antisite structures have 112 atoms per unit cell. N1 and N2 correspond to the two different nitrogen atomic sites in the β structure. Overall, the formation energies calculated with the reduced TB CT model are comparable to the values obtained with DFT. The silicon vacancy defect formation energy is larger than both nitrogen vacancy defect formation energies calculated with both DFT and reduced TB CT. However, the two nitrogen vacancies don't seem to relax into the same minimum when relaxing with DFT and reduced TB CT. Furthermore, both silicon antisite defects have the same ordering for DFT and reduced TB CT with respect to their formation energies. However, similarly to the silicon vacancy formation energies, the formation energies calculated with DFT and reduced TB CT differ by more than 1 eV.

5.3 Summary

The reduced TB model for silicon nitride presented in this Chapter demonstrates the transferability of the reduced TB parameters between different environments as the elemental interactions are used in the binary model without further adjustment. The DFT DOS for the silicon nitride β structure is qualitatively well reproduced by projected TB and reduced TB allowing charge transfer (CT). Furthermore, the valence band width when going from projected TB to reduced TB is being reproduced well compared to the DOS for the silicon diamond structure and the nitrogen cubic gauche structure. This can be attributed to the fact that reduced TB approximates the two-centre orthogonal TB Si-N bond integrals at the nearest neighbour distance in the ground state equilibrium β structure well. In addition, the charge transfer we obtain with our reduced TB CT model in the β equilibrium structure is in good agreement with other DFT studies.

The reduced TB CT model reproduces the ordering of DFT heat of formation curves over similar nearest neighbour distances and composition of $\beta \rightarrow \alpha \rightarrow$ wII and B3 $\rightarrow$ B4 $\rightarrow$ B1 $\rightarrow$ B2. However, the heat of formation values calculated for the γ structure do not fit into the ordering predicted by DFT. The reduced TB CT model calculates equilibrium heat of formation, equilibrium volume, and bulk modulus values for the silicon nitride β structure that are in good agreement with DFT results. Results of elastic constants and point defect formation energies are only fairly well reproduced.

Furthermore, we compare the reduced TB CT model for silicon nitride with a reduced TB model enforcing local charge neutrality (LCN). Even though we observe charge transfer in our calculations with the reduced TB CT model comparable to other studies, an advantage of the reduced TB CT model over the reduced TB

LCN model with respect to the energetically ordering and thermodynamic stability of different structures is not observable. This is mainly due to the large influence that the fitting of the repulsive energy to reference binding energies has on the final reduced TB binding energies.

6 Bond-order Potential for Silicon

In the previous three Chapters we presented the individual contributions to the reduced TB models for the silicon nitride system. This Chapter is devoted to the bond-based bond-order potential (BOP) for silicon. The same reduced TB parameters are employed as for the silicon reduced TB model. The repulsive parameters have been fitted in the same fashion as for the reduced TB models and we tabulate those values in this Chapter. Furthermore, we provide the binding energy curves and give details of tests of the BOP for silicon in the form of equilibrium binding energy, volume, bulk modulus, elastic constants, and point defect energies.

6.1 Bond Integrals

The reduced TB parameters entering the energy contributions of the BOP scheme are the same as described in Chapter 3. The data and functions are displayed in Figure 3.2 and the parameter values of the functions representing the reduced TB parameters are given in Table 3.1. The only difference between the parameter values of the BOP for silicon and the reduced TB model for silicon is that we have chosen $p_{\sigma ij}$ such that the binding energy difference between the equilibrium diamond structure and the equilibrium clathrate34 structure is reproduced (see Table 6.3). In addition to the bond integrals, the on-site levels are required which are also identical

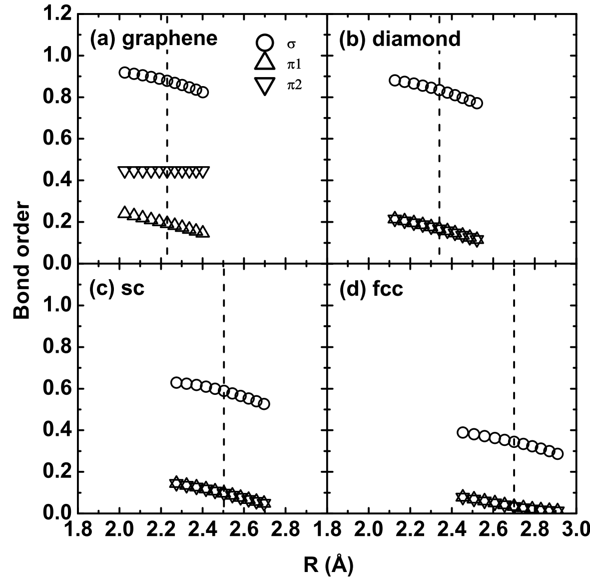

Figure 6.1: σ and π bond orders for a first nearest neighbour bond of silicon in the (a) graphene, (b) diamond, (c) simple cubic (sc), and (d) face centred cubic (fcc) structures as a function of interatomic distance R of the bond-order potential for silicon.

to the on-site levels used in the reduced TB model [186] and the values are given in Table 3.2 in Chapter 3.

Figure 6.1 displays the silicon σ and π bond orders for a first nearest neighbour bond with respect to interatomic distance R in the graphene, diamond, simple cubic (sc), and face centred cubic (fcc) structures, which have coordination numbers of 3, 4, 6, and 12, respectively. Similarly to the reduced TB bond orders for a first nearest neighbour bond of silicon in Figure 3.6, the equilibrium total bond order varies approximately inversely with the coordination number. Furthermore, in addition to a similar behaviour of the total bond order values of the density matrix dependent reduced TB bond orders in Figure 3.6 and the analytically derived BOP bond orders in Figure 6.1, the individual σ and π contributions agree very well.

Table 6.1: Repulsive parameters for silicon-silicon (Si-Si) BOP interactions.

	Si-Si
Φ_0 (eV)	4.653
R_0 (Å)	2.333
R_c (Å)	3.071
n_a	1.000
n_b	7.709
n_c	4.457
R_{tail} (Å)	2.687
R_{cut} (Å)	4.200

6.2 Binding Energy Curves

The repulsive energy contribution (Eq. (2.42)) to the binding energy (Eq. (2.29)) of the BOP for silicon was derived in a similar fashion as the repulsive energy of the reduced TB model for silicon as described in Subsection 2.4.4. Figure 6.2 displays the resulting BOP binding energy curves for different silicon structures in the right-hand panel. For comparison the DFT binding energy curves are shown in the left-hand panel and the reduced TB binding energy curves in the middle panel. The parameters of the repulsive function for the silicon BOP are given in Table 6.1. The Yukawa parameters for the silicon BOP are given in Table 6.2. The repulsive embedding exponent n_d and the shift in the non-magnetic compared to the magnetic reference energy of the free silicon atom ΔU_{atom} are the same for the BOP for silicon and the reduced TB model for silicon and are given in Table 3.4.

6.2.1 DFT binding energy curves

See Subsection 3.2.1 for a discussion of the DFT binding energy curves for silicon.

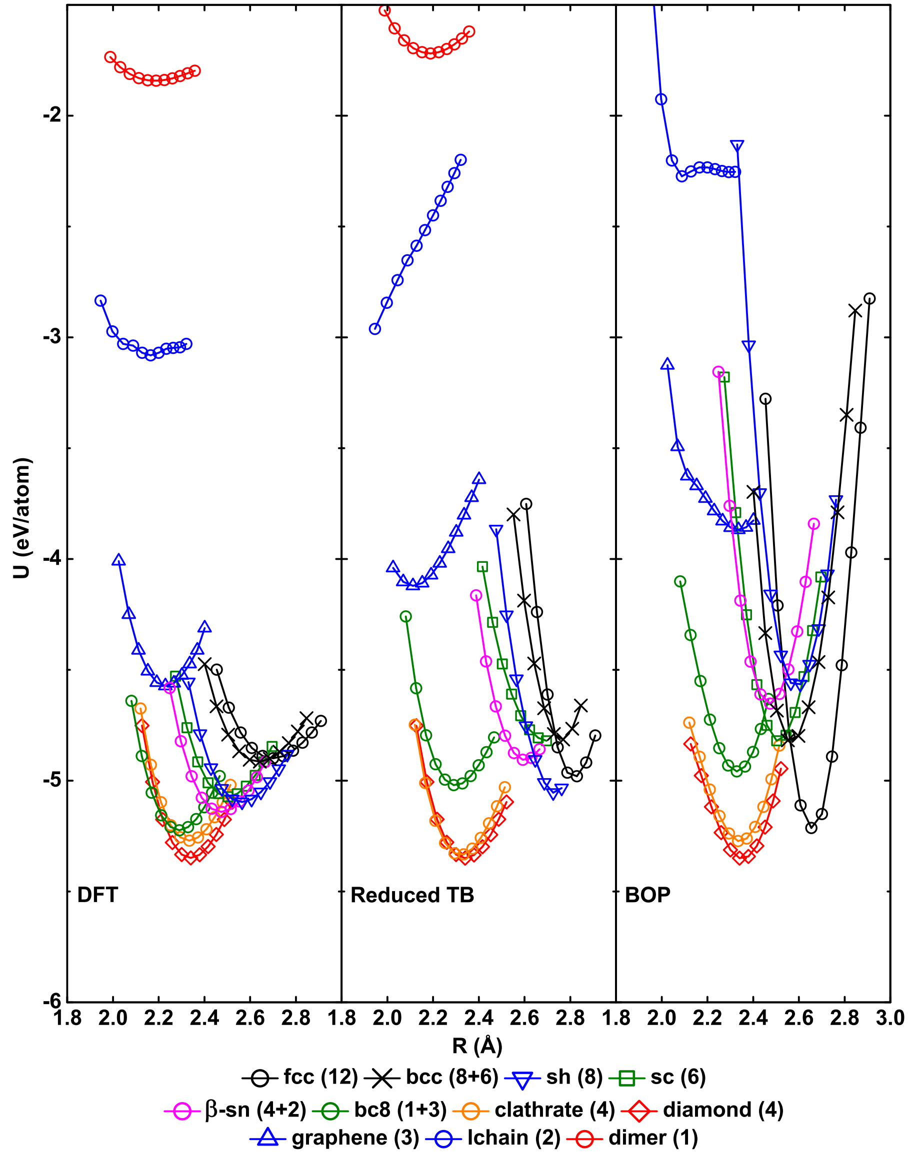

Figure 6.2: DFT, reduced TB, and BOP binding energy curves for different silicon structures as a function of interatomic distance R. DFT and reduced TB binding energy curves are taken from Figure 3.8. The number of nearest neighbours in each structure is given in parentheses.

Table 6.2: Yukawa parameters for silicon-silicon (Si-Si) BOP interactions.

	Si-Si
a_c (eV)	1000.000
b_c	5.000
c_c (1/Å)	0.000
$R_{tail,c}$ (Å)	1.100
$R_{cut,c}$ (Å)	2.120

6.2.2 BOP binding energy curves

Figure 6.2 shows that the diamond structure is predicted to be the ground state structure by the BOP for silicon. Further, similarly to the reduced TB model for silicon, the ordering diamond $\rightarrow$ clathrate $\rightarrow$ bc8 $\rightarrow$ β-Sn predicted by the DFT binding energy data is reproduced by the BOP when considering only these four structures. In contrast to reduced TB and BOP, DFT predicts this ordering in the presence of all other structures considered. The BOP for silicon however predicts the fcc structure to be more stable than the bc8 structure and, in addition, the sc and bcc structures to be more stable than the β-Sn structure. Compared to the reduced TB model, the low coordinated structures dimer, linear chain (lchain), and graphene are less well reproduced by the BOP for silicon. The parameters of the hard core Yukawa potential were chosen such that they do not influence the diamond equilibrium properties, and the effect of the Yukawa potential on the graphene and lchain structures can be seen in the right-hand panel of Figure 6.2. Similarly to the reduced TB model for silicon, the BOP for silicon predicts the close packed structure fcc to be slightly too stable compared to the DFT data. Models that gave lower binding energies for the open structures and higher binding energies for all close packed structures (sc, sh, bcc, and fcc) were also possible, however, in those models the equilibrium binding energies of the close packed structures sc, sh, and bcc were

further away from the DFT values compared to the model presented here. Generally, the lack of the BOP model to describe the close packed structures comparable to DFT is similar to the inability of all orthogonal two-centre TB models with empirical repulsive pair potentials to describe material systems over a large range of coordination. Environment dependent repulsive potentials [205] would increase the complexity of such a model, however, they might also help to improve the overall quality.

While the reduced TB model for silicon predicts that the hexagonal diamond structure is less stable than the cubic diamond structure (by 0.016 eV/atom compared to 0.010 eV/atom for DFT, see Table 3.6), the BOP for silicon is not able to differentiate between these two structures to three decimal places (see Table 6.3). This is not due to the difficulty of fitting the binding energy curves with transferable parameters over such a wide range of co-ordination, but rather due to the fact that the BOP theory when going up to four recursion levels, where the eigenspectrum is approximated by four delta functions, simply cannot differentiate between these two structures. Further silicon structures used as a binding energy benchmark are given in Table 6.3.

6.2.3 Equilibrium properties of diamond ground state

Table 6.4 gives equilibrium properties of silicon diamond for BOP and DFT. The column named BOP shows the results of the BOP for silicon from this study, and the column named DFT shows the results of the DFT calculations performed in this study using LDA, which are the same values as in Table 3.8. Throughout the development process of the BOP for silicon, a positive correlation between the bulk modulus and the elastic constants $C11$ and $C44$ was observed. Trial BOP

Table 6.3: Silicon structures used as a binding energy benchmark. Equilibrium binding energies (eV/atom) are given in parentheses (BOP, DFT).

dimer (1.196, -1.841)	hp7 (-4.187, -4.793)	A6 (-5.158, -4.901)
lchain (-0.905, -3.069)	hp12 (-3.890, -4.795)	Gaoc4 (-4.684, -4.908)
achain45 (-1.356, -3.313)	hr13 (-4.113, -4.803)	C19 (-5.202, -4.909)
achain (-1.304, -3.315)	A15 (-4.369, -4.834)	hp4 (-5.205, -4.909)
zchain90 (-2.048, -3.368)	Ab (-4.468, -4.850)	bcc (-4.837, -4.914)
zchain (-1.235, -3.625)	A13 (-4.815, -4.854)	mp16 (-3.612, -4.922)
A14 (-3.077, -4.248)	tp30 (-4.516, -4.859)	hcp (-5.207, -4.928)
A17 (-2.421, -4.456)	A11 (-4.404, -4.869)	Gamc4 (-4.651, -4.936)
graphene (-3.857, -4.575)	A12 (-2.077, -4.873)	hr22 (-4.448, -4.937)
A9 (-3.857, -4.593)	Ac (-3.615, -4.884)	Uoc4 (-4.355, -4.942)
st12 (-3.722, -4.603)	A10 (-4.396, -4.892)	Ad (-4.096, -4.944)
A8 (-3.846, -4.698)	A7 (-3.985, -4.894)	A20 (-4.287, -4.945)
mp4 (-3.357, -4.778)	fcc (-5.212, -4.899)	Aa (-4.847, -4.951)
st12-W (-3.731, -4.786)	of8 (-4.714, -4.901)	Aaback (-4.846, -4.951)
ci12 (1.472, -4.959)	Ai (-4.499, -5.000)	bct5 (-4.760, -5.065)
sc (-4.813, -5.071)	mc4 (-4.596, -5.075)	sh (-4.582, -5.095)
β-Sn (-4.651, -5.140)	bc8 (-4.954, -5.222)	Clathrate46 (-5.253, -5.262)
Clathrate34 (-5.265, -5.269)	hex. diamond (-5.34**27**, -5.338)	diamond (-5.34**32**, -5.348)

Table 6.4: Equilibrium properties of silicon diamond for BOP and DFT. Equilibrium binding energy (U), equilibrium volume (V), and bulk modulus (B) are obtained from Birch-Murnaghan equation of state fits to binding energies. Units are U (eV/atom), V (Å^3), and B and C (GPa). C_{44}^0 is the static C_{44} elastic constant.

	BOP	DFT	Expt.	BOP[a]
U	-5.343	-5.348	-4.63[b]	-4.63
V	20.194	19.742	20.026[c]	approx. 20[f]
B	124	94	100[c]	92
C'	85	48.5	51[d,e]	32[e]
$C44$	62	76	80[d]	84
$C44^0$	88	106	g	g
$C11$	252	161	166[d]	135
$C12$	82[e]	65[e]	64[d]	71

[a]Reference [30].
[b]Reference [112].
[c]Reference [188].
[d]Reference [190].
[e]Calculated from other elastic constants.
[f]Not available. Read off Figure 3 a).
[g]Not available.

models, which predicted a match of equilibrium binding energy, equilibrium volume, and bulk modulus with DFT comparable to the match of results from the reduced TB model for silicon in Chapter 3 with DFT, unfortunately resulted in negative values for the elastic constant $C44$. A BOP for silicon that gives a reasonable elastic constant $C44$ could only be achieved at the expense of less accurate other equilibrium properties. Nevertheless, even though less accurate than the reduced TB model for silicon in Chapter 3, the BOP for silicon still reproduces the equilibrium binding energy, equilibrium volume, and bulk modulus calculated with DFT fairly well. In addition, the elastic constants are also fairly well reproduced. Overall, the BOP

model for silicon is stiffer than the DFT results for silicon, except for $C44$ and $C44^0$. The same experimental data as in Table 3.8 and results from a BOP for silicon by Gillespie *et al.* [30] are also included for comparison.

We chose the model by Gillespie *et al.*, since it is also based on the BOP theory going up to four recursion levels. The first major difference between the Gillespie *et al.* and our approach is that Gillespie *et al.* fitted to experimental cohesive energies for dimer and diamond, experimental elastic constants $C11$, $C12$, and $C44$ of the diamond structure, and DFT bulk moduli of simple cubic, face centred cubic, and body centred cubic, whereas we only optimised fitting the binding energy curves. The second major difference is that Gillespie *et al.* fitted bond integral as well as repulsive parameters, whereas we only fitted repulsive parameters to binding energies and took the non-repulsive parameters fixed from the reduced TB model for silicon in Chapter 3, which were directly derived from DFT. The effect of the different approaches can be seen by comparing the binding energies of the BOP and DFT columns with the binding energies of the experimental and Gillespie *et al.* columns.

In addition to testing equilibrium properties, we tested the BOP for silicon for point defects. Table 6.5 gives point defect formation energies in silicon calculated with the BOP for silicon. These formation energies are calculated in the same fashion as those for testing the reduced TB models. Similarly to the reduced TB model for silicon, the BOP for silicon gives relatively high energies for the unrelaxed structures. Furthermore, the unrelaxed defect formation energies follow the same energetic ordering tetrahedral $\rightarrow$ vacancy $\rightarrow$ split-(110) $\rightarrow$ hexagonal as predicted by our unrelaxed DFT calculations.

The columns Relaxed (TB) and Relaxed (BOP) give the formation energies calculated with the BOP model for silicon for the with reduced TB relaxed structures

and for the with BOP relaxed structures, respectively. The fact that the reduced TB model predicts an unstable hexagonal defect which relaxes into a tetrahedral defect configuration can be seen by the identical formation energy values, similarly to the identical formation energy values in Table 3.9. Further, the ordering tetrahedral $\rightarrow$ split-(110) $\rightarrow$ vacancy observed with DFT relaxation and with relaxing with reduced TB is reproduced by the static BOP calculations. The BOP silicon relaxed formation energies show the ordering tetrahedral $\rightarrow$ split-(110) $\rightarrow$ vacancy which is identical to DFT, however, the ordering hexagonal $\rightarrow$ split-(110) is reversed compared to DFT (split-(110) $\rightarrow$ hexagonal). Furthermore, relaxation with the BOP for silicon shows a stable hexagonal defect. Overall, the BOP for silicon overestimates the relaxed point defect formation energies relative to DFT.

Table 6.5: Point defect formation energies in silicon diamond (eV). The numbers in parentheses in the top line are the number of atoms per perfect unit cell, whereas the pair of numbers in parentheses in the DFT column from Ref. [191] are LDA and GGA values respectively.

	BOP (128)			DFT (128)		BOP [30] (1536)
	Unrelaxed	Relaxed (TB)	Relaxed (BOP)	Unrelaxed	Relaxed	Relaxed
Vacancy	10.531	8.811	10.241	3.795	3.577	2.759
Split-(110)	11.223	8.636	7.816	4.949	3.340	3.876
Hexagonal	16.641	7.906	7.591	5.961	3.378	3.846
Tetrahedral	8.280	7.906	7.100	3.772	3.339	2.636

6.3 Summary

In this Chapter we presented a bond-based BOP for silicon. This model demonstrates the transferability of the parameters obtained through the projection scheme described in Subsection 2.4.1 across the coarse-graining levels from reduced TB to BOP. The BOP for silicon presented in this Chapter uses the identical input parameters as the reduced TB model presented in Chapter 3. This transferability is demonstrated by the agreement of the density matrix dependent reduced TB bond orders and the analytical BOP bond orders with respect to interatomic distance. Overall, the BOP for silicon reproduces the DFT reference equilibrium properties of the ground state equilibrium diamond structure less well than the reduced TB model for silicon. However, when not considering all structures in the structure database, the ordering of the structures according to their binding energy diamond $\rightarrow$ clathrate $\rightarrow$ bc8 $\rightarrow$ β-Sn and the ordering of the relaxed formation energies tetrahedral $\rightarrow$ split-(110) $\rightarrow$ vacancy are identical to results from DFT calculations.

7 Conclusions and Future Work

The silicon nitride system is of great technological interest and is applied as a bulk as well as a coating material due to its excellent mechanical properties. The existence of a computationally efficient and accurate model that is able to describe the mechanical properties of silicon nitride would allow a more tailored design process of coatings and therefore reduce the experimentation costs. However, no interatomic potential that describes the silicon nitride system robustly exists in the literature.

In this thesis we provide valuable input for the development of an interatomic potential for silicon nitride. We present reduced tight-binding (TB) models for silicon, nitrogen, and silicon nitride and a preliminary bond-based bond-order potential (BOP) for silicon. These models are developed by coarse-graining the electronic structure from density functional theory (DFT) to TB to BOPs. Within this approach the TB bond integrals are obtained directly from DFT projections which thereby reduces the number of overall parameters to be fitted. Furthermore, we show that the reduced TB approximation is not only the theoretical link between the quantum mechanical DFT and the bond-based BOPs, but, in addition, provides a decent description of the silicon nitride system. The binding energies, heats of formation, elastic constants, and defect energies calculated with our reduced TB models are in reasonable agreement with DFT calculations and experimental values.

Furthermore, applying bond-order potential (BOP) theory, a preliminary analytic

interatomic potential for silicon is derived directly from the reduced TB description of the electronic structure. As shown for silicon, the parameters from the reduced TB model are suitable as input for the individual BOP energy contributions. Overall, after fitting a repulsive function to DFT binding energies in a similar fashion as for the reduced TB models, the resulting binding energies, elastic constants, and defect energies are in good agreement with results obtained with DFT and in experimental studies. Even though the BOP for silicon presented here needs further testing and adjustment to be applicable to large scale simulations, we believe that the reduced TB models presented in this thesis will be a valuable foundation on which BOPs for the silicon nitride system can be developed in the future.

In addition to developing the four models mentioned above, we present an improved methodology when going from TB to reduced TB by weighting all four σ TB bond integrals equally in Eqs. (2.73) and (2.74). Further, we show that the quality of the silicon reduced TB model compared to a previously developed reduced TB model for silicon can be improved by choosing one of the reduced TB parameters to be distance invariant.

For the reduced TB models for silicon in Chapter 3, for nitrogen in Chapter 4, and for silicon nitride in Chapter 5 we show that the chosen functions of the individual reduced TB parameters β_σ and β_π reproduce the equilibrium as well as the non equilibrium data very well. Furthermore, the gradients of the bond integral curves are fairly well reproduced by the reduced TB parameters β_σ and β_π. In contrast, the functions for p_σ reproduce only the equilibrium data well, however, the non-equilibrium data as well as the gradients are badly reproduced. We show that taking p_σ as a constant rather than as a function of interatomic distance R has a positive effect on the relative ordering of structures as well as on the properties of the

ground state equilibrium structure for the reduced TB model for silicon. Especially by comparing the results for the properties of the ground state equilibrium diamond structure with the results of an earlier model shows the advantage of this approach.

Furthermore, we show that by going from DFT to projected TB to reduced TB the features of the DOS are qualitatively reproduced. Whereas our current theory guarantees that the total band width is conserved when going from projected TB to reduced TB, the conservation of the valence band width depends on how well reduced TB approximates the individual bond integrals. We have shown that this is better achieved for the binary silicon nitride than for the elemental silicon and nitrogen systems. In addition, the total reduced TB bond orders of the reduced TB models for silicon and nitrogen are inversely proportional to the coordination number of the investigated structure types.

For the reduced TB model for silicon in Chapter 3, fitting a repulsive function to the DFT binding energies leads to a reproduction of the DFT binding energy ordering diamond $\rightarrow$ clathrate $\rightarrow$ bc8 $\rightarrow$ β-Sn. In addition, the diamond structure has the lowest binding energy amongst the structures in our structure database. The reduced TB model for silicon predicts an unstable hexagonal defect which relaxes into a tetrahedral defect configuration. Nevertheless, the energetically defect ordering tetrahedral $\rightarrow$ split-(110) $\rightarrow$ vacancy as predicted by our DFT calculations is reproduced.

The reduced TB model for nitrogen in Chapter 4 predicts the dimer to be the ground state structure and the ordering dimer $\rightarrow$ cg $\rightarrow$ achain $\rightarrow$ zchain predicted by the DFT binding energy data is reproduced by the reduced TB model. Furthermore, the ordering of the close packed structures sh $\rightarrow$ bcc $\rightarrow$ fcc is also reproduced by the reduced TB model.

The reduced TB model for silicon nitride in Chapter 5 demonstrates the transferability between the elemental and binary models as it uses the reduced TB models for silicon and nitrogen from Chapters 3 and 4, respectively, for the elemental interactions without further adjustment. Furthermore, the reduced TB model for silicon nitride predicts the following agreements with DFT results: The β structure is the ground state structure, the ordering of the structures according to their heat of formation values at nearest neighbour distances close to the nearest neighbour distance in the ground state equilibrium β structure and equal composition, namely, $\beta \rightarrow \alpha \rightarrow$ wII, and the ordering of the structures according to their heat of formation values, namely, B3 $\rightarrow$ B4 $\rightarrow$ B1 $\rightarrow$ B2. These agreements in structural ordering with DFT are only adequate when considering these structures only and not all the other structures in the structure database. For example, the reduced TB model for silicon nitride only poorly describes the γ structure. Whereas the γ structure is the third lowest structure according to DFT heat of formation values, the reduced TB model allowing charge transfer (CT) predicts the heat of formation value to be more than 1eV/atom too large. Furthermore, even though we observe charge transfer in our calculations with the reduced TB CT model that is comparable to other DFT studies, an advantage of the reduced TB CT model over the reduced TB model enforcing local charge neutrality (LCN) with respect to the energetically ordering and thermodynamic stability of different structures is not observable. We also find that the fitting of the repulsive energy to reference binding energies has a large influence on the quality of the final reduced TB models.

Whereas the reduced TB model for silicon nitride shows the transferability of the elemental interactions from one environment to another, the BOP for silicon in Chapter 6 shows good transferability across the coarse-graining levels by employing

the identical parameters as the reduced TB model as input. The transferability from reduced TB to BOP can especially be seen when comparing the density matrix dependent reduced TB bond orders with the results of the analytical BOP bond orders. Even though the BOP for silicon does not reproduce the properties of the ground state equilibrium diamond structure obtained with DFT as good as the reduced TB model for silicon, the diamond structure is still predicted to be the ground state structure, and, in addition, the ordering of the structures according to their binding energy diamond $\rightarrow$ clathrate $\rightarrow$ bc8 $\rightarrow$ β-Sn is reproduced. Furthermore, the unrelaxed defect formation energies follow the same energetic ordering tetrahedral $\rightarrow$ vacancy $\rightarrow$ split-(110) $\rightarrow$ hexagonal as predicted by our unrelaxed DFT calculations, and the relaxed formation energies show the ordering tetrahedral $\rightarrow$ split-(110) $\rightarrow$ vacancy which is identical to DFT.

Possible future work may include the application of the four models presented in this thesis to large scale simulations. Two possible applications could be the investigation of amorphous structures as well as the investigation of crack propagation with respect to brittle or ductile behaviour. Another application to test the robustness of the reduced TB model for silicon nitride could be to investigate composition dependent structures resulting from deposition simulations. Furthermore, the model development methodology and the models presented here could be used to assist further model development for reduced TB models for carbon, silicon carbide, as well as BOPs for nitrogen, silicon nitride, carbon, and silicon carbide. New bond-based BOPs for silicon nitride and silicon carbide could improve the theoretical description of growth. For example, these models could help to explain the effect of process temperature and pressure on the morphology of the deposited films. In addition, by using the same parameters for elemental interactions in different

environments, ternary systems from combinations of silicon nitride, silicon carbide, titanium nitride, and titanium carbide could be developed combining this work with the work by Kamenski [164] and Margine *et al.* [165].

References

[1] H. Hauser. Ceramics in engines past - present - future. *Thermochim. Acta*, 112:1–11, 1987.

[2] C. Juang, J. H. Chang, and R. Y. Hwang. Properties of very low temperature plasma deposited silicon nitride films. *J. Vac. Sci. Technol. B*, 10(3):1221–1223, 1992.

[3] E. Kroke and M. Schwarz. Novel group 14 nitrides. *Coordin. Chem. Rev.*, 248:493–532, 2004.

[4] A. Kailer. Werkzeuge und Komponenten aus Hochleistungskeramik. *Konstruktion - Zeitschrift für Produktentwicklung und Ingenieur-Werkstoffe*, 7-8:IW8–9, 2010.

[5] F. L. Riley. Silicon nitride and related materials. *J. Am. Ceram. Soc.*, 83:245–265, 2000.

[6] S. Hampshire. Silicon nitride ceramics – Review of structure, processing and properties. *Journal of Achievements in Materials and Manufacturing Engineering*, 24:43–50, 2007.

[7] R. C. Buchanan, editor. *Ceramic Materials for Electronics*. Marcel Dekker, Inc., 3rd edition, 2004.

[8] R.-H. Ma, P.-C. Chou, Y.-H. Wang, T.-H. Hsueh, L.-M. Fu, and C.-Y. Lee. A microcantilever-based gas flow sensor for flow rate and direction detection. *Microsyst. Technol.*, 15:1201–1205, 2009.

[9] W. van Gelder and V. E. Hauser. The etching of silicon nitride in phosphoric acid with silicon dioxide as a mask. *J. Electrochem. Soc.*, 114(8):869–872, 1967.

[10] A. Piccirillo and A. L. Gobbi. Physical-electrical properties of silicon nitride deposited by PECVD on III-V semiconductors. *J. Electrochem. Soc.*, 137:3910–3917, 1990.

[11] H. O. Pierson. *Handbook of chemical vapor deposition (CVD): principles, technology, and applications*. William Andrew, 1992.

[12] C. Uslu, B. Park, and D. B. Poker. Synthesis of metastable carbon-silicon-nitrogen compounds by ion implantation. *J. Electron. Mater.*, 25:23–26, 1996.

[13] M. Lattemann, S. Ulrich, H. Holleck, M. Stüber, and H. Leiste. Characterisation of silicon carbide and silicon nitride thin films and Si_3N_4/SiC multilayers. *Diam. Relat. Mater.*, 11:1248–1253, 2002.

[14] D. Pakula, L. A. Dobrzanskia, K. Golombek, M. Pancielejko, and A. Kriz. Structure and properties of the Si_3N_4 nitride ceramics with hard wear resistant coatings. *J. Mater. Process. Tech.*, 157–158:388–393, 2004.

[15] J. Robertson. The electronic properties of silicon nitride. *Philos. Mag. B*, 44(2):215–237, 1981.

[16] J. Robertson and M. J. Powell. Gap states in silicon nitride. *Appl. Phys. Lett.*, 44(4):415–417, 1984.

[17] J. Robertson. Electronic structure of silicon nitride. *Philos. Mag. B*, 63:47–77, 1991.

[18] J. Robertson. Defects and hydrogen in amorphous silicon nitride. *Philos. Mag. B*, 69(2):307–326, 1994.

[19] J. Robertson, W. L. Warren, and J. Kanicki. Nature of the Si and N dangling bonds in silicon-nitride. *J. Non-Cryst. Solids*, 187:297–300, 1995.

[20] J. Tersoff. New empirical model for the structural properties of silicon. *Phys. Rev. Lett.*, 56:632–635, 1986.

[21] P. Vashishta, R. K. Kalia, J. P. Rino, and I. Ebbsjö. Interaction potential for SiO_2: A molecular-dynamics study of structural correlations. *Phys. Rev. B*, 41:12197–12209, 1990.

[22] R. Belkada, T. Shibayanagi, M. Naka, and M. Kohyama. *Ab initio* calculations of the atomic and electronic structure of β-silicon nitride. *J. Am. Ceram. Soc.*, 83(10):2449–2454, 2000.

[23] W. Y. Ching, Lizhi Ouyang, and Julian D. Gale. Full *ab initio* geometry optimization of all known crystalline phases of Si_3N_4. *Phys. Rev. B*, 61:8696–8700, 2000.

[24] R. Belkada, M. Kohyama, T. Shibayanagi, and M. Naka. Relative stability of $P6_3/m$ and $P6_3$ structures of β-Si_3N_4. *Phys. Rev. B*, 65:092104, 2002.

[25] A. Togo and P. Kroll. First-principles lattice dynamics calculations of the phase boundary between β-Si_3N_4 and γ-Si_3N_4 at elevated temperatures and pressures. *J. Comput. Chem.*, 29:2255–2259, 2008.

[26] T. Watts. Properties of silicon nitride - an *ab initio* study of the crystalline phases and amorphous silicon-nitrogen alloys. Diplomarbeit, Universität Wien, 2011.

[27] R. Drautz, X. W. Zhou, D. A. Murdick, B. Gillespie, H. N. G. Wadley, and D. G. Pettifor. Analytic bond-order potentials for modelling the growth of semiconductor thin films. *Prog. Mater. Sci.*, 52:196–229, 2007.

[28] Ralf Drautz and D. G. Pettifor. Valence-dependent analytic bond-order potential for magnetic transition metals. *Phys. Rev. B*, 84:214114, 2011.

[29] D. A. Murdick, X. W. Zhou, H. N. G. Wadley, D. Nguyen-Manh, R. Drautz, and D. G. Pettifor. Analytic bond-order potential for the gallium arsenide system. *Phys. Rev. B*, 73:045206–1–20, 2006.

[30] B. A. Gillespie, X. W. Zhou, D. A. Murdick, H. N. G. Wadley, R. Drautz, and D. G. Pettifor. Bond-order potential for silicon. *Phys. Rev. B*, 75:155207–1–10, 2007.

[31] A. Urban, M. Reese, M. Mrovec, C. Elsässer, and B. Meyer. Parameterization of tight-binding models from density functional theory calculations. *Phys. Rev. B*, 84:155119, 2011.

[32] Georg K. H. Madsen, Eunan J. McEniry, and Ralf Drautz. Optimized orthogonal tight-binding basis: Application to iron. *Phys. Rev. B*, 83:184119, 2011.

[33] D. G. Pettifor. *Bonding and Structure of Molecules and Solids.* Oxford Science Publications, 2002.

[34] M. Elstner, D. Porezag, G. Jungnickel, J. Elsner, M. Haugk, Th. Frauenheim, S. Suhai, and G. Seifert. Self-consistent-charge density-functional tight-binding method for simulations of complex materials properties. *Phys. Rev. B*, 58:7260–7268, 1998.

[35] X. Ma, C. Li, F. Wang, and W. Zhang. Thermodynamic assessment of the Si–N system. *CALPHAD - Computer Coupling of Phase Diagrams and Thermochemistry*, 27:383–388, 2003.

[36] David A. Young. *Phase diagrams of the elements.* University of California Press, 1991.

[37] C. Mailhiot, L. H. Yang, and A. K. McMahan. Polymeric nitrogen. *Phys. Rev. B*, 46:14419–14435, 1992.

[38] H. Okamoto. N-Si (nitrogen-silicon). *J. Phase Equilib. Diffus.*, 26:293–294, 2005.

[39] E. T. Turkdogan, P. M. Bills, and V. A. Tippett. Silicon nitrides: Some physico-chemical properties. *J. Appl. Chem.*, 8:296–302, 1958.

[40] R. Grün. The crystal structure of β-Si_3N_4; structural and stability considerations between α- and β-Si_3N_4. *Acta Cryst.*, B35:800–804, 1979.

[41] J. Liang, L. Topor, A. Navrotsky, and M. Mitomo. Silicon nitride: Enthalpy of formation of the α- and β-polymorphs and the effect of C and O impurities. *J. Mater. Res.*, 14:1959–1968, 1999.

[42] R. S. Bradley, D. C. Munro, and M. Whitfield. The reactivity and polymorphism of selected nitrides at high temperatures and high pressures. *J. Inorg. Nucl. Chem.*, 28:1803–1812, 1966.

[43] R. Pompe. A thermoanalytical study of the alpha and beta forms of silicon nitride. *Thermochim. Acta*, 27(1-3):155 – 163, 1978.

[44] P. Sajgalik and D. Galusek. α/β phase transformation of silicon nitride: homogeneous and heterogeneous nucleation. *J. Mater. Sci. Lett.*, 12:1937–1939, 1993.

[45] K. H. Jack. Review sialons and related nitrogen ceramics. *J. Mater. Sci.*, 11:1135–1158, 1976.

[46] C.-M. Wang, X. Pan, M. Rühle, F. L. Riley, and M. Mitomo. Review silicon nitride crystal structure and observations of lattice defects. *J. Mater. Sci.*, 31:5281–5298, 1996.

[47] A. Zerr, G. Miehe, G. Serghiou, M. Schwarz, E. Kroke, R. Riedel, H. Fueß, P. Kroll, and R. Boehler. Synthesis of cubic silicon nitride. *Nature*, 400:340–342, 1999.

[48] P. Kroll. Pathways to metastable nitride structures. *J. Solid. State. Chem.*, 176:530–537, 2003.

[49] X. Qiu and E. Gyarmati. Composition and properties of SiN_X films produced by reactive r.f. magnetron sputtering. *Thin Solid Films*, 151:223–233, 1987.

[50] P. E. Tomaszewski. Jan Czochralski - father of the Czochralski method. *J. Cryst. Growth.*, 236:1–4, 2002.

[51] T. Itoh. Preparation of pure α-silicon nitride from silicon powder. *J. Mater. Sci. Lett.*, 9:19–20, 1990.

[52] T. Licko, V. Figusch, and J. Puchyova. Synthesis of silicon nitride by carbothermal reduction and nitriding of silica: Control of kinetics and morphology. *J. Eur. Ceram. Soc.*, 9:219–230, 1992.

[53] F. K. van Dijen, A. Kerber, U. Vogt, W. Pfeifer, and M. Schulze. A comparative study of three silicon nitride powders, obtained by three different syntheses. *Key. Eng. Mat.*, 89-91:19–28, 1994.

[54] A. Atkinson, P. J. Leatt, A. J. Moulson, and E. W. Roberts. A mechanism for the nitridation of silicon powder compacts. *J. Mater. Sci.*, 9:981–984, 1974.

[55] G. R. Terwilliger. Properties of sintered Si_3N_4. *J. Am. Ceram. Soc.*, 57(1):48–49, 1974.

[56] G. R. Terwilliger and F. F. Lange. Pressureless sintering of Si_3N_4. *J. Mater. Sci.*, 10:1169–1174, 1975.

[57] A. Giachello, P. C. Martinengo, G. Tommasini, and P. Popper. Sintering of silicon nitride in a powder bed. *J. Mater. Sci.*, 14:2825–2830, 1979.

[58] K. Niihara and T. Hirai. Chemical vapour-deposited silicon nitride. *J. Mater. Sci.*, 12:1233–1242, 1977.

[59] M. Diserens, J. Patscheider, and F. Lévy. Improving the properties of titanium nitride by incorporation of silicon. *Surf. Coat. Tech.*, 108–109:241–246, 1998.

[60] Y. Suda, K. Ebihara, K. Baba, H. Abe, and A. M. Grishin. Crystalline silicon nitride thin films grown by pulsed YAG laser deposition. *Nanostruct. Mater.*, 12:391–394, 1999.

[61] E. Kroke, Y.-L. Li, C. Konetschny, E. Lecomte, C. Fasel, and R. Riedel. Silazane derived ceramics and related materials. *Mat. Sci. Eng. R.*, 26:97–199, 2000.

[62] T. Otani and M. Hirata. High rate deposition of silicon nitride films by APCVD. *Thin Solid Films*, 442:44–47, 2003.

[63] A. Markwitz, H. Baumann, E. F. Krimmel, M. Rose, K. Bethge, P. Misaelides, and S. Logothetidis. Nitrogen profiles of thin sputtered PVD silicon nitride films. *Vacuum*, 44(3/4):367–370, 1993.

[64] K. F. Roenigk and K. F. Jensen. Low pressure CVD of silicon nitride. *J. Electrochem. Soc.*, 134(7):1777–1785, 1987.

[65] T. Hiraj and S. Hayashi. Synthesis of β-Si_3N_4 by chemical vapor deposition. *Communications of the American Ceramic Society*, pages C–88–89, 1981.

[66] W. Posadowski. Properties of silicon nitride thin films obtained by reactive sputtering. *Thin Solid Films*, 69:149–155, 1980.

[67] M. Bielawski and D. Seo. Residual stress development in UMS TiN coatings. *Surf. Coat. Tech.*, 200:1476–1482, 2005.

[68] S. K. Patra and G. Mohan Rao. Studies on structural and electrical properties of silicon nitride films deposited by unbalanced magnetron sputter deposition. *Mater. Sci. Eng.*, B90:90–98, 2002.

[69] J. H. Kim and K. W. Chung. Microstructure and properties of silicon nitride thin films deposited by reactive bias magnetron sputtering. *J. Appl. Phys.*, 83:5831–5839, 1998.

[70] Prof. Dr.-Ing. Jörg Müller. Halbleitertechnologie. Lecture Notes at Technische Universität Hamburg-Harburg, 2007.

[71] P. F. Becher, E. Y. Sun, K. P. Plucknett, K. B. Alexander, C.-H. Hsueh, H.-T. Lin, S. B. Waters, and C. G. Westmoreland. Microstructural design of silicon nitride with improved fracture toughness: I effects of grain shape and size. *J. Am. Ceram. Soc.*, 81:2821–2830, 1998.

[72] R. W. Rice. *Mechanical Properties of Ceramics and Composites - Grain and Particel Effects*. Marcel Dekker, Inc., 2000.

[73] R. M. Fulrath and J. A. Pask, editors. *Ceramic Microstructures '76*. Westview Press, 1976.

[74] R. W. Trice and J. W. Halloran. Mode I fracture toughness of a small-grained silicon nitride: Orientation, temperature, and crack length effects. *J. Am. Ceram. Soc.*, 82:2633–2640, 1999.

[75] A. K. Mukhopadhyay, S. K. Datta, and D. Chakraborty. On the microhardness of silicon nitride and sialon ceramics. *J. Eur. Ceram. Soc.*, 6:303–311, 1990.

[76] I. Tanaka, F. Oba, T. Sekine, E. Ito, A. Kubo, K. Tatsumi, H. Adachi, and T. Yamamoto. Hardness of cubic silicon nitride. *J. Mater. Res.*, 17:731–733, 2002.

[77] M. Parlinska-Wojtan, S. Meier, and J. Patscheider. Transmission electron microscopy characterization of TiN/SiN_X multilayered coatings plastically deformed by nanoindentation. *Thin Solid Films*, 518:4890–4897, 2010.

[78] C. H. Pan. A novel method for determining young's modulus of thin films by micro-strain gauges. *Microsyst. Technol.*, 11:151–157, 2005.

[79] V. Ziebart, O. Paul, U. Münch, J. Schwizer, and H. Baltes. Mechanical properties of thin films from the load deflection of long clamped plates. *J. Microelectromech. S.*, 7:320–328, 1998.

[80] U. Beck, D. T. Smith, G. Reiners, and S. J. Dapkunas. Mechanical properties of SiO_2 and Si_3N_4 coatings: a BAM/NIST co-operative project. *Thin Solid Films*, 332:164–171, 1998.

[81] T.-Y. Zhang, Y.-J. Su, C.-F. Qian, M.-H. Zhao, and L.-Q. Chen. Microbridge testing of silicon nitride thin films deposited on silicon wafers. *Acta Mater.*, 48:2843–2857, 2000.

[82] S. J. Bull. Nanoindentation of coatings. *J. Phys. D: Appl. Phys.*, 38:R393–R413, 2005.

[83] S. Veprek and S. Reiprich. A concept for the design of novel superhard coatings. *Thin Solid Films*, 268(1-2):64–71, 1995.

[84] S. Veprek, M. G. J. Veprek-Heijman, P. Karvankova, and J. Prochazka. Different approaches to superhard coatings and nanocomposites. *Thin Solid Films*, 476(1):1–29, 2005.

[85] S. Veprek. The search for novel, superhard materials. *J. Vac. Sci. Technol. A*, 17(5):2401–2420, 1999.

[86] L. Shizhi, S. Yulong, and P. Hongrui. Ti-Si-N films prepared by plasma-enhanced chemical vapor deposition. *Plasma. Chem. Plasma. P.*, 12(3):287–297, 1992.

[87] A. Niederhofer, T. Bolom, P. Nesladek, K. Moto, C. Eggs, D. S. Patil, and S. Veprek. The role of percolation threshold for the control of the hardness and thermal stability of super- and ultrahard nanocomposites. *Surf. Coat. Tech.*, 146-147:183–188, 2001.

[88] R. F. Zhang and S. Veprek. On the spinodal nature of the phase segregation and formation of stable nanostructure in the Ti–Si–N system. *Mat. Sci. Eng. A*, 424:128–137, 2006.

[89] J. M. Cairney, M. J. Hoffman, P. R. Munroe, P. J. Martin, and A. Bendavid. Deformation and fracture of Ti–Si–N nanocomposite films. *Thin Solid Films*, 479:193–200, 2005.

[90] S. Veprek, A. Niederhofer, K. Moto, T. Bolom, H.-D. Männling, P. Nesladek, G. Dollinger, and A. Bergmaier. Composition, nanostructure and origin of the ultrahardness in nc-TiN/a-Si_3N_4/a- and nc-$TiSi_2$ nanocomposites with H_V = 80 to $\geq$ 105 GPa. *Surf. Coat. Tech.*, 133-134:152–159, 2000.

[91] H. Söderberg, M. Oden, T. Larsson, L. Hultman, and J. M. Molina-Aldareguia. Epitaxial stabilization of cubic-SiN_X in TiN/SiN_X multilayers. *Appl. Phys. Lett.*, 88:191902–1–3, 2006.

[92] H. Holleck and V. Schier. Multilayer PVD coatings for wear protection. *Surf. Coat. Tech.*, 76-77:328–336, 1995.

[93] S. Hao, B. Delley, S. Veprek, and C. Stampfl. Superhard nitride-based nanocomposites: Role of interfaces and effect of impurities. *Phys. Rev. Lett.*, 97:086102–1–4, 2006.

[94] R. F. Zhang, A. S. Argon, and S. Veprek. Understanding why the thinnest SiN_X interface in transition-metal nitrides is stronger than the ideal bulk crystal. *Phys. Rev. B*, 81:245418–1–7, 2010.

[95] A. Nakano, R. K. Kalia, and P. Vashishta. Dynamics and morphology of brittle cracks: A molecular-dynamics study of silicon nitride. *Phys. Rev. Lett.*, 75:3138–3141, 1995.

[96] R. K. Kalia, A. Nakano, A. Omeltchenko, K. Tsuruta, and P. Vashishta. Role of ultrafine microstructures in dynamic fracture in nanophase silicon nitride. *Phys. Rev. Lett.*, 78:2144–2147, 1997.

[97] M. E. Bachlechner, A. Omeltchenko, A. Nakano, R. K. Kalia, P. Vashishta, I. Ebbsjö, and A. Madhukar. Dislocation emission at the silicon/silicon nitride interface: A million atom molecular dynamics simulation on parallel computers. *Phys. Rev. Lett.*, 84:322–325, 2000.

[98] Shigenobu Ogata, Hiroshi Kitagawa, Naoto Hirosaki, Yoshinari Hatanaka, and Takashi Umezu. Molecular dynamics simulation of shearing deformation process of silicon nitride single crystal. *Comp. Mater. Sci.*, 23:146 – 154, 2002.

[99] P. Walsh, A. Omeltchenko, R. K. Kalia, A. Nakano, and P. Vashishta. Nanoindentation of silicon nitride: A multimillion-atom molecular dynamics study. *Appl. Phys. Lett.*, 82:118–120, 2003.

[100] R. K. Kalia, A. Nakano, K. Tsuruta, and P. Vashishta. Morphology of pores and interfaces and mechanical behavior of nanocluster-assembled silicon nitride ceramic. *Phys. Rev. Lett.*, 78:689–692, 1997.

[101] R. K. Kalia, A. Nakano, P. Vashishta, C. L. Rountree, L. Van Brutzel, and S. Ogata. Multiresolution atomistic simulations of dynamic fracture in nanostructured ceramics and glasses. *Int. J. Fracture*, 121:71–79, 2003.

[102] X.-Y. Guo and P. Brault. Early stages of silicon nitride film growth studied by molecular dynamics simulations. *Surf. Sci.*, 488:133–140, 2001.

[103] F. Gou, M.A. Gleeson, A.W. Kleyn, R.W.E. van de Kruijs, A.E. Yakshin, and F. Bijkerk. Growth of silicon nitride films by bombarding amorphous silicon with N+ ions: MD simulation. *Nucl. Instrum. Meth. B*, 267(18):3245 – 3248, 2009.

[104] F. de Brito Mota, J. F. Justo, and A. Fazzio. Structural properties of amorphous silicon nitride. *Phys. Rev. B*, 58:8323–8328, 1998.

[105] A. C. T. van Duin, S. Dasgupta, F. Lorant, and W. A. Goddard. ReaxFF: A reactive force field for hydrocarbons. *J. Phys. Chem. A*, 105:9396–9409, 2001.

[106] G. C. Abell. Empirical chemical pseudopotential theory of molecular and metallic bonding. *Phys. Rev. B*, 31:6184–6196, 1985.

[107] J. Tersoff. Empirical interatomic potential for carbon, with applications to amorphous carbon. *Phys. Rev. Lett.*, 61:2879–2882, 1988.

[108] J. Tersoff. Empirical interatomic potential for silicon with improved elastic properties. *Phys. Rev. B*, 38:9902–9905, 1988.

[109] J. Tersoff. New empirical approach for the structure and energy of covalent systems. *Phys. Rev. B*, 37:6991–7000, 1988.

[110] J. Tersoff. Modeling solid-state chemistry: Interatomic potentials for multicomponent systems. *Phys. Rev. B*, 39:5566–5568, 1989.

[111] P. C. Kelires and J. Tersoff. Equilibrium alloy properties by direct simulation: Oscillatory segregation at the Si-Ge(100) 2 x 1 surface. *Phys. Rev. Lett.*, 63:1164–1167, 1989.

[112] H. Balamane, T. Halicioglu, and W. A. Tiller. Comparative study of silicon empirical interatomic potentials. *Phys. Rev. B*, 46:2250–2279, 1992.

[113] D. W. Brenner. Empirical potential for hydrocarbon for use in simulating the chemical vapor deposition of diamond films. *Phys. Rev. B*, 42:9458–9471, 1990.

[114] F. De Brito Mota, J. F. Justo, and A. Fazzio. Structural and electronic properties of silicon nitride materials. *Int. J. Quantum Chem.*, 70(4-5):973–980, 1998.

[115] F. de Brito Mota, J. F. Justo, and A. Fazzio. Hydrogen role on the properties of amorphous silicon nitride. *J. Appl. Phys.*, 86:1843–1847, 1999.

[116] J. Houska, J. E. Klemberg-Sapieha, and L. Martinu. Atom-by-atom simulations of chemical vapor deposition of nanoporous hydrogenated silicon nitride. *J. Appl. Phys.*, 107(8):083501, 2010.

[117] A.-P. Prskalo, S. Schmauder, C. Ziebert, J. Ye, and S. Ulrich. Molecular dynamics simulations of the sputtering of SiC and Si_3N_4. *Surf. Coat. Tech.*, 204:2081 – 2084, 2010.

[118] K. Albe, W. Möller, and K.-H. Heinig. Computer simulation and boron nitride. *Radiat. Eff. Defect. S.*, 141:85–97, 1997.

[119] K. H. Park, B. C. Kim, and H. Kang. Silicon nitride formation by low energy N^+ and N_2^+ ion beams. *J. Chem. Phys.*, 97(4):2742–2749, 1992.

[120] I. Kusunoki, T. Takaoka, Y. Igari, and K. Ohtsuka. Nitridation of a Si(100) surface by 100–1000 eV N_2^+ ion beams. *J. Chem. Phys.*, 101(9):8238–8245, 1994.

[121] Frank H. Stillinger and Thomas A. Weber. Computer simulation of local order in condensed phases of silicon. *Phys. Rev. B*, 31:5262–5271, 1985.

[122] P. Vashishta, R. K. Kalia, A. N. Weili, and I. Ebbsjö. Molecular dynamics methods and large-scale simulations of amorphous materials. *NATO ASI SERIES 3 HIGH TECHNOLOGY*, 23:151–213, 1996.

[123] C.-K. Loong, P. Vashishta, R. K. Kalia, and I. Ebbsjö. Crystal structure and phonon density of states of high-temperature ceramic silicon nitride. *Europhys. Lett.*, 31(4):201, 1995.

[124] P. Vashishta, A. Nakano, R. K. Kalia, and I. Ebbsjö. Molecular dynamics simulations of covalent amorphous insulators on parallel computers. *J. Non-Cryst. Solids*, 182:59 – 67, 1995.

[125] P. Vashishta, R. K. Kalia, and I. Ebbsjö. Low-energy floppy modes in high-temperature ceramics. *Phys. Rev. Lett.*, 75:858–861, 1995.

[126] K. Tsuruta, A. Omeltchenko, R. K. Kalia, and P. Vashishta. Early stages of sintering of silicon nitride nanoclusters: a molecular-dynamics study on parallel machines. *Europhys. Lett.*, 33:441–446, 1996.

[127] M. E. Bachlechner, A. Omeltchenko, A. Nakano, R. K. Kalia, P. Vashishta, I. Ebbsjö, A. Madhukar, and P. Messina. Multimillion-atom molecular dynamics simulation of atomic level stresses in Si(111)/Si_3N_4(0001) nanopixels. *Appl. Phys. Lett.*, 72(16):1969–1971, 1998.

[128] D. Beysens, C. M. Knobler, and H. Schaffar. Scaling in the growth of aggregates on a surface. *Phys. Rev. B*, 41(14):9814–9818, 1990.

[129] G. H. Gilmer, H. Huang, and C. Roland. Thin film deposition: fundamentals and modeling. *Comp. Mater. Sci.*, 12:354–380, 1998.

[130] A. C. T. van Duin, A. Strachan, S. Stewman, Q. Zhang, X. Xu, and W. A. Goddard. $ReaxFF_{SiO}$ reactive force field for silicon and silicon oxide systems. *J. Phys. Chem. A*, 107:3803–3811, 2003.

[131] A. van Duin. ReaxFF user manual, 2002.

[132] T. S. Hudson, D. Nguyen-Manh, A. C. T. van Duin, and A. P. Sutton. Grand canonical Monte Carlo simulations of intergranular glassy films in β silicon nitride. *Mat. Sci. Eng. A*, 422:123–135, 2006.

[133] D. G. Pettifor. New many-body potential for the bond order. *Phys. Rev. Lett.*, 63:2480–2483, 1989.

[134] D. G. Pettifor and I. I. Oleinik. Analytic bond-order potentials beyond Tersoff-Brenner. I. Theory. *Phys. Rev. B*, 59:8487–8499, 1999.

[135] I. I. Oleinik and D. G. Pettifor. Analytic bond-order potentials beyond Tersoff-Brenner. II. Application to the hydrocarbons. *Phys. Rev. B*, 59:8500–8507, 1999.

[136] D. G. Pettifor and I. I. Oleinik. Bounded analytic bond-order potentials for σ and π bonds. *Phys. Rev. Lett.*, 84:4124–4127, 2000.

[137] M. Mrovec, M. Moseler, C. Elsässer, and P. Gumbsch. Atomistic modeling of hydrocarbon systems using analytic bond-order potentials. *Prog. Mater. Sci.*, 52:230–254, 2007.

[138] B.A. Gillespie and H.N.G. Wadley. Atomistic examinations of the solid-phase epitaxial growth of silicon. *J. Cryst. Growth*, 311(11):3195 – 3203, 2009.

[139] D. A. Murdick, H. N. G. Wadley, and X. W. Zhou. Condensation mechanisms of an arsenic-rich vapor on GaAs (001) surfaces. *Phys. Rev. B*, 75(12):125318, 2007.

[140] P. C. Zalm, G. F. A. van de Walle, D. J. Gravesteijn, and A. A. van Gorkum. Ge segregation at Si/$Si_{1-X}Ge_X$ interfaces grown by molecular beam epitaxy. *Appl. Phys. Lett.*, 55(24):2520–2522, 1989.

[141] M. Pristovsek, S. Tsukamoto, A. Ohtake, N. Koguchi, B. G. Orr, W. G. Schmidt, and J. Bernholc. Gallium-rich reconstructions on GaAs(001). *Phys. Status Solidi B*, 240(1):91–98, 2003.

[142] J. R. Arthur. Interaction of Ga and As_2 molecular beams with GaAs surfaces. *J. Appl. Phys.*, 39(8):4032–4034, 1968.

[143] J. R. Arthur. Surface stoichiometry and structure of GaAs. *Surf. Sci.*, 43(2):449 – 461, 1974.

[144] E. S. Tok, J. H. Neave, J. Zhang, B. A. Joyce, and T. S. Jones. Arsenic incorporation kinetics in GaAs(001) homoepitaxy revisited. *Surf. Sci.*, 374(1-3):397 – 405, 1997.

[145] A. F. Voter. Hyperdynamics: Accelerated molecular dynamics of infrequent events. *Phys. Rev. Lett.*, 78(20):3908–3911, 1997.

[146] A. F. Voter. A method for accelerating the molecular dynamics simulation of infrequent events. *J. Chem. Phys.*, 106(11):4665–4677, 1997.

[147] A. F. Voter. Parallel replica method for dynamics of infrequent events. *Phys. Rev. B*, 57(22):R13985–R13988, 1998.

[148] A. F. Voter, F. Montalenti, and T. C. Germann. Extending the time scale in atomistic simulation of materials. *Annu. Rev. Mater. Res.*, 32:321–346, 2002.

[149] Graeme Henkelman and Hannes Jónsson. Long time scale kinetic Monte Carlo simulations without lattice approximation and predefined event table. *J. Chem. Phys.*, 115(21):9657–9666, 2001.

[150] P. Hohenberg and W. Kohn. Inhomogeneous electron gas. *Phys. Rev.*, 136:B864–B871, 1964.

[151] W. Kohn and L. J. Sham. Self-consistent equations including exchange and correlation effects. *Phys. Rev.*, 140:1133–1138, 1965.

[152] J. P. Perdew and W. Yue. Accurate and simple density functional for the electronic exchange energy: Generalized gradient approximation. *Phys. Rev. B*, 33:8800–8802, 1986.

[153] Richard M. Martin. *Electronic Structure: Basic Theory and Practical Methods.* Cambridge University Press, 2004.

[154] Mike Finnis. *Interatomic forces in condensed matter.* Oxford series on materials modelling, 2010.

[155] J. C. Slater and G. F. Koster. Simplified LCAO method for the periodic potential problem. *Phys. Rev.*, 94:1498–1524, 1954.

[156] F. Ducastelle and F. Cyrot-Lackmann. Moments developments and their application to the electronic charge distribution of d bands. *J. Phys. Chem. Solids*, 31:1295–1306, 1970.

[157] F. Cyrot-Lackmann. On the electronic structure of liquid transitional metals. *Adv. Phys.*, 16:393–400, 1967.

[158] R. Haydock, V. Heine, and M. J. Kelly. Electronic structure based on the local atomic environment for tight-binding bands: II. *J. Phys. C. Solid. State.*, 8:2591–2605, 1975.

[159] C. Lanczos. An iteration method for the solution of the eigenvalue problem of linear differential and integral operators. *J. Res. Nat. Bur. Stand.*, 45:255–282, 1950.

[160] A. P. Horsfield, A. M. Bratkovsky, M. Fearn, D. G. Pettifor, and M. Aoki. Bond-order potentials: Theory and implementation. *Phys. Rev. B*, 53:12694–12712, 1996.

[161] M. Aoki. Rapidly convergent bond order expansion for atomistic simulations. *Phys. Rev. Lett.*, 71:3842–3845, 1993.

[162] M. Aoki and D. G. Pettifor. Angularly-dependent many-atom bond-order potentials within tight binding Hückel theory. *Physics of transition metals*, 1:299–304, 1993.

[163] R. Drautz, D. A. Murdick, D. Nguyen-Manh, X. Zhou, H. N. G. Wadley, and D. G. Pettifor. Analytic bond-order potential for predicting structural trends across the sp-valent elements. *Phys. Rev. B*, 72:144105–1–14, 2005.

[164] P. Kamenski. Orthogonal tight binding model for silicon carbide. Master's thesis, Department of Materials, University of Oxford, 2011.

[165] E. R. Margine, A. N. Kolmogorov, M. Reese, M. Mrovec, C. Elsässer, B. Meyer, R. Drautz, and D. G. Pettifor. Development of orthogonal tight-binding models for Ti-C and Ti-N systems. *Phys. Rev. B*, 84:155120, 2011.

[166] Per-Olov Löwdin. On the non-orthogonality problem connected with the use of atomic wave functions in the theory of molecules and crystals. *J. Chem. Phys.*, 18(3):365–375, 1950.

[167] L. Goodwin, A. J. Skinner, and D. G. Pettifor. Generating transferable tight-binding parameters: Application to silicon. *Europhys. Lett.*, 9:701–706, 1989.

[168] M. Aoki, D. Nguyen-Manh, D. G. Pettifor, and V. Vitek. Atom-based bond-order potentials for modelling mechanical properties of metals. *Prog. Mater. Sci.*, 52:154–195, 2007.

[169] C. H. Xu, C. Z. Wang, C. T. Chan, and K. M. Ho. A transferable tight-binding potential for carbon. *J. Phys.: Condens. Matter*, 4:6047–6054, 1992.

[170] I. Kwon, R. Biswas, C. Z. Wang, K. M. Ho, and C. M. Soukoulis. Transferable tight-binding models for silicon. *Phys. Rev. B*, 49(11):7242—-7250, 1994.

[171] C. Köhler. *Berücksichtigung von Spinpolarisationseffekten in einem dichtefunktionalbasierten Ansatz.* PhD thesis, Department Physik der Fakultät für Naturwissenschaften an der Universität Paderborn, 2003.

[172] M. W. Finnis. Bond-order potentials through the ages. *Prog. Mater. Sci.*, 52:133–153, 2007.

[173] D. G. Pettifor. From exact to approximate theory: the tight binding bond model and many body potentials. *Springer Proc. Phys.*, 48:64–84, 1990.

[174] D. G. Pettifor, M. W. Finnis, D. Nguyen-Manh, D. A. Murdick, X. W. Zhou, and H. N. G. Wadley. Analytic bond-order potentials for multicomponent systems. *Mat. Sci. Eng.*, A365:2–13, 2004.

[175] G. Kresse and J. Hafner. *Ab initio* molecular dynamics for liquid metals. *Phys. Rev. B*, 47:558, 1993.

[176] G. Kresse and J. Furthmüller. Efficient iterative schemes for *ab initio* total-energy calculations using a plane-wave basis set. *Phys. Rev. B*, 54:11169, 1996.

[177] D. M. Ceperley and B. J. Alder. Ground state of the electron gas by a stochastic method. *Phys. Rev. Lett.*, 45(7):566–569, 1980.

[178] J. P. Perdew and A. Zunger. Self-interaction correction to density-functional approximations for many-electron systems. *Phys. Rev. B*, 23:5048, 1981.

[179] P. E. Blöchl. Projector augmented-wave method. *Phys. Rev. B*, 50:17953–17979, 1994.

[180] G. Kresse and D. Joubert. From ultrasoft pseudopotentials to the projector augmented-wave method. *Phys. Rev. B*, 59:1758, 1999.

[181] Hendrik J. Monkhorst and James D. Pack. Special points for brillouin-zone integrations. *Phys. Rev. B*, 13(12):5188–5192, 1976.

[182] James D. Pack and Hendrik J. Monkhorst. "Special points for brillouin-zone integrations"—a reply. *Phys. Rev. B*, 16(4):1748–1749, 1977.

[183] T. Hammerschmidt, B. Seiser, M. E. Ford, D. G. Pettifor, and R. Drautz. BOPfox program for tight-binding and bond-order potential calculations. Unpublished.

[184] P. E. Blöchl, O. Jepsen, and O. K. Andersen. Improved tetrahedron method for brillouin-zone integrations. *Phys. Rev. B*, 49:16223–16233, 1994.

[185] D. Nguyen-Manh, D. G. Pettifor, and V. Vitek. Analytic environment-dependent tight-binding bond integrals: Application to $MoSi_2$. *Phys. Rev. Lett.*, 85:4136–4139, 2000.

[186] Walter A. Harrison. *Elementary Electronic Structure (Revised Edition).* World Scientific Publishing Company, 2004.

[187] T. J. Lenosky, J. D. Kress, I. Kwon, A. F. Voter, B. Edwards, D. F. Richards, S. Yang, and J. B. Adams. Highly optimized tight-binding model of silicon. *Phys. Rev. B*, 55:1528–1544, 1997.

[188] http://www.webelements.com/silicon/physics.html.

[189] H. J. McSkimin and P. Andreatch. Elastic moduli of silicon vs hydrostatic pressure at 25.0 °C and −195.8 °C. *J. Appl. Phys.*, 35(7):2161–2165, 1964.

[190] G. Simmons and H. Wang. *Single Crystal Elastic Constants and Calculated Aggregate Properties: A Handbook.* MIT, Cambridge, MA, 2nd ed edition, 1971.

[191] R J Needs. First-principles calculations of self-interstitial defect structures and diffusion paths in silicon. *J. Phys.: Condens. Matter*, 11(50):10437, 1999.

[192] A. Zoroddu, F. Bernardini, P. Ruggerone, and V. Fiorentini. First-principles prediction of structure, energetics, formation enthalpy, elastic constants, polarization, and piezoelectric constants of AlN, GaN, and InN: Comparison of local and gradient-corrected density-functional theory. *Phys. Rev. B*, 64:045208, 2001.

[193] http://www.zum.de/faecher/materialien/beck/chemkurs/cs11-14.htm.

[194] http://www.colby.edu/chemistry/webmo/n2.html.

[195] K. Huber. *Constants of Polyatomic Molecules.* Van Nostrand Reinhold, 1979.

[196] C. Stampfl and C. G. Van de Walle. Density-functional calculations for III-V nitrides using the local-density approximation and the generalized gradient approximation. *Phys. Rev. B*, 59:5521–5535, 1999.

[197] G. L. Zhao and M. E. Bachlechner. Electronic structure, charge distribution, and charge transfer in α- and β-Si_3N_4 and at the Si(111)/Si_3N_4(001) interface. *Europhys. Lett.*, 37(4):287, 1997.

[198] G. L. Zhao and M. E. Bachlechner. Electronic structure and charge transfer in α- and β-Si_3N_4 and at the Si(111) Si_3N_4(001) interface. *Phys. Rev. B*, 58:1887–1895, 1998.

[199] L. E. Hintzsche, C. M. Fang, T. Watts, M. Marsman, G. Jordan, M. W. P. E. Lamers, A. W. Weeber, and G. Kresse. Density functional theory study of the structural and electronic properties of amorphous silicon nitrides: Si_3N_{4-X}:H. *Phys. Rev. B*, 86:235204, 2012.

[200] J. A. Wendel and W. A. Goddard. The Hessian biased force field for silicon nitride ceramics: Predictions of thermodynamic and mechanical properties for α- and β-Si_3N_4. *J. Chem. Phys.*, 97:5048–5062, 1992.

[201] J. C. Idrobo, H. Iddir, S. Ogut, A. Ziegler, N. D. Browning, and R. O. Ritchie. *Ab initio* structural energetics of β-Si_3N_4 surfaces. *Phys. Rev. B*, 72:241301, 2005.

[202] W.-Y. Ching, Y.-N. Xu, J. D. Gale, and M. Rühle. *Ab initio* total energy calculation of α- and β-silicon nitride and the derivation of effective pair potentials with application to lattice dynamics. *J. Am. Ceram. Soc.*, 81(12):3189–3196, 1998.

[203] Y. M. Li, M. B. Kruger, J. H. Nguyen, W. A. Caldwell, and R. Jeanloz. High pressure x-ray diffraction study of β-Si_3N_4. *Solid State Commun.*, 103(2):107 – 112, 1997.

[204] J. C. Hay, E. Y. Sun, G. M. Pharr, P. F. Becher, and K. B. Alexander. Elastic anisotropy of β-silicon nitride whiskers. *J. Am. Ceram. Soc.*, 81(10):2661–2669, 1998.

[205] M. Aoki and T. Kurokawa. A simple environment-dependent overlap potential and cauchy violation in solid argon. *J. Phys.: Condens. Matter*, 19(23):236228, 2007.

List of Figures

2.1 Calculated Si–N phase diagram at 1 atm from Ref. [35]. (Figure modified from Ref. [38].) 8
2.2 The tetrahedral unit in Si_3N_4 (modified from Ref. [45]). 9
2.3 The idealised Si-N layers in the α and β crystal structures: ...ABAB... for the β structure and ...ABCDABCD... for the α structure [46]. The small and large circles represent silicon and nitrogen atoms respectively. The black circles represent atoms from the A and C layers and the grey circles represent atoms from the B and D layers. 10
2.4 Inert gas pressure (Inertgasdruck) and homologous temperature (T/T_m) effects on the microstructure of deposited films [70]. 16
2.5 Number of N atoms accumulated on the surface at 300 K as a function of the number of incident N^+ ions for ion energies of 50, 100, 150 and 200 eV. [103] 25
2.6 Nitrogen surface concentration measured as a function of N_2^+ dose at several impact energies. [119] 26
2.7 Cumulative number of incident N^+ ions, self-sputtering, deposition and scattering events during bombardment as a function of the number of incident N^+ ions for 100 eV at 300 K. The number of incident N+ ions is equal to the sum of self sputtering, scattering and deposition. [103] 26
2.8 Evolution of the mean cluster size ⟨n⟩ with deposition time t: (A) T_{sub} = 300 K, E_k = 0.1 eV; (B) T_{sub} = 300 K, E_k = 10 eV; (C) T_{sub} = 1000 K, E_k = 0.1 eV [102]. 29
2.9 Effect of the substrate temperature T_{sub} on the mean cluster size ⟨n⟩ with increasing atom coverage Θ (in fractions of one monolayer (ML)): (A) T_{sub} = 300 K, E_k = 0.1 eV; (C) T_{sub} = 1000 K, E_k = 0.1 eV [102]. 30
2.10 Effect of the impact energy on the mean cluster size ⟨n⟩ with increasing atom coverage Θ: (A) T_{sub} = 300 K, E_k = 0.1 eV; (B) T_{sub} = 300 K, E_k = 10 eV [102]. 31
2.11 Simulated atomic structure of the Si films. (a) T = 600 K, (b) T = 800 K, and (c) T = 900 K. (Figure modified from [27].) 33

2.12 Simulated atomic structures of the GaAs films after 10 ns of deposition at different substrate temperatures T and As:Ga flux ratios R. (a) T = 500 K, R = 1.14; (b) T = 800 K, R = 1.19; (c) T = 1100 K, R = 1.67, and (d) T = 1500 K, R = 3.14. [27] 35
2.13 Hopping path contributions $\Phi_{i,2}$ and $R_{ij,4}$ that are taken into account for the evaluation of the analytic BOP. 47
2.14 Screened Coulomb integrals [132] J as a function of interatomic distance R for the elemental silicon-silicon (Si-Si) and nitrogen-nitrogen (N-N) and binary silicon-nitrogen (Si-N) interactions (black: range of function from 0 to 10 Å, grey: range of function from 0 to 30 Å) compared to the unscreened Coulomb interaction. 58

3.1 Two-centre orthogonal TB Si-Si bond integrals obtained from DFT via projection scheme for different structures as a function of interatomic distance R. Equilibrium data are displayed with enlarged symbols. Dashed vertical lines are the first and second nearest neighbour distances in the ground state equilibrium diamond structure, $R_1^\diamond$ and $R_2^\diamond$. 70
3.2 Reduced TB Si-Si parameters calculated from projected bond integrals in Figure 3.1 for different structures as a function of interatomic distance R. Equilibrium data are displayed with enlarged symbols. Dashed vertical lines are the first and second nearest neighbour distances in the ground state equilibrium diamond structure, $R_1^\diamond$ and $R_2^\diamond$. The vertical dotted line marks R_{tail}. 71
3.3 Reduced TB Si-Si parameters from Figure 3.2 including the gradients at the equilibrium first nearest neighbour distance in each structure of silicon. 73
3.4 s and p contributions to the average total density of states of the silicon diamond structure for DFT, projected TB, and reduced TB. For the calculation of the projected TB DOS the same on-site levels were used as for the calculation of the reduced TB DOS. 75
3.5 Two-centre orthogonal TB Si-Si bond integrals from Figure 3.1 including the functions that show how well the bond integrals are approximated by reduced TB. 76
3.6 σ and π bond orders for a first nearest neighbour bond in the silicon (a) graphene, (b) diamond, (c) simple cubic (sc), and (d) face centred cubic (fcc) structures as a function of interatomic distance R. . . . 78
3.7 Total bond order for a first nearest neighbour bond in the silicon (Si) and nitrogen (N) structures in Figures 3.6 and 4.6, respectively, versus $1/z$, where z is the coordination number. 79

3.8 DFT and reduced TB (LCN) binding energy curves for different silicon structures as a function of nearest neighbour interatomic distance R. The number of nearest neighbours is given in parenthesis for each structure. 81

4.1 Two-centre orthogonal TB N-N bond integrals obtained from DFT via projection scheme for different structures as a function of interatomic distance R. Equilibrium data are displayed with enlarged symbols. Dashed vertical lines are, from left to right, the first nearest neighbour distance in the ground state equilibrium dimer, R_1^{dimer}, and the first and second nearest neighbour distances in the equilibrium diamond structure, $R_1^{\diamond}$ and $R_2^{\diamond}$. 93

4.2 Reduced TB N-N parameters calculated from projected bond integrals in Figure 4.1 for different structures as a function of interatomic distance R. Equilibrium data are displayed with enlarged symbols. Dashed vertical lines are, from left to right, the first nearest neighbour distance in the ground state equilibrium dimer, R_1^{dimer}, and the first and second nearest neighbour distances in the equilibrium diamond structure, $R_1^{\diamond}$ and $R_2^{\diamond}$. The vertical dotted line marks R_{tail}. 94

4.3 Reduced TB N-N parameters from Figure 4.2 including the gradients at the equilibrium first nearest neighbour distance in each structure of nitrogen. 95

4.4 s and p contributions to the average total density of states of the nitrogen cubic gauche (cg) structure for DFT, projected TB, and reduced TB. For the calculation of the projected TB DOS the same on-site levels were used as for the calculation of the reduced TB DOS. 97

4.5 Two-centre orthogonal TB N-N bond integrals from Figure 4.1 including the functions that show how well the bond integrals are approximated by reduced TB. 98

4.6 σ and π bond orders for a first nearest neighbour bond in the nitrogen (a) dimer, (b) cubic gauche (cg), (c) diamond, and (d) simple cubic (sc) structures as a function of interatomic distance R. 99

4.7 DFT and reduced TB (LCN) binding energy curves for different nitrogen structures as a function of nearest neighbour interatomic distance R. The number of nearest neighbours is given in parenthesis for each structure. 100

5.1 Two-centre orthogonal TB Si-N bond integrals obtained from DFT via projection scheme for different structures as a function of interatomic distance R. Equilibrium data are displayed with enlarged symbols. Dashed vertical lines are the first and second nearest neighbour distances in the ground state equilibrium β structure, R_1^β and R_2^β. Note that the $ps\sigma$ data is multiplied by -1 to improve the comparability to the $sp\sigma$ data. 107

5.2 Reduced TB Si-N parameters calculated from projected bond integrals in Figure 5.1 for different structures as a function of interatomic distance R. Equilibrium data are displayed with enlarged symbols. Dashed vertical lines are the first and second nearest neighbour distances in the ground state equilibrium β structure, R_1^β and R_2^β. The vertical dotted line marks R_{tail}. 108

5.3 Reduced TB Si-N parameters from Figure 5.2 including the gradients at the equilibrium first nearest neighbour distance in each structure of silicon nitride. 109

5.4 Local s and p contributions of silicon and nitrogen to the average total density of states of the silicon nitride β structure for DFT, projected TB, and reduced TB. For the calculation of the projected TB DOS the same on-site levels were used as for the calculation of the reduced TB DOS. 110

5.5 Two-centre orthogonal TB Si-N bond integrals from Figure 5.1 including the functions that show how well the bond integrals are approximated by reduced TB. 112

5.6 σ and π bond orders for a first nearest neighbour bond in the silicon nitride β structure as a function of interatomic distance R. 113

5.7 DFT, reduced TB LCN, and reduced TB CT heat of formation curves for different silicon nitride structures as a function of nearest neighbour interatomic distance R. The number of nearest neighbours is given in parenthesis for each structure. 114

5.8 Heat of formation for different silicon nitride structures for DFT, reduced TB LCN, and reduced TB CT, versus nitrogen concentration. 120

5.9 Binding energy contributions for different silicon nitride structures for reduced TB CT as a function of interatomic distance R. 122

5.10 Binding energy contributions for different silicon nitride structures for reduced TB LCN as a function of interatomic distance R. 123

6.1 σ and π bond orders for a first nearest neighbour bond of silicon in the (a) graphene, (b) diamond, (c) simple cubic (sc), and (d) face centred cubic (fcc) structures as a function of interatomic distance R of the bond-order potential for silicon. 131

6.2 DFT, reduced TB, and BOP binding energy curves for different silicon structures as a function of interatomic distance R. DFT and reduced TB binding energy curves are taken from Figure 3.8. The number of nearest neighbours in each structure is given in parentheses. 133

List of Tables

3.1 Reduced TB parameters for silicon-silicon (Si-Si), nitrogen-nitrogen (N-N), and silicon-nitrogen (Si-N) interactions. 74
3.2 On-site levels for silicon (Si) and nitrogen (N) (Ref. [186]). 74
3.3 Repulsive parameters for silicon-silicon (Si-Si), nitrogen-nitrogen (N-N), and silicon-nitrogen (Si-N) interactions. 80
3.4 Embedding exponent n_d and shift in the non-magnetic DFT free atom reference energy Δu_{atom} for silicon (Si), and nitrogen (N). 80
3.5 Yukawa parameters for silicon-silicon (Si-Si) and silicon-nitrogen (Si-N) interactions. 81
3.6 Silicon structures used as a binding energy benchmark. Equilibrium binding energies (eV/atom) are given in parentheses (reduced TB, DFT). The structures are ordered with respect to DFT binding energies. 84
3.7 Equilibrium properties of different structures for silicon calculated with reduced TB with p_σ as a function of interatomic distance R as in Figure 3.2, reduced TB with p_σ = const., and DFT. Difference to the diamond equilibrium binding energy (ΔU), equilibrium binding energy (U), equilibrium volume (V), and bulk modulus (B) are obtained from Birch-Murnaghan equation of state fits to binding energies. Units are ΔU and U (eV/atom), V (Å^3), and B (GPa). . 86
3.8 Equilibrium properties of silicon diamond for reduced TB (LCN) and DFT. Equilibrium binding energy (U), equilibrium volume (V), and bulk modulus (B) are obtained from Birch-Murnaghan equation of state fits to binding energies. Units are U (eV/atom), V (Å^3), and B and C (GPa). C^0_{44} is the static C_{44} elastic constant. 88
3.9 Point defect formation energies in silicon diamond (eV). The numbers in parentheses in the top line are the number of atoms per perfect unit cell, whereas the pair of numbers in parentheses in the DFT column from Ref. [191] are LDA and GGA values respectively. 90

4.1 Nitrogen structures used as a binding energy benchmark. Equilibrium binding energies (eV/atom) are given in parentheses (reduced TB, DFT). The structures are ordered with respect to DFT binding energies. 102
4.2 Equilibrium properties of the nitrogen dimer for reduced TB (LCN), DFT, and experiment. Equilibrium binding energy (U), equilibrium nearest neighbour distance (NND), and frequency ν are obtained from Birch-Murnaghan equation of state fits to binding energies. Units are U (eV/atom), NND (Å), ν (cm^{-1}). The pair of numbers in parentheses in the DFT column from Ref. [192] are LDA and GGA values respectively. 103

5.1 Species dependent atomic on-site Coulomb integrals for silicon (Si) and nitrogen (N) from Ref. [171]. 107
5.2 Silicon nitride structures used as a heat of formation benchmark. Equilibrium heat of formation values (eV/atom) are given in parentheses (reduced TB CT, reduced TB LCN, DFT). The structures are ordered with respect to DFT heat of formation values. 117
5.3 Further silicon nitride structures used as a heat of formation benchmark. Equilibrium heat of formation values (eV/atom) are given in parentheses (reduced TB CT, reduced TB LCN, DFT). The structures are ordered with respect to DFT heat of formation values. . . 118
5.4 Lowering of the energy when allowing charge transfer compared to enforcing local charge neutrality ($\Delta(U_{bind} - U_{rep})$) and increase of the energy when refitting the repulsive energy to the binding energy of the ground state β structure (ΔU_{rep}) for different structures of silicon nitride. Units are eV/atom. 121
5.5 Equilibrium properties of the silicon nitride β structure for reduced TB CT and DFT. Equilibrium heat of formation (ΔH), equilibrium volume (V), and bulk modulus (B) are obtained from Birch-Murnaghan equation of state fits to binding energies. Units are ΔH (eV/atom), V (Å^3), B and C (GPa). The FF column displays values of the force field at 0 Kelvin and B is calculated from other elastic constants. 126
5.6 Relaxed point defect formation energies in silicon nitride β (eV) with 112 atoms per perfect unit cell. 127

6.1 Repulsive parameters for silicon-silicon (Si-Si) BOP interactions. . . 132
6.2 Yukawa parameters for silicon-silicon (Si-Si) BOP interactions. . . . 134
6.3 Silicon structures used as a binding energy benchmark. Equilibrium binding energies (eV/atom) are given in parentheses (BOP, DFT). . 136

6.4 Equilibrium properties of silicon diamond for BOP and DFT. Equilibrium binding energy (U), equilibrium volume (V), and bulk modulus (B) are obtained from Birch-Murnaghan equation of state fits to binding energies. Units are U (eV/atom), V (Å^3), and B and C (GPa). C_{44}^0 is the static C_{44} elastic constant. 137
6.5 Point defect formation energies in silicon diamond (eV). The numbers in parentheses in the top line are the number of atoms per perfect unit cell, whereas the pair of numbers in parentheses in the DFT column from Ref. [191] are LDA and GGA values respectively. 140